ABSTRACT

Dennis, Ryan Shaun. Development of a Localized Heat Treatment Tool for Shape Memory Alloy Wires using an Ytterbium Fiber Laser. (Under the direction of Dr. Juei-Feng Tu.)

Creating localized areas of shape memory effect or superelastic effect in a shape memory alloy wire is quite a complicated task. To produce these localized effects in feasible applications it is necessary to precisely control the temperature profile of the treated wire. This is due to a shape memory alloy's notorious sensitivity to composition and heat treatment. In this thesis, a localized heat treatment system based on a one-dimensional heat transfer model coupled with the precise control of a high powered fiber laser has been developed. Also, a variable flow inert gas heat treatment chamber that is specially designed to eliminate the oxide formation in shape memory alloy heat treatments without causing significant forced convection cooling has been developed. Several experiments have been performed in which various heat treatments are prescribed by the model, and then validated by real-time thermocouple temperature measurements. It is demonstrated that localized changes in superelasticity occur, where the treated region takes on shape memory effect properties and even shows signs of precipitate hardening when overaged. More studies are needed to determine specific heat treatment processes that induce desired SMA properties, but this is beyond the scope of this thesis.

DEVELOPMENT OF A LOCALIZED HEAT TREATMENT TOOL FOR SHAPE MEMORY ALLOY WIRES USING AN YTTERBIUM FIBER LASER

by
RYAN SHAUN DENNIS
BSME (Clemson University) 2003

A thesis submitted to the Graduate Faculty of
North Carolina State University
in partial fulfillment of the
requirements for the Degree of
Masters of Science

MECHANICAL ENGINEERING

Raleigh

2005

APPROVED BY:

Dr. Gregory Buckner

Dr. Stefan Seelecke

5-18-2005

Dr. Juei-Feng Tu
(Chair of Advisory Committee)

DEDICATION

I would like to dedicate this work to Allen, Sherry, Jarrod, and the rest of my family and friends that have encouraged me throughout these last six years. Without their support this work would never have been accomplished. I would also like to dedicate this work in memory of my grandmother, Anne J. Dennis, and my grandfather, Max N. Burleson. Thank you for the wonderful memories from childhood, and the life lessons you instilled in me while you blessed us with your presence on this earth. Lastly, this thesis is for a little boy with a set of LEGOS® that never hesitated to disassemble any toy to "investigate" what was going on inside.

"The important thing is not to stop questioning. Curiosity has its own reason for existing."
- Albert Einstein

BIOGRAPHY

Ryan Shaun Dennis was born to W. Allen L. Dennis and Sherry B. Dennis on the night of July 25, 1981. He was born and raised in the same house on Rocky River Rd. in Oakboro, North Carolina until he was eighteen. He attended Oakboro Elementary School for nine years where he went on to graduate from West Stanly High School 10^{th} in his class. Ryan then attended Clemson University, notably one of the finest institutions in the Southeast, studying mechanical engineering as an undergraduate. He graduated Cum Laude in the spring of 2003 from Clemson University with a Bachelors of Science in Mechanical Engineering, and decided to pursue an advanced degree in mechanical engineering back home in his native state of North Carolina. In his first semester of masters studies at North Carolina State University he had the privilege of meeting Dr. Juei F. Tu from which this current research relationship stemmed. Currently, Ryan is finishing up 2 years of masters research under the guidance of Dr. Juei F. Tu, and will soon graduate from North Carolina State University with a Maters of Science in Mechanical Engineering with a concentration in Mechatronics.

ACKNOWLEDGEMENTS

First, I would like to acknowledge Dr. Juei F. Tu, for all of his guidance, and for giving me this incredible opportunity. I would also like to acknowledged Dr. Gregory Buckner and Dr. Stefan Seelecke for their guidance and assistance during my masters research. Lastly, I would like to acknowledge my laboratory peers: Jason Dilwith, Ray Harp, and Alexander Paleocrassas. Thank you for all of your help.

TABLE OF CONTENTS

LIST OF FIGURES

Page

LIST OF TABLES

Page

1 INTRODUCTION

Heat treatments, when controlled properly, can allow an engineer to tailor a material's properties to meet specific demands of an application. A plethora of heat treatments have been developed to change material properties such as: microstructure, grain size, grain boundaries, hardness, internal stress, ductility, toughness, etc. Some of the most common heat treatment processes include: aging, annealing, hardening, tempering, quenching, normalizing, and spheroidizing. Typically, when a heat treatment is performed the process is usually applied to the entire workpiece. But, sometimes it is quite desirable to localize the heat treatment, so as to only change the properties over a small region, such as localized hardening of gear teeth. Localized treatments can provide a great advantage by having varying physical properties on a single workpiece. Developing a localized heat treatment in a material would allow the material to exhibit different properties across the length of the material, which in turn would allow an engineer to tailor a material to meet different demands on the same workpiece. This can be quite advantageous when one workpiece is desired to be subjected to very different loading cases, temperature differences, etc. Certain types of alloys are very sensitive to heat treatment, thus their local properties can be dramatically changed with a simple heat treatment.

A special category of materials, known as Shape Memory Alloys (SMA), which exhibit rather unique properties, have started to gain much attention in the past few decades for their ever-growing uses in many practical engineering applications. A SMA exhibits two important characteristics. First, the Shape Memory Effect (SME) is the ability of the material to "remember" a certain shape and return to that shape upon heating, even after large deformations. Second, the Superelastic Effect (SE) is the ability of the material to be strained up to 10 times the normal amount before plastic deformation occurs. One of the defining properties of a SMA is its transition temperatures, and these temperatures are the key to implementing a SMA material in any system. Due to the sensitivity of SMA to heat treatments, any localized heat treatment would need to have an energy source that could apply precise amounts of energy into a rather small area.

The use of a LASER (Light Amplification by Simulated Emission of Radiation) in engineering applications has proven to be an excellent source of energy input. The

advantages of using a laser are: a narrow beam, very directional, very small spot sizes, very high power density, spectral purity in wavelength, etc. (Hitz *et al.*, 1991) A laser beam can be focused, using optics, to decrease the spot size and increase power density. The applications for the use of a laser seem endless, and include: welding of materials, drilling in materials, heat treating of materials, reading and transmitting data, surgical tools, military targeting applications, commercial bar code scanners, etc. There are many different types of lasers available to perform all these applications. For heat treatments a high power laser is needed to induce the changes in the materials properties, and a particular type of laser, a fiber laser, is becoming a frontrunner in the heat treatment field due to its exceptional beam characteristics. This will play an especially important role in localized heat treatments.

A laser seems to be quite a likely candidate to induce a local heat treatment, due to its ability to provide a large amount of energy to a very small area. This would allow the effected zone to be minimized, thus creating a sharp controlled boundary where different material properties can exist. Being able to apply a localized heat treatment to a shape memory alloy (SMA) would allow a shape memory effect and a superelastic effect to exist on the same workpiece. This could be used to create a SE or SME joint in the material, thus opening up many new doors for engineering development and application.

2 RESEARCH OBJECTIVE

To develop a laser-based technique for localized heat treatment for a SMA wire that will exhibit prescribed properties at different locations.

3 BACKGROUND AND LITERATURE REVIEW

3.1 Shape Memory Alloys (SMA)

Engineers have found some rather ingenious applications for SMA, which really take advantage of the inherent characteristics of the material. They are used as pipe coupling, cell phone antennas, artery stents, and various actuators in electrical appliances. (Otsuka, K. and Kakeshita, T., 2002) Some more sophisticated applications that are still in the research

phases include: adaptive aircraft wings that can change their curvature in mid-flight, cantilever beam actuators that can produce oscillations less than 15 Hertz with small strokes, and nano-muscles, which, when layered, can behave the same way as a human muscle. (Icardi, U., 2001; Ramrkahyani, D.S. *et al.*, 2004; Wang, G. and Shahinpoor, M., 1996)

SMA exhibits two very unique properties, the shape memory effect (SME) and the superelastic effect (SE). The SME is the ability of a material to annihilate a deformation and to recover an 'imprinted' shape. (Hesselbach, 1999) The SME effect occurs within a specific temperature range, and is based on solid-solid phase transition. The other effect is the SE, in which a SMA shows extraordinary elasticity. Just like any other elastic material, a SMA changes shape during a deformation, and returns to the original shape after unloading if there is no plastic deformation. The difference is an SMA will require five to ten times the loading a normal material would to cause a plastic deformation. The restoring force is independent of the strain. These two properties exist in every SMA, and the difference is the transition temperatures at which each property exist. The SME occurs at the lower transformation temperatures and has a martensitic microstructure at this lower temperature; conversely, the SE occurs at the higher transformation temperatures and has an austenitic microstructure at these temperatures.

The transition temperatures define a range of temperatures at which the material under goes a phase transformation from the Martensite phase to the Austenite phase or vice versa. (Hesselbach, 1999) Thus, there is a start and finish temperature for each transformation. The Austenite start and finish temperatures (A_s and A_f), is where the phase is changing from Martensite to Austenite, and the Martensite start and finish temperatures (M_s and M_f), is where the phase is changing from Austenite to Martensite. Figure 1 below shows the different phases and the 4 different transition temperatures described above, but note this an idealized schematic, the phase transformation are not as sharp in actual materials.

The SME occurs when a SMA is below the Austenite start temperature, therefore the SMA has a completely martensitic microstructure, and the material is easily deformable. The material is then heated above the Austenite finish temperature; the material is now in an austenite microstructure and recovers the original shape, which is the shape of the austenite phase, also known as the parent phase. The simple transformation of martensite to austenite allows the SME to be realized. Once the shape is recovered the SMA can be cooled below

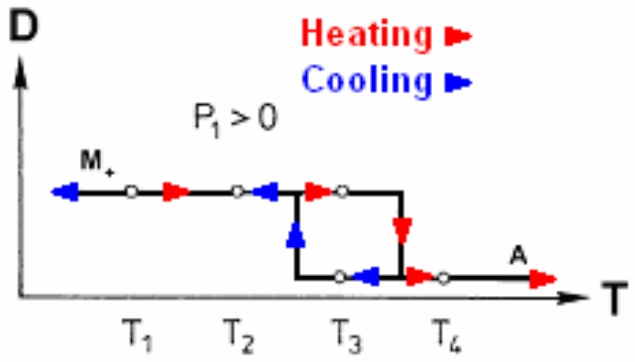

Figure 1. Idealized strain vs. temperature of a typical SMA.

the Martensite finish temperature, and once again be quite ductile. The SE occurs in a similar but opposite manner. It too is a product of the phase transformation, but this time the transformation occurs from austenite to martensite. An unstrained superelastic wire will have a completely austenitic microstructure, but once strain is applied areas of the austenite will transform to a strain induced martensite phase to accommodate the strain in the material, thus the SE is realized. Once the strain is released, the martensite transforms back to austenite and the wire will return to its normal shape. In both the SME and SE, there is a threshold of deformation to which the material will not recover. Finding ways to manipulate the transformation temperatures at which these properties occur can be quite desirable in many engineering applications.

The transformation temperatures of the wire, and furthermore the actual presence of a SME or SE is dependent on certain characteristics of the wire such as: the manufacturing methods, environmental conditions during formation, the plastic working conditions, the shape memory heat treatment, and the balance of Ti-Ni content. Factors such as manufacturing methods, plastic working conditions, and environmental conditions during formation do not concern this research, especially since the wires that will be experimented upon will be purchased with these characteristics already established. Also, knowing the Ti-Ni content is important, but once the wire is formed there is no practical method for removing either element from the alloy. Therefore, the focus of this research is to use the heat treatment to manipulate the transition temperatures. Understanding how these properties can be manipulated to change the transition temperatures is a key step in being able to use a

heat treatment to achieve the desired properties. Also, more in-depth information on SMA can be found in Appendix 11.1.

3.2 Manipulation of SMA Properties

While the transition temperature of an SMA has shown to be influenced by a complex fashion of the manufacturing methods, environmental conditions during formation, the plastic working conditions, and the shape memory heat treatment, the most important factor is the Ti-Ni ratio. (Kaieda, 2003)

In a pure Ti-Ni material, a small change of 0.1% in the proportion of Ni can cause a 10K change in the transformation temperature. For Nitinol, a very commonly used SMA, the compositions can vary from 50:50 Ni:Ti to 51.2:48.8. (Hodgson, 2002) The transformation temperatures for each composition are 100^{o}C to -20^{o}C, respectively. This is a 120 degree difference over a 1.2% composition change. In commercial steel a slight segregation will not produce any noticeable effects in the material's behavior, but in a SMA homogeneity is extremely important due to the drastic impact that the composition makes on its inherent properties. (Kaieda, 2003) Austenite and martensite transformation temperatures fall rapidly with increase in Ni content, and they actually go so low that it can be difficult to measure, i.e. -60^{o}C for 50.5% Ni, see Figure 2.

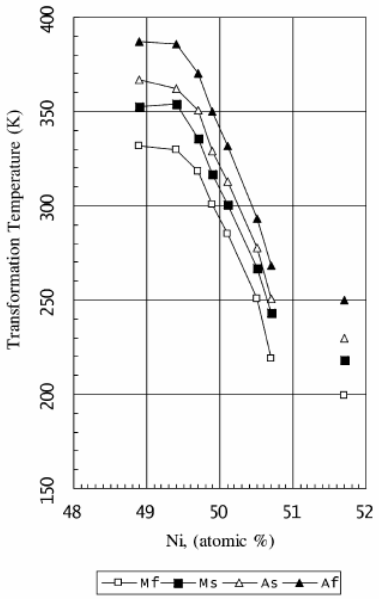

Figure 2. Change in transformation temperature of Ti-Ni wire solution-treated. (Kaieda, 2003)

Another way to change the Ti-Ni balance in a wire is to add some sort of alloying element. Most alloying elements are typically used to either gain some other beneficial property from the SMA, or to impact the SME and SE effects directly. Jiangnan experimented with adding Tantalum (Ta), and found that the material had elevated phase transformation temperatures; it was less sensitive to Ni content, increased X-ray visibility, and excellent shape memory properties. (Jiangnan *et al.*, 2003) Aluminum is another alloying element, and it is used to increase the recovery of the shape memory effect. This is accomplished due to the increased hardening effects, and the slowing of nucleation and growth rates for precipitates that Al causes when added to a SMA. (Hsieh and Wu, 1997) Hsieh and Wu also discover that adding in Zirconium (Zr) will raise the martensite start temperature (M_s) significantly. For one particular alloy that was studied the increase in M_s was 900%. Also, adding Zr increases the hardness of the material after annealing. Lastly, adding Copper (Cu) to SMA will make a marked increase in the damping capacity of the material at room temperature. This stems largely from the increase in internal fiction that is caused by adding the Cu. (Yoshida *et a.*., 2004) The alloys used in this research are simply composed of binary Ti-Ni alloys though. This will reduce the complexity involved in the interaction of an alloying element in the heat treatments, thus targeting in solely on the changes due to the binary interactions.

The focus of this research is going to be geared towards the use of heat treatments to change the properties of the SMA. Specific heat treatments will be discussed in detail in the Section 3.3, but as for now it is necessary to understand what exactly the heat treatments can do to the properties of the SMA and how that will affect the SMA's characteristics. There are a multitude of heat treatments, but the goal of many heat treatments, especially those used to treat SMA, is to change the amount of precipitates or the grain size in the alloy itself. The affects of changing both of these properties in an SMA alloy are discussed in detail below.

The binary alloy Ti-Ni can have any amount of Ni and balance Ti, but as previously mentioned the best SMA are derived from those alloys that are close to equiatomic. A typical binary Ti-Ni SMA with an atomic balance around 50-50 will have a structure similar to that of CsCl. This applies to both the austenite and martensite phases. The microstructure for the CsCl alloy is shown below in Figure 3.

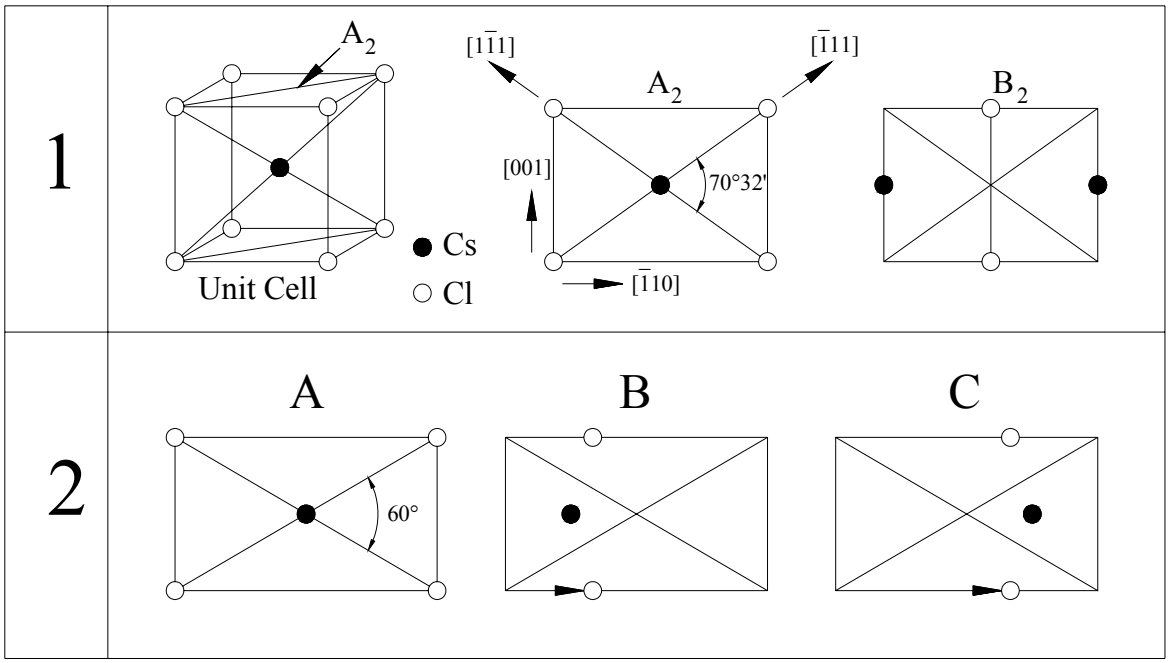

Figure 3. CsCl microstructure. (1) The alternating stacking planes for the austenite phase. (2) The stacking planes for the martensite plane, where the arrow represent the shift vector with respect to A. (Funakubo ed., 1987)

Certain heat treatments can actually cause some of the Ti or Ni to pull out of the equilibrium matrix and bond with more of the other binary element. In Ni rich SMA, the Ti would bond with the excess Ni and make nickel rich precipitates, and vice versa in Ti rich alloys. Note that no precipitates are formed with alloys of Ni composition between 50 and 50.5 percent; the diffusion will not take place due to the lack of excess Ni. One tool that may aid in understanding how to manipulate SMA is the phase diagram for Ti-Ni. The phase diagram, shown in Figure 4, is much like a typical binary phase diagram, and can be useful in understanding how the precipitates are formed in an SMA. Also, see Appendix 11.2 for a larger version of this figure.

The amount of precipitates in the material is very important, since these precipitates ultimately change the transition temperatures of the alloy. Therefore, having a sufficient understanding of the different precipitates that are created during a particular heat treatment is necessary. In Ti-52Ni, isothermal aging is carried out, and the results are displayed in a TTT diagram as shown in Figure 5.

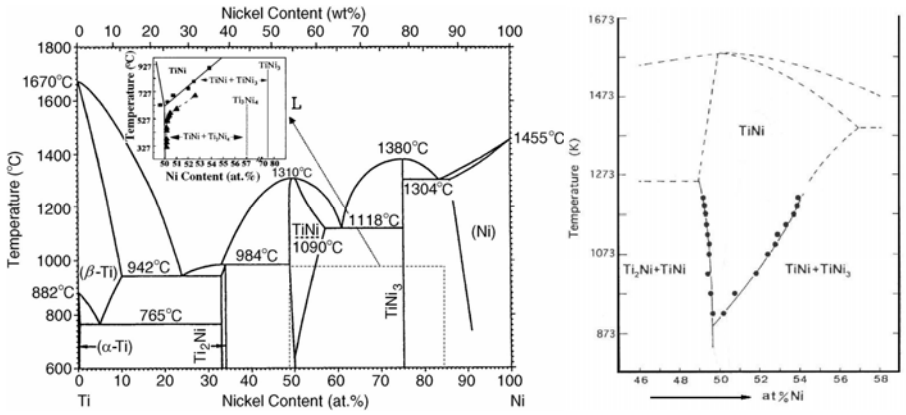

Figure 4. Ti-Ni phase diagrams. (T.B. Massalski, T.B., *et al*., 1990; Otsuka and Wayman, 1998)

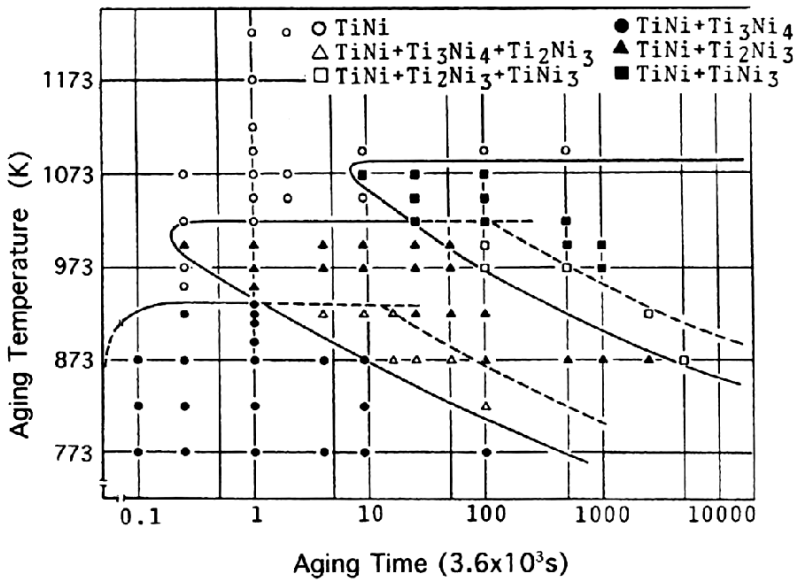

Figure 5. Time Temperature Transformation (TTT) diagram for isothermally aged Ti-52Ni. (Nishida et al., 1986)

It is easy to see from Figure 5 that the precipitation sequence is divided into three aging temperature regimes. They are as follows:

$$TiNi \rightarrow TiNi + Ti_{11}Ni_{14} \rightarrow TiNi + Ti_2Ni_3 \rightarrow TiNi + TiNi_3 \qquad T_a \leq 680^oC \pm 10\,^oC$$

$$TiNi \rightarrow TiNi + Ti_2Ni_3 \rightarrow TiNi + TiNi_3 \qquad 680^oC \pm 10\,^oC \leq T_a \leq 750^oC \pm 10\,^oC$$

$$TiNi \rightarrow TiNi + TiNi_3 \qquad 750^oCK \pm 10\,^oC \leq T_a$$

Note that T_a represents the aging temperature. The solidus line for the Ti-Ni phase in the Ti-52Ni alloy lies between 800°C and 825°C±10 °C. This is reported by Nishida after specimens were aged for 100 hours at 800°C and 825°C and no aging products were seen. Also, this was indicated by the absence of a secondary phase in specimens aged at 825 °C for 500 hours or more. When the precipitates form, two fundamental changes happen in the crystallographic matrix. First the balance of Ti and Ni is changed. For example, in a Ni-rich Ti-Ni alloy if a precipitate is formed then the Ni concentration in the equiatomic matrix will be reduced. This will change the transition temperatures as previously described in other sections.

The second change is coherency stress fields are produced. This can be visualized in the schematic Figure 6. (Khalil-Allafi *et al*., 2002) These stresses can affect the alloy by changing the transition temperatures, inhibiting grain growth along grain boundaries, affecting the way in which the martensitic transformation takes place, supporting the formation of an R-phase, etc. How much of an effect the precipitate has depends on the composition of the alloy, the type of the precipitate, the thermo-mechanical treatment to produce the precipitate, as well as where the precipitate nucleates in the crystal structure.

Another important factor in determining the transformation temperatures of a SMA is the grain size. During a laser heat treatment, the grain size of the material can be altered to effectively change the forward and reverse transformation temperatures. A relationship between the elastic energy of the material and grain size can obtained, and a thermodynamic analysis shows that the elastic energy will decrease with increase in grain size. (Gil and Planell, 2000) This is due to the fact that as the grain size increases the martensitic plates

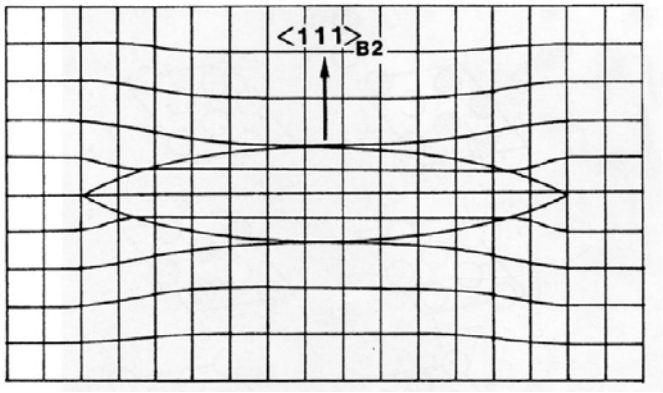

Figure 6. Lattice distortion due to stress field produced by precipitate in parent phase of Ti-Ni alloy. (Otsuka and Wayman, 1998)

grow larger between the grain boundaries, thus producing an increase in local elastic energy. This then facilitates the nucleation of new plates. Also, small crystals possess larger internal stresses due to anisotropy, which is produced by the different orientations of the grains, and that in turn aids the martensitic transformation. Therefore when grain size is small M_s is higher, conversely the M_s is lower when the grain size is large, and this is shown in Figure 7. (Gil and Planell, 2000) Similarly the frictional energy decreases with grain size, where the frictional energy is calculated as the area within the hysteresis loop (normalized entropy versus temperature). This is due to the appearance of bigger plates that decrease the grain boundaries, thus decreasing frictional energy. Figure 7, below, shows the trend of the change in M_s and A_s as grain size is increased. Figure 7 shows how both temperatures linearly decrease with grain growth. Showing how the grain boundaries favor the martensitic transformation, but they also obstruct the reverse transformation. The influence of the grain boundaries does not concern the nucleation of the first martensite plates; rather it takes place in the propagation in the polycrystals, when the plates interact with the grain boundaries. Similarly the A_s is larger with a small grain and vice versa. This is due to the fact that the martensite plates decompose in the same manner in which they nucleate, where it takes a great deal of energy to separate the plates from the grain boundaries. (Gil and Planell, 2000)

3.3 Heat Treatment

Heat treatments, when controlled properly, can allow an engineer to tailor a material's properties to meet specific demands of an application. A plethora of heat treatments have been developed to change material properties such as: microstructure, grain size, grain

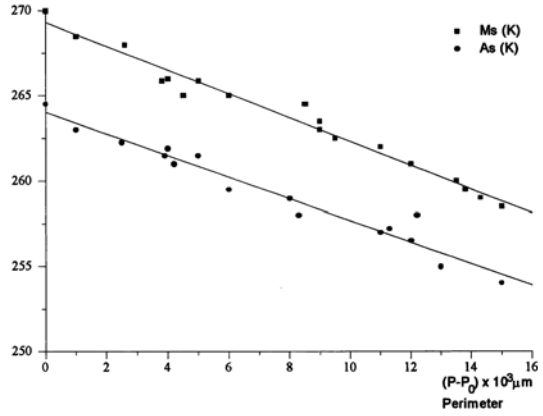

Figure 7. M_s and A_s versus grain size. (Gil and Planell, 2000)

boundaries, hardness, internal stress, ductility, toughness, etc. Some of the most common heat treatment processes include: aging, annealing, hardening, tempering, quenching, normalizing, and spheroidizing. Heat treatments are usually performed on the whole workpiece, and these processes are usually carried out in one of the following manners: continuous heat treatment, batch process, or fluidized beds. A type of heat treatment that is important to this research and deserves some review is annealing. This heat treatment is going to be used to change the grain size and the precipitates.

Annealing is carried out in three distinct stages: (1) heating to the desired temperature, (2) holding or "soaking" at that temperature, and (3) cooling, usually to room temperature. (Callister, 1997) Time is a very important parameter in each step and will ultimately dictate the effects of the treatment process. Annealing can be used to increase softness, ductility, toughness, relieve stresses, and produce a desired microstructure. Changing the annealing temperature of the SMA is a useful way to adjust transition temperatures. For an equiatomic wire (50/50 Ni:Ti) when the annealing temperature is higher the transition temperatures will be higher. (Hodgson, 2000) For a nickel rich wire (i.e. 51/49 Ni:Ti), when the annealing temperature is higher the transition temperatures will be lower, and this is due to the slightly higher Nickel content.

Ti-rich films show transformation temperatures higher than room temperature, thus allowing the development of SMA actuators at ambient temperature. (Surbled *et al.*, 2001) Upon proper annealing Ti-rich and Ni-rich films showed respectively Ti_2Ni and Ti_3Ni_4 precipitates, with different effects on the SME. The difference between Ni-rich and Ti-rich

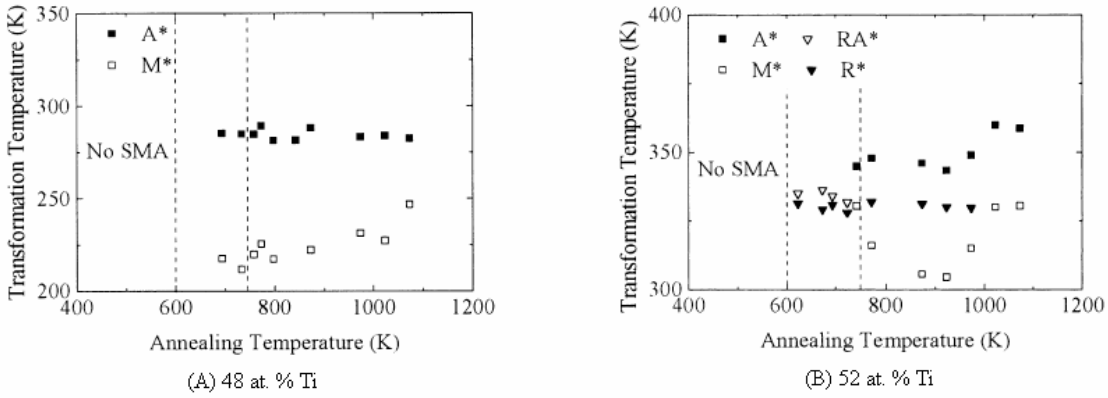

Figure 8. Ni-rich (A) versus Ti-rich (B) changes in transformation temperature due to annealing temperatures. (Surbled *et al.*, 2001)

films response to annealing temperature can be seen in Figure 8. Figure 8 shows the dependence of Ti-rich films on annealing temperatures, and how it doesn't affect the Ni-rich films much at all. The figure also shows that in Ti-rich films there are no SMA effects when annealed below 600K because it is amorphous. When annealed between 600K and 740K the film has a mirror finish and extremely ductile, and here the film has Ti-rich plate precipitates between equiatomic nanocrystals. When annealed above 740K and below 1000K a R-phase is realized, Ti_2Ni begins to precipitate, and an evolution of precipitate distribution due to non-equilibrium precipitates and the growth of precipitates is observed. These three distinct stages are realized by exotherms corresponding to formation of different precipitates. Also the transformation temperature hysteresis decreases with decreasing annealing temperatures. Ti-rich Ti-Ni films annealed at lower temperatures showed transformation temperature hysteresis as low as 3K, and this is promising of a faster actuating SMA in the future.

Aging, as it is commonly called, is really an annealing heat treatment in which the supersaturated solid solution of a binary alloy is heated to some intermediate temperature in the α+β two-phase region. (Callister, 1997) Aging is sometimes also referred to as precipitation heat treatment. Here diffusion rates increase to the point that β phase precipitates and form finely dispersed particles. The time it takes to form the desired amount of precipitate is called the aging time, and this can be from a few minutes to a few hundred hours. After this time the heating is removed and the workpiece is allowed to air cool naturally. Figure 9 shows the heat treatment as shown on a phase diagram (a) and on a TT diagram (b).

Aging in SMA is used to change the transition temperatures by creating precipitates that decrease the Ti-Ni ratio, thus changing the transition temperatures, but the precipitates should not interfere with the SME or SE. Therefore, Ti-Ni can be heat treated for aging, thus precipitating Ti_3Ni_4, to raise the M_s, etc., temperatures for further study of the effects of increased Ni content. (Kaieda, 2003) The precipitation of Ti_3Ni_4, lowers the Ni content in the matrix, which promotes the rise in transformation temperatures. When the transformation temperatures of the aged material are explored, it is seen that the transformation temperatures continue to decline until 51.4% Ni content, it bottoms out and begins to rise again at 51.7% Ni content, and this is seen in Figure 10 below. Also, an R-phase transformation was evident when the ratio was 49.7% or greater, but when the Ni content decreases, the Ms, etc.,

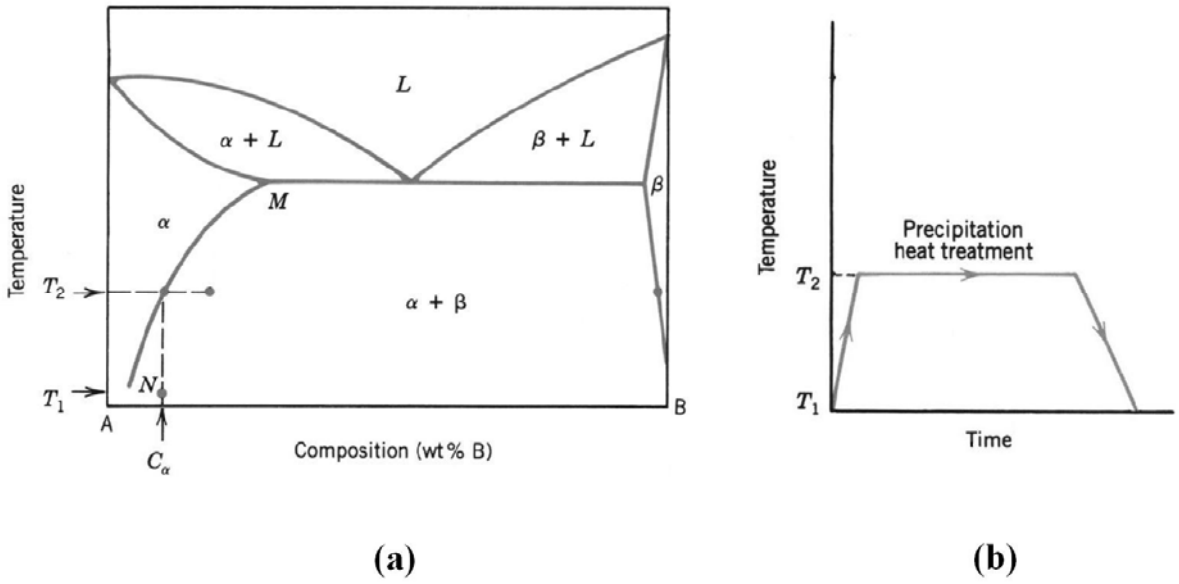

Figure 9. Precipitation heat treatment phase diagram and the corresponding TT diagram. (Callister, 1997)

temperatures increase, and a direct martensite to austenite phase transformation occurs, and this is also shown in Figure 10 below. Using the alloy $Ni_{46}Ti_{44}Ta_{10}$, Jiangnan attempted to experiment with a range of aging temperatures, 573K to 823K, and a range of aging times to determine the effect on the transition temperatures and the SME and SE.

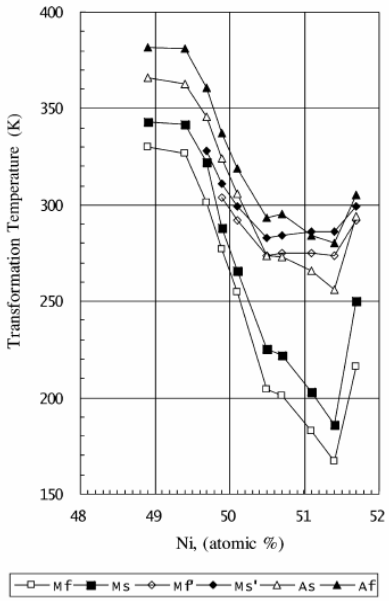

Figure 10. Transformation temperature of Ti-Ni wire heat treated for aging. (Kaieda, 2003)

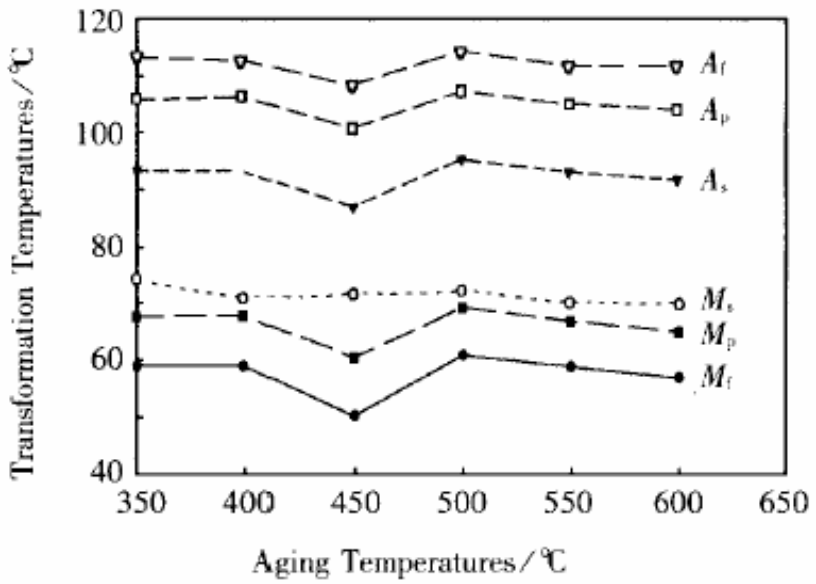

Figure 11. Variation of transformation temperature with aging temperature. (Jiangnan *et al.*, 2003)

NiTiTa is used because the transition temperatures are less sensitive to the Ni content, and this is believed to be due to a Ta rich phase and a $NiTa_2$ compound. (Jiangnan *et al.*, 2003) Also, from an applications point of view, the ease of control over transition temperatures and the excellent SME is essential.

Figure 11 clearly shows the change of M_f, A_s, and A_f temperatures can be classified into three stages. As the aging temperatures increase from 623K to 723K the transformation temperatures fall, from 723K to 773K they rise, and above 773K they slightly fall. In the first stage the nucleation and growth rate of the precipitate is relatively slow, and the Ni/Ti ratio will increase, thus the transformation temperatures decrease. But at 723K, the dispersed Ta phase comes out of the Ti-Ni matrix, and more $NiTa_2$ compound is formed. This causes the Ni/Ti ratio to increase, thus stage two occurs and the transformation temperatures increase. Finally above 773K, stage three a balance of precipitate and second phase is reached, and increasing the aging temperature affects the transition temperatures only slightly. Jiangnan found that the best SME occurred during the first 30 minutes at the lower aging temperatures, but as the duration increased the recovery rate decreased as well. Upon aging in the temperature range of 773K to 823K, the best SME occurred in the early stage of the aging, usually less than 10 minutes. The most practical level of SME was obtained when the samples were aged at a temperature range from 673K to 773K. Interestingly, the best SME

always occurred at an aging condition that corresponded to the maximum hardness value, and this is due to the increased difficulty of the dislocation propagation.

It is quite easy to see that annealing and aging are very similar. Typically the distinction is in the time over which the material is soaked at a certain temperature to create these effects. Normal aging implies a longer soak time on the order of minutes, hours, or even days, whereas annealing usually implies soak times of seconds or minutes. But, there is a way to reverse the growing of precipitates and essentially change the transition temperatures by simply eliminating the precipitates. This would grow larger Ti-Ni grains by dissolving the precipitates back into the matrix. This is a process called a solution heat treatment.

In a solution heat treatment all of the solute atoms are dissolved to form a single-phase solid solution. (Callister, 1997) This is accomplished by heating the alloy composed of $\alpha + \beta$ to an α phase field and soaking at this temperature until all of the β phase has dissolved into the α phase, and then the alloy typically water quenched, as to prevent any reformation of the β phase. The equiatomic phase of Ti-Ni is represented by the α phase and the precipitates are represented by the β phase in a SMA. Therefore a nonequilibrium supersaturated solid α phase now exist with little or no β phase present. Figure 12 shows the heat treatment as shown on a phase diagram (a) and on a TT diagram (b). Typically diffusion rates at lower temperatures is extremely slow, therefore this phase should be retained for relatively long periods of time. But if the material is operating over range of higher temperatures, thermal cycling issues can occur. The SMA would need to be thermally cycled, which would decrease performance of the SMA due to the diffusion of β that will occur. Usually after a certain number of thermal cycles the SMA will reach a point where the diminishing effects of diffusion are no longer noticeable.

It is easy to see how aging/annealing and solution heat treating are essentially complementary opposites. In the fact that the former attempts to produce precipitates by a lower temperature heat treatment that is soaked and then slowly cooled, and the latter is heated higher to produce a singular phase solution and then cooled as quick as possible to prevent the precipitates from forming. These treatments each affect transition temperatures, but how they raise or lower the temperatures depends mainly on the alloy's composition, previous thermo-mechanical treatments, the duration of soaking at an elevated temperature,

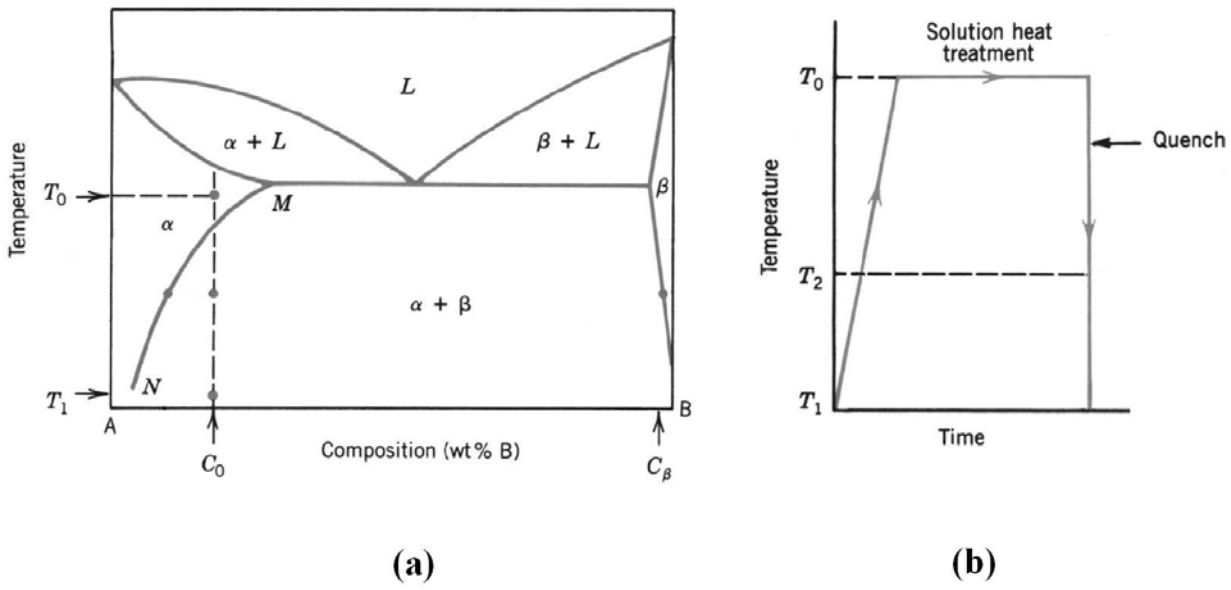

Figure 12. Solution heat treatment phase diagram with corresponding TT diagram. (Callister, 1997)

and the rate of cooling. Now that these treatments have been established it is the concern of this research to apply them locally. All of the treatments that have been mention are quite well established and documented, but effectively applying them locally to SMA is the real challenge.

3.4 Localized Heat Treatment

Localized heat treatments are used to change the material's properties only over a small region, such as localized hardening of gear teeth, stress relief and repair of welded joints, annealing of work hardened flexible joints, etc. Developing a localized heat treatment in a material would allow the material to exhibit different properties across the length of the material, which in turn would allow an engineer to tailor a material to meet different demands on the same workpiece. Induction coils are one of the primary means of conducting localized heat treatments, and lasers are becoming ever more popular for conducting localized heat treatments for fine wires, narrow tubes, thin plates, and micro-devices.

Some localized annealing techniques have already been tested on SMAs where it is impossible to furnace anneal the material. In one example, $Ni_{52}Ti_{48}$ is deposited by DC magnetron sputtering onto a Si(100) wafer. The normal temperature used to anneal the SMA to give it a shape memory is around 450^{o}C, because at this temperature recrystallization

occurs. With the SMA sputtered on the wafer, this temperature would destroy the wafer if placed in a furnace, therefore a laser can be used to locally anneal the metal, thus inducing a shape memory. In a furnace, changing the temperature and annealing time will change the transition temperature of the SMA. The equivalents in laser annealing is changing the laser fluence (mJ/cm^2), which is like changing the annealing temperature, and changing the laser pulses, which is like changing the annealing time. (Xie *et al.*, 2003) Xie experimented with a method of laser annealing. The method employed is to test a range of laser fluence from $582.0mJ/cm^2$ to $189.0mJ/cm^2$, and vary the laser pulses, which are 23ns in duration, from 1 to 40. The best sample was obtained using 10 pulses at $252.0mJ/cm^2$ and cooled at 10^oC/min. After annealing, the sample was shown to be amorphous and has a crystalline structure. Therefore, it is possible for the sample to have phase transformation temperatures. But after Differential Scanning Calorimeter (DSC), shown in Figure 13, there is no peak in the cooling process; this would indicate the transformation back from austenite to martensite. Since there is no peak, this indicates that the material must have a reverse transformation temperature lower than -43^oC, which is the lowest temperature tested by the DCS, therefore the SMA is exhibiting the superelastic effect. Xie, conclude by stating that in published work the martensite starting temperature is around -56^oC when annealed at 693^oC. (Surbled *et al.*, 2001) Also, that for the sample tested the austenite starting temperature is around 0^oC and the martensite starting temperature is probably around -50^oC, but they are limited by testing equipment to determine this. Furthermore, it is possible to laser anneal a thin film to induce recrystallization while keeping the material amorphous, thus producing a shape memory, although exhibited as superelasticity at room temperature. (Xie et al., 2003)

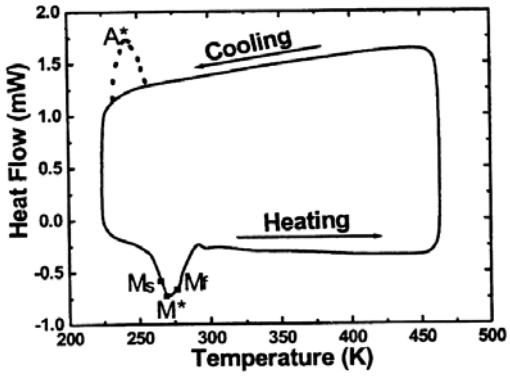

Figure 13. DCS measurements of $Ni_{52}Ti_{48}$ thin films. (Xie *et al.*, 2003)

Another localized annealing technique has been performed, where the heat source for the annealing is a 2W diode laser. The key idea in laser annealing is to select and anneal the place where a SME or SE is desired. (Hafez *et al.*, 2000) This method can be applied to a SMA film, cold rolled sheets, cold drawn wires, or other materials which have been work hardened. The annealing process then reduces the amount of internal stress. The objective here is to create a clamping joint in a microgripper that has been cut out of a non-annealed, work-hardened SMA thin sheet. The microgripper is shown in Figure 14. The annealed area is the shaded area in Figure 14, and will activate the first time by closing the jaw shut upon heating above the transformation temperatures, and then a mechanical force will be required to deform it back to its open position. On subsequent heating the jaw will close, and upon cooling the bias spring will reopen the jaw. During the annealing process the heating time is of one second maximum, the laser power is approximately 1.5W, and the monitored temperature on the actuating part was about 823K whereas the bias spring only heated up to about 373K. The change in the stress-strain behavior of a cold rolled sheet before and after annealing is shown in Figure 15.

The main advantages of the local laser annealing are the freedom to choose the parts to be annealed (i.e. with a spatial resolution of less than 100μm), no particular design restrictions, contactless technology (i.e. no delicate handling problems) and suitability for MEMS technology and MEMS fabrication environment (e.g. clean room, vacuum chamber, etc.). Overall local laser annealing can introduce different mechanical properties in the same part combining active and passive regions with a flexible, contactless, and cheap technology. (Bellouard *et al*., 1999) Therefore, a deeper understanding of lasers must be gained to

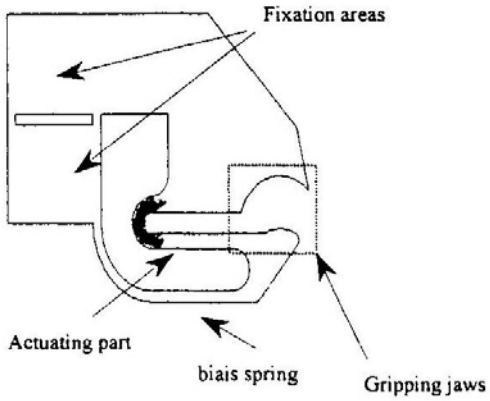

Figure 14. SMA microgripper to be locally annealed with a diode laser. (Bellouard *et al.*, 1999)

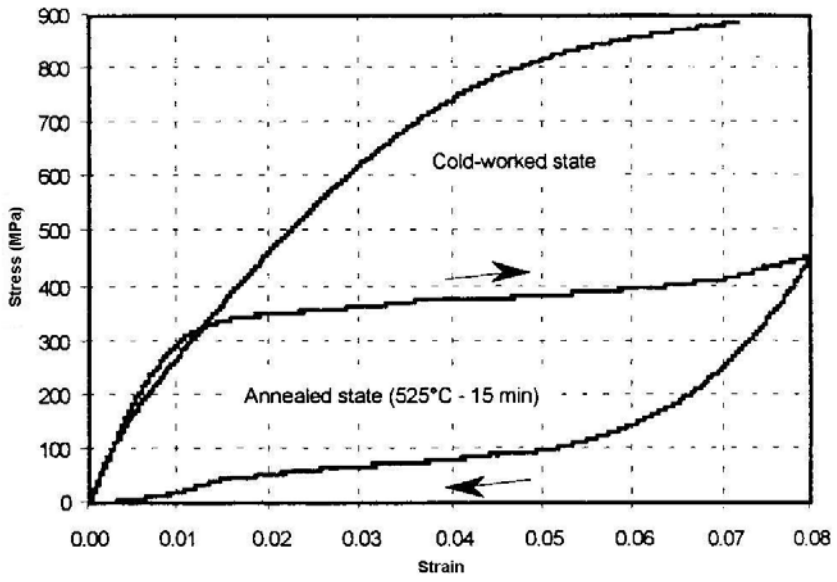

Figure 15. Stress-strain behavior of a cold rolled sheet before and after annealing. (Hafez *et al.*, 2000)

understand how they can be effectively used in SMA heat treatments. More background on the heat treatments mentioned in this section can be found in Appendix 11.3.

3.5 Fiber Lasers

The use of a laser in engineering applications has proven to be an excellent source of energy input. The advantages of using a laser are: a narrow beam, very directional, very small spot sizes, very high power density, spectral purity in wavelength, etc. (Hitz et al., 1991) A laser operates by collecting millions of photons from a lasing medium that is pumped with energy and output directionally. The beam can be further focused, using optics, to decrease the spot size and increase power density. The applications for the use of a laser seem endless, and include: welding of materials, drilling in materials, heat treating of materials, reading and transmitting data, surgical tools, military targeting applications, commercial bar code scanners, etc. Lasers are available in a multitude of power levels as well as lasing mediums. Appendix 11.4 has more information about the properties inherent with lasers. One particular type of laser that interests this research is an Ytterbium solid-state fiber laser. The desirable properties that this type of laser possesses and its application in laser heat treatments will be discussed further in the proceeding sections.

The modern high-power fiber laser is pumped by high-power multimode diodes via a cladding surrounding a single-mode core. The concept allowed the efficient conversion of multimode output radiation from a solid state pump laser, or a broad-stripe semiconductor laser diode into single-model emission of fiber lasers. In simple double-clad fiber architecture, an axial single-mode glass core is doped with the desired laser ion, such as Ytterbium, which is used in the laser utilized for this research. (Gapontsev and Krupke, 2002) There are three essential advantages of using a fiber laser versus using other conventional lasers, and these consist of the very high optical damage threshold of quartz fibers, higher output power density, and the way in which heat is dissipated. (Gapontsev and Samartsev, 1991) The first advantage is associated with the very high optical damage threshold of quartz fibers. The optical damage threshold to the fiber is at fluences on two orders of magnitude higher than that of competing lasers, and it achieves enormous values mounting to 5 to 10 MW/cm^2. The second advantage of fiber lasers is connected with being able to use highly opened cavities even for continuous watt operation due to a very high single-pass gain. As a result the intensity at the workpiece can be 4 to 8 MW/cm^2, and this is 20 to 50 times higher that in other lasers. The third advantage of fiber laser is the ability to sink heat in the active media at excitation. This allows for units up to 2 kilowatts of continuous power to simply be air cooled. Most other kilowatt lasers must be water cooled and have water chillers which takes up more space, adds operating cost, and requires more equipment. Some the other advantages of fiber lasers are particular to the manufacturer of the laser used in this particular research, IPG Photonics. First, the diodes used to pump the laser have a pump to laser conversion of 70%, a life of 100,000 plus hours, and wall plug efficiencies in excess of 27%. (Shiner, 2004) In other conventional lasers the wall plug efficiencies barely eclipses 10%, and the life of the diodes is only 10,000 hours at best. (Gapontsev and Krupke, 2002) One of the more important characteristics of a fiber laser is the extremely high beam quality. The beam is a single mode beam with a Gaussian profile, and has a M^2 value of 1.1, whereas other lasers have much higher M^2 values especially in the kilowatt range. (Shiner, 2004) Figure 16 shows the comparison of the fiber laser to other lasers. The beam profile can also be seen in the Figure 17, where the beam is shown to have a single mode and a Gaussian profile.

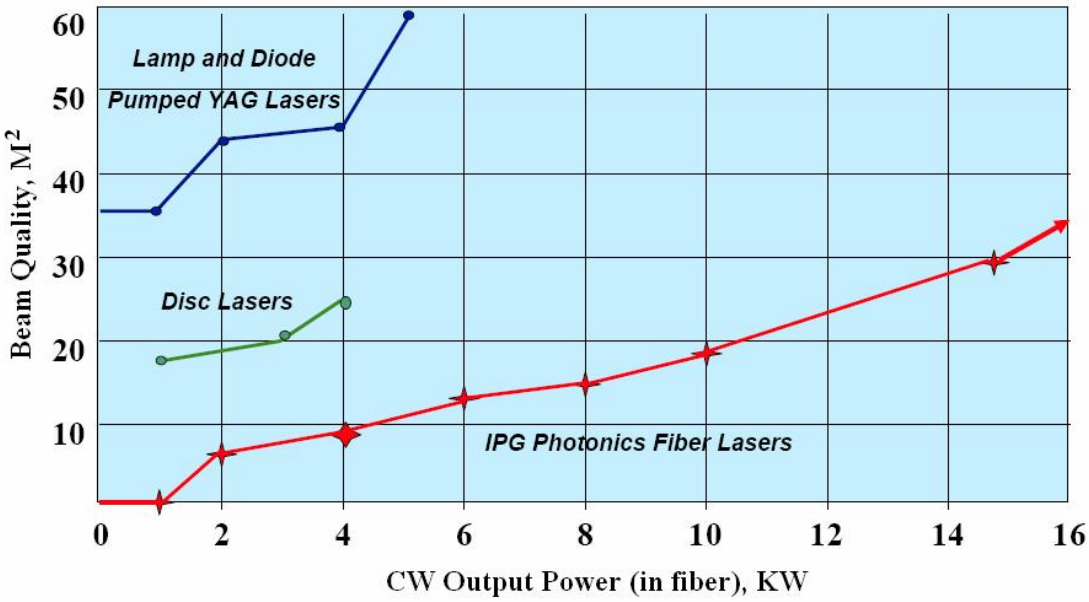

Figure 16. M^2 value of common industrial lasers (Shiner, 2005)

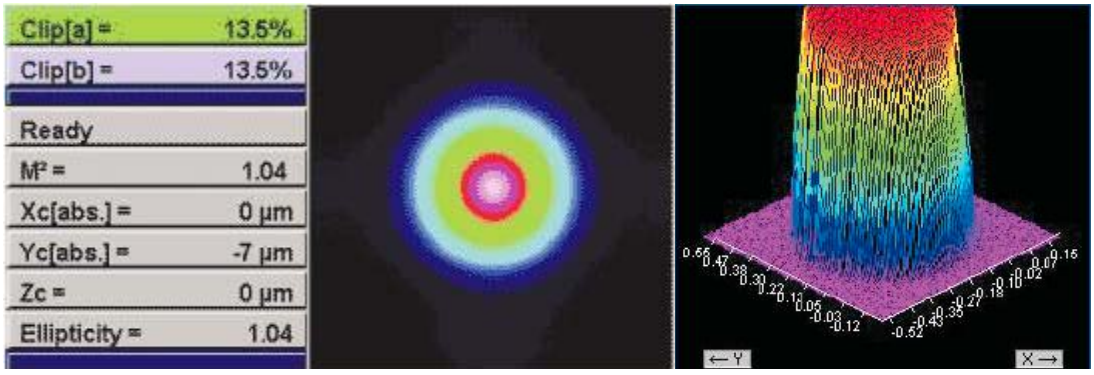

Figure 17. 300W single mode beam profile of fiber laser. (Shiner, 2004)

All of the characteristics discussed above are the attractive qualities of fiber lasers that make them desirable for almost any application, but there are certain qualities that the fiber laser possesses that are crucial to localized heat treatments in shape memory alloys.

As discussed in Section 3.3, laser heat treatments of SMA are becoming increasing popular due to the lasers ability to localize the effects of the heat treatments. Much of the laser heat treatments that have been performed on SMA apply to very small devices, and the lasers used in the heat treatments are only on the order of a few watts. But to heat treat larger workpieces and to achieve faster heating rates a more powerful laser must be used. As discussed above, due to the high damage threshold of the quart fibers and the efficiency of the laser diodes in the fiber laser, the large amount of power needed to produce the heating

rates in SMA workpieces can be generated in an economical package. One of the most crucial elements in localized laser heat treating is the beam profile. Since the heat treatments are desired to be small and localized, a multimode beam will produce uneven heating in the treated region and cause a larger heat affected zone in the workpiece. Since the fiber laser has an exceptional beam profile and quality, the energy can be applied very precisely, in a small region, with even energy distribution in the treated region, and with less affected area around the treated region. These aspects are very important in localized heat treatments of SMA, and make a fiber laser the best choice for this type of research.

4 HYPOTHESIS

A laser treatment model can be developed to precisely control a heat source, provided by a fiber laser, from which localized heat treatments can be created in a SMA wire to change the transition temperature at those localized spots. Thus a continuous wire can exhibit regions of no SMA effects, shape memory effects, and/or superelastic effects, all at the same temperature, strain, and stress conditions.

5 RESEARCH PROBLEMS

There are several significant problems present in this research. Currently there is not a model that will predict the effects of a heat treatment in the SMA wire. There should be a simple heat transfer model that can be derived so that given an energy input profile a continuous solution for the temperature distribution in the wire could be generated. The energy input by the laser needs to be carefully controlled. The properties of an SMA wire are very sensitive to heat treatments. Pulsing the laser beam is a likely method that will be experimented with to control the temperature in the wire. The laser must be pulsed so as not to melt the wire, but it must be pulsed fast enough to simulate a heat treatment condition. Determining the correct duration of pulses and the number of pulses will be one of two main factors that define the type of heat treatment that is simulated. Specific heat treatments must be designed to change the properties in the wire. These heat treatments need to produce specific desired properties with repeatable results. There needs to be a sharp contrast between

the heat affected area and the rest of the wire. Also this zone of different properties should be as small as possible. Validation of the model that predicts the temperature of the wire is crucial. Comparing actual experiments to the predictions made by the model is an important step in the validation process.

6 APPROACH

6.1 Heat Transfer Model

6.1.1 Governing Equations

To predict the temperature distribution in a SMA wire during the heat treatment a finite element model is constructed. The wire is modeled as a one-dimensional heat transfer problem along the length of the wire. The assumptions in the model are as follows:

1. Heat transfer is 1-D along the length of the wire
2. Heating caused by the laser beam is homogeneous through thickness of the wire
3. The temperature distribution in each finite element is linear
4. Only natural convection is occurring around the wire during heat treatment
5. Heat transfer tip effects are negligible in this model

Each assumption above is built into the heat transfer model. These assumptions help to simplify the model as well as make it a more accurate model. Also built into the model are the boundary conditions of this wire. The conditions are as follows:

1. Initially the wire is completely surrounded by ambient gas at standard temperature and pressure
2. The temperature of the gas around heated sections of the wire will be assumed to be an average of ambient temperatures and the temperature of that section of wire
3. The wire is not in contact with any other solid heat conducting body, due to the length of the wire and the small size of the section that is treated

Figure 18, below, shows an example of the simplified finite element model. The generalized single element used in the finite element model is shown below in Figure 19.

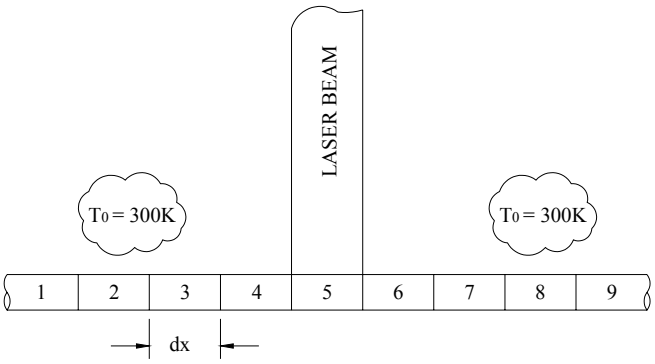

Figure 18. Simplified finite element model of SMA wire with laser beam.

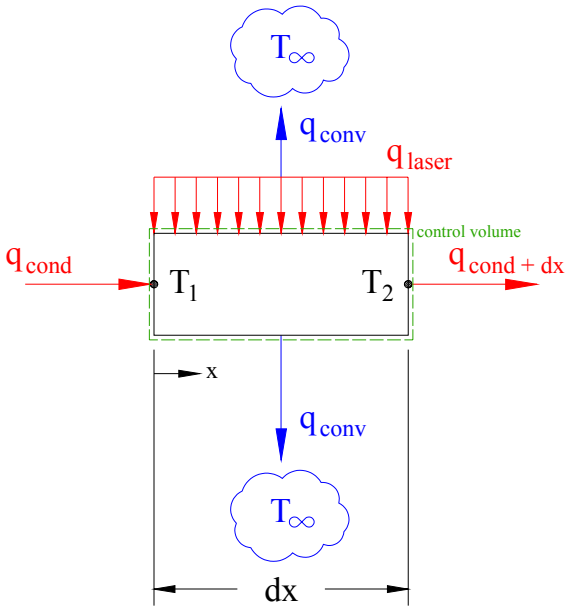

Figure 19. Single element used to calculate the heat distribution in the wire.

Where q_{cond} is the conduction from an adjacent element into the control volume, and $q_{cond+dx}$ is the conduction out of the control volume into an adjacent element. Each q_{conv} represents the convection to the environment which is at the temperature T_∞, note that in the following derivation the q_{conv} term is treated as one general term, not two separate terms. Lastly, the q_{laser} term is the energy input to the control volume due to the laser beam on the surface of the wire. In the following derivation, the q_{laser} will be treated as energy generated inside the control volume, since the laser is assumed to be absorbed uniformly in the volume due to the small wire diameters used in this research. The following is a derivation of the

local matrices that describe the heat transfer in and out of the control volume. First begin with the basic energy equation:

(1) $$E_{in} + E_g - E_{out} = E_{st}$$

Where: E_{in} = Energy into control volume [W]

E_g = Energy generated inside control volume [W]

E_{out} = Energy out of control volume [W]

E_{st} = Energy stored [W]

Substituting in for these values from Figure 19:

(2) $$\underbrace{q_{cond} + q_{laser}}_{E_{in}} \underbrace{- q_{cond+dx} - q_{conv}}_{E_{out}} = E_{st}$$

Each of the components in Equation 2 can be expanded into:

(3) $$q_{cond} = -k\frac{\partial T}{\partial x}Adt$$

(4) $$q_{cond+dx} = q_{cond} + \frac{\partial q_{cond}}{\partial x}dx$$

(5) $$q_{laser} = Q_{laser}Adxdt$$

(6) $$q_{conv} = h(T(x,t) - T_{\infty})Pdxdt$$

(7) $$c_p(\rho Adx)dT$$

Where: A = Cross-sectional area of the SMA wire [m^2]

c_p = Specific heat of wire [J/(kg*K)]

h = Convection coefficient [W/(m^2*K)]

k = Thermal conductivity [W/(m*K)]

Q_{laser} = Volumetric laser power [W/m^3]

T = Temperature of a particular point [K]

T_{∞} = Ambient temperature [K]

t = Time [s]

x = Position along wire [m]

ρ = Density of SMA wire [kg/m^3]

Combining Equations 2, 3, 4, 5, 6, and 7 the equation for heat transfer in the wire is realized in Equation 8.

(8)

$$E_{st} = -k\frac{\partial T}{\partial x}Adt + Q_{laser}Adxdt - \left(-k\frac{\partial T}{\partial x}Adt + \frac{\partial}{\partial x}\left(-k\frac{\partial T}{\partial x}Adt\right)dx\right) - \left(h\left(T(x,t) - T_{\infty}\right)Pdxdt\right) = c_p\rho AdxdT$$

Simplifying and dividing through by "Adxdt" to eliminate common terms:

(9) $$Q_{laser} + \frac{\partial}{\partial x}\left(k\frac{\partial T}{\partial x}\right) - \frac{hP}{A}\left(T(x,t) - T_{\infty}\right) = c_p\rho\frac{dT}{dt}$$

The temperature distribution is assumed to be linear in the each finite element. When this approximate solution is substituted into the governing differential equation, Equation 9, an error will result. In order to try and drive this error to zero, Galerkin's Method of Weighted Residuals (GMWR) is employed. Let the linear shape function be:

(10) $$N = \left[1 - \frac{\hat{x}}{L}, \frac{\hat{x}}{L}\right]$$

Where: $\hat{x}$ = Distance from left side of finite element [m]

L = Total length of finite element [m]

The result of applying the GMWR to Equation 9 will result in the rearranged Equation 11. This derivation can be found in Appendix 11.5.

(11) $$\begin{Bmatrix} c_1 \left.\frac{\partial \Psi}{\partial \hat{x}}\right|_{\hat{x}=\hat{x}_i} \\ -c_1 \left.\frac{\partial \Psi}{\partial \hat{x}}\right|_{\hat{x}=\hat{x}j} \end{Bmatrix} + \underbrace{\frac{c_1}{L}\begin{bmatrix} 1 & -1 \\ -1 & 1 \end{bmatrix}}_{[K]_{c_1}} \begin{Bmatrix} \Psi_i \\ \Psi_j \end{Bmatrix} - \underbrace{\frac{c_2 L}{6}\begin{bmatrix} 2 & 1 \\ 1 & 2 \end{bmatrix}}_{[K]_{c_2}} \begin{Bmatrix} \Psi_i \\ \Psi_j \end{Bmatrix} = \underbrace{\frac{c_3 L}{2}\begin{bmatrix} 1 \\ 1 \end{bmatrix}}_{[F]} + \underbrace{\frac{c_4 L}{2}\frac{\partial \Psi}{\partial t}\begin{bmatrix} 1 \\ 1 \end{bmatrix}}_{[C]}$$

Combining like terms in Equation 11 and plugging in for c_1, c_2, c_3, c_4, and Ψ yeilds:

(12) $$\begin{Bmatrix} k \left.\frac{\partial T}{\partial x}\right|_{x=x_i} \\ -k \left.\frac{\partial T}{\partial x}\right|_{x=xj} \end{Bmatrix} + \left\{ [K]_{c_1} + [K]_{c_2} \right\} \begin{Bmatrix} T_i \\ T_j \end{Bmatrix} = [F] + [C] \begin{Bmatrix} \frac{\partial T_i}{\partial t} \\ \frac{\partial T_j}{\partial t} \end{Bmatrix}$$

Where: $$[K]_{c_1} = \frac{k}{L}\begin{bmatrix} 1 & -1 \\ -1 & 1 \end{bmatrix}$$

$$[K]_{c_2} = \frac{hPL}{6A}\begin{bmatrix} 2 & 1 \\ 1 & 2 \end{bmatrix}$$

$$[F] = \left(\frac{hPL}{2A} T_\infty + \frac{L}{2} Q_{laser} \right) \begin{bmatrix} 1 \\ 1 \end{bmatrix}$$

$$[C] = \left(\frac{c_p \rho L}{2} \right) \begin{bmatrix} 1 \\ 1 \end{bmatrix}$$

For the finite elements at the ends of the wire the end effects are ignored due the long length of the wire compared to the cross-sectional area, as well as a small cross-sectional area due to the small diameter of the thin wire. Therefore, the first term in Equation 12 is neglected and the general form of Equation 12 is realized as $[K]^e[T] = [F]^e + [C]^e[dT/dt]$. The equation for the elemental conduction matrix is shown below in Equation 13.

(13) $$[K]^e = \frac{k}{L}\begin{bmatrix} 1 & -1 \\ -1 & 1 \end{bmatrix} + \frac{hPL}{6A}\begin{bmatrix} 2 & 1 \\ 1 & 2 \end{bmatrix}$$

The elemental force matrix is shown below as Equation 14.

(14) $$[F]^e = \left(\frac{hPL}{2A} T_\infty + \frac{L}{2} Q_{laser} \right) \begin{bmatrix} 1 \\ 1 \end{bmatrix}$$

Elemental condition matrix is shown below in Equation 15.

(15) $$[C]^e = \left(\frac{c_p \rho L}{2} \right) \begin{bmatrix} 1 \\ 1 \end{bmatrix}$$

Elemental temperature matrix is shown below in Equation 16.

(16) $$[T]^e = \begin{bmatrix} T_i \\ T_j \end{bmatrix}$$

The elemental change in temperature with respect to time matrix is shown in Equation 17.

(17) $$\left[\frac{\partial T}{\partial t} \right] = \begin{bmatrix} \frac{\partial T_i}{\partial t} \\ \frac{\partial T_j}{\partial t} \end{bmatrix}$$

Equations 13 through 17 are the core elemental matrices used to construct the global matrices that will represent the heat transfer in the entire wire as a summation of its individual elements. The construction of the global matrix for the wire is actually quite simple. A five element example is give below in Figure 20.

Once the global matrices are formed, the temperature distribution must be determined. Matrix operations can be used to solve the global matrices for the heat transfer equation. The general form of the global matrices is $[K]^g[T] = [F]^g + [C]^g[dT/dt]$. Solve for the change in temperature with respect to time, as shown below.

(18) $$\frac{\partial T}{\partial t} = \frac{[K]^g}{[C]^g}[T] - \frac{[F]^g}{[C]^g}$$

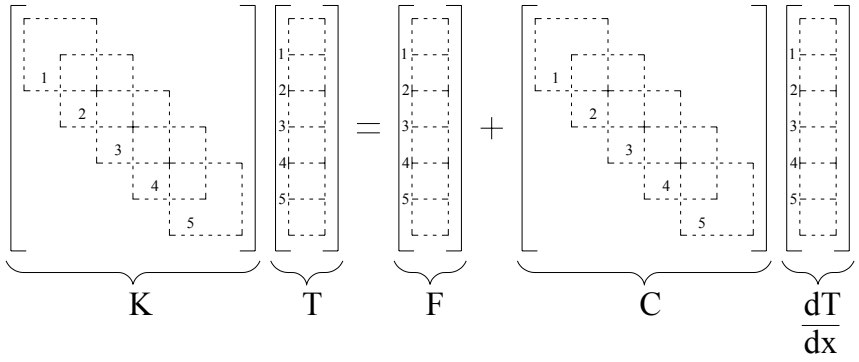

Figure 20. Assembly of the global matrix for a simple four element wire.

Once this is accomplished, a numerical integration technique can be used to solve for the temperature distribution of the wire over time. The only requirement is the initial state of the wire. This will generally be ambient temperature. All the mathematical calculations and finite element analysis are computed with Matlab. The numerical integration is also done using a predefined differential equation solver in Matlab.

6.1.2 Convective Heat Transfer in Model

Another major component in determining the temperature distribution in the wire is determining the convection coefficient. This can be tricky since portions of the wire must heat up well above ambient temperature. The difference in surface temperature of the wire and ambient temperature will obviously cause natural convection, which has already been stated as one of the most significant cooling mode in thin wires for the setup studied in this research. The convection coefficient will change significantly along the wire and in time as the wire heats up. Therefore, in the finite element program the coefficient must be calculated in time using the previous temperature of each finite element. The formula used to determine the convection coefficient for a cylinder is shown below in Equation 19. (Shu *et al.*, 1997)

(19) $$h_c(T,d) = \frac{k_{air}}{d} Nu$$

Where: $$Nu = \left[\alpha_1 + \alpha_2 \left\{ \frac{GrPr}{\left[1 + (0.56/Pr)^{9/16}\right]^{16/9}} \right\}^{1/6} \right]^2$$

$$Gr = \frac{1}{1/2(T + T_\infty)}(T - T_\infty)\frac{gd^3}{\upsilon^2}$$

$$Pr = \frac{\mu C_p}{k_{air}}$$

Let d be the diameter of the SMA wire, α_1 and α_2 be experimental derived constants, g is gravity, μ is the viscosity of helium, υ is the kinematic viscosity of helium, C_p is the heat capacity at constant pressure, k_{helium} is the thermal conductivity of helium, Nu is the Nusselt number, Gr is the Grashof number, and Pr Prandtl number. It should be noted that the viscosity, kinematic viscosity, and heat capacity of helium also change with temperature. These values are generally looked up in a table, but for the finite element program to use them in the solver the table of values must be plotted. Curve fitting of these plots was done to establish an equation to determine these values at any temperature between 100K and 2000K. The equations are given below.

(20) $$\mu = (4.5905 * T^{0.6619}) * 10^{-7} \ [N*s/m^2]$$

(21) $$\upsilon = (0.0095 * T^{1.6612}) * 10^{-6} \ [m^2/s]$$

(21) $$C_p = 0.519395 \ [KJ/(kg*K)]$$

(23) $$k_{helium} = (2.7836 * T^{0.7024}) * 10^{-3} \ [W/(m*K)]$$

The temperature, T, used in the above four equations is an average temperature of the wire surface temperature and the ambient helium temperature at that particular finite element. When Equations 19, 20, 21, 22, and 23 are combined the convection coefficient can be calculated for each element at any particular instant in time.

6.1.3 Gaussian Beam Profile

Another important aspect in the heat transfer model is the amount of the laser beam that is actually covering the SMA wire, as well as the profile of the laser beam. Generally the laser beam's diameter will be greater than that of the SMA wire, since the wires are so thin. Therefore, the actual amount of the beam covering the laser must be determined. This problem can be visualized in Figure 21.

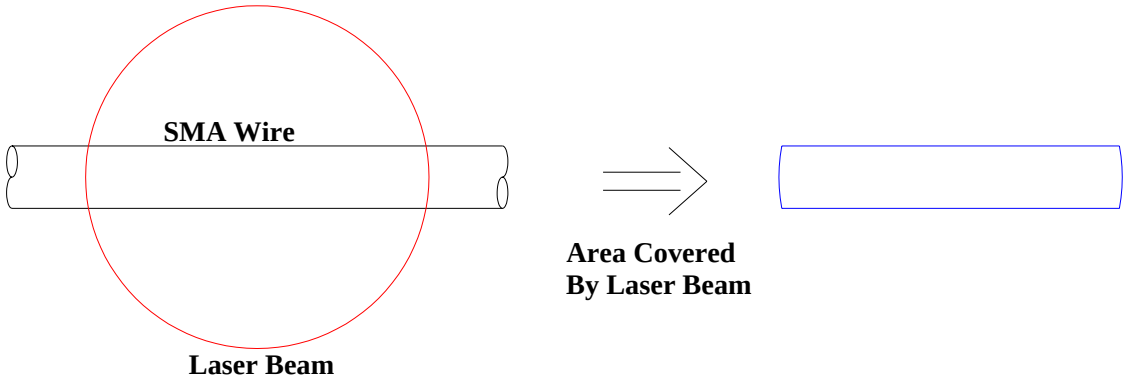

Figure 21. The portion of the laser beam covering the wire.

Also, the profile of the beam in terms of power density is not uniform over the laser beam coverage area. The profile of the Ytterbium fiber laser used in this research has a single mode Gaussian distribution, as shown in Figure 22. This is the 5mm diameter collimated beam, and from Figure 22 the Gaussian distribution is quite apparent. This distribution is advantageous because the energy input from the laser beam is very predictable, and with precision heat treatment this is a very important aspect. If the heating is multiple mode then different parts of the treated region will be at different temperatures, which will yield varying results across the wire. Also, without the aid of special, complicated optics there is not an industrial laser that can produce a high power laser beam with uniform power density across its profile, and most typical, high powered lasers actually have multiple modes in their profile that would definitely cause uneven heating in a heat treatment. But as Figure 22 shows, the power distribution is a single mode for this particular laser.

While the Gaussian beam profile is very desirable it also presents a problem when developing the heat transfer model for the SMA wire. If the diameter of the wire or the finite elements is smaller than the diameter of the spot size, then the beam must be segmented to determine the amount of energy input into that particular finite element. For this research the wires are typically thinner than the spot size, and it is desirable for finite elements to be small to increase the accuracy of the simulated results. Therefore the segmentation of the beam profile must be addressed.

It would be quite easy to model this beam with a beam profiler, but this is a very expensive tool and the funds are not available for this. But, the manufacturer of the laser, IPG

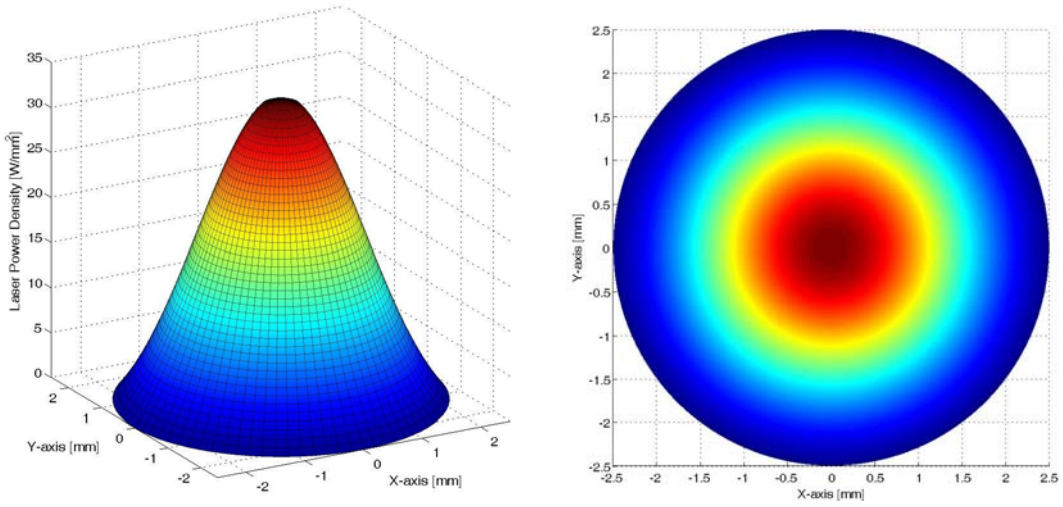

Figure 22. The theoretical profile for the laser beam in terms of power density, and this particular profile represents a 5mm diameter, collimated beam at 300W laser power.

Photonics, boast that the beam profile is very close to Gaussian, therefore this assumption will be made and the equation for a Gaussian curve is shown below in Equation 24.

(24) $$z(x) = c_1 e^{-c_2 x^2} \text{ or } z(y) = c_1 e^{-c_2 y^2}$$

Let c_1 and c_2 be constants that can adjust the height and width of the Gaussian beam, respectively, and the equations for these are dependent solely on laser power and beam diameter. Note that c_1 and c_2 in each individual equation, respectively, will be the same since the laser beam is assumed to be round and uniform. Equation 24 obviously describes the Gaussian curve in either the Z-X plane or the Z-Y plane. When c_1 and c_2 are unity the curves are of that as shown in Figure 23, and it is easy to notice from Equation 24 or Figure 23 that the curves are exponentials and will never actually intersect the abscissa. This brings up the question of where is the actual cutoff that defines the diameter of the laser beam as shown in Figure 22. According to Sharp, the actual beam diameter should be defined as that distance within which $1/e^2$ of the total power exists. (Sharp *et al.*, 1983) This is shown on Figure 23 as a horizontal red line. Above this line is considered to be the beam profile, and that below the line is neglected. As mentioned above, the constants c_1 and c_2 in Equation 24 are used to adjust the height and width of the Gaussian beam, and these constants depend on the laser

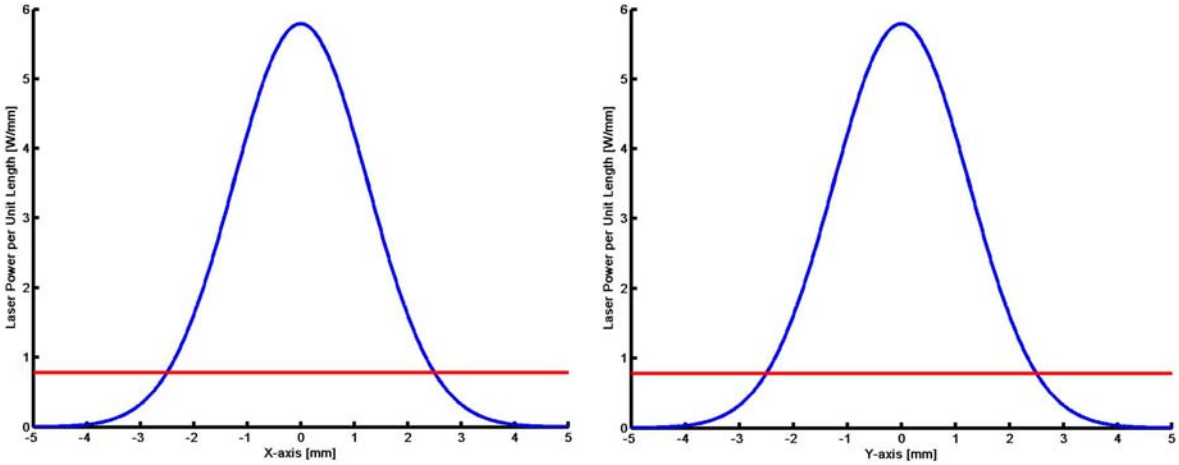

Figure 23. A typical Gaussian curve in Z-X plane and Z-Y plane, respectively.

power and the desired beam diameter. The derivation of these constants is shown in Appendix 11.6.

Now that c_1 and c_2 have been solved, Equation 25 can be used to determine the power in any segment of the laser beam by simply controlling the limits of integration in the equation. This tool allows for a more accurate heat transfer model because the theoretical amount of laser power applied to each individual element is known. Figure 24, below, shows an example of a segment of the laser beam that might be applied to one finite element in the wire.

(25) $$P = c_1^{\,2}\left(\int e^{-c_2 x^2}\,dx\right)\left(\int e^{-c_2 y^2}\,dy\right)$$

6.1.4 Thermocouples in Heat Transfer Model

Since it is already known that the temperature of the wire is going to be measured by a thermocouple, the heat transfer model should be adjusted to include this. The reason behind adding the thermocouples in the model is, a thermocouple is a contact type of measuring device, thus it must extract some energy from the wire in order to make a measurement. This energy would have originally propagated down the wire, but since it is extracted by the thermocouple, the overall temperature of the wire will be slightly lower. The design of a thermocouple is such that this measurement will not cause a significant amount of error. However, in a precision heat treatment model, it can prove useful to account for these

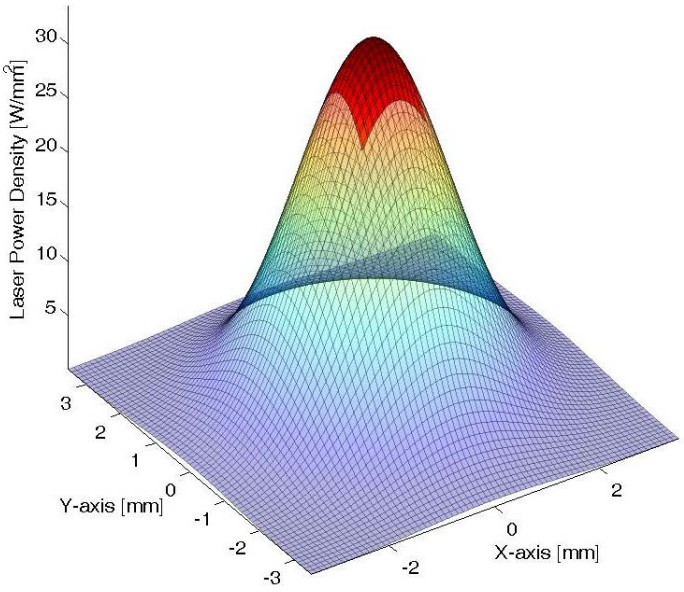

Figure 24. An example of segregation of the Gaussian laser beam profile.

additional heat losses. The adjustment to the heat transfer model is shown in Appendix 11.7. The new single element equation, similar to that of Equation 12, shown in the Section 6.1.1., above, is:

(26)
$$\begin{Bmatrix} k\left.\frac{\partial T}{\partial x}\right|_{x=x_i} \\ -k\left.\frac{\partial T}{\partial x}\right|_{x=xj} \end{Bmatrix} + \left\{[K]_{c_1} + [K]_{c_2} + [K]_{c_5}\right\}\begin{Bmatrix} T_i \\ T_j \end{Bmatrix} = [F] + [C]\begin{Bmatrix} \frac{\partial T_i}{\partial t} \\ \frac{\partial T_j}{\partial t} \end{Bmatrix}$$

Where:
$$[K]_{c_1} = \frac{k}{L}\begin{bmatrix} 1 & -1 \\ -1 & 1 \end{bmatrix}$$

$$[K]_{c_2} = \frac{hPL}{6A}\begin{bmatrix} 2 & 1 \\ 1 & 2 \end{bmatrix}$$

$$[K]_{c_5} = \frac{k_t PL}{2rA}\begin{bmatrix} -1 & 1 \\ -1 & 1 \end{bmatrix}$$

$$[F] = \left(\frac{hPL}{2A}T_\infty + \frac{L}{2}Q_{laser}\right)\begin{bmatrix} 1 \\ 1 \end{bmatrix}$$

$$[C] = \left(\frac{c_p \rho L}{2}\right)\begin{bmatrix} 1 \\ 1 \end{bmatrix}$$

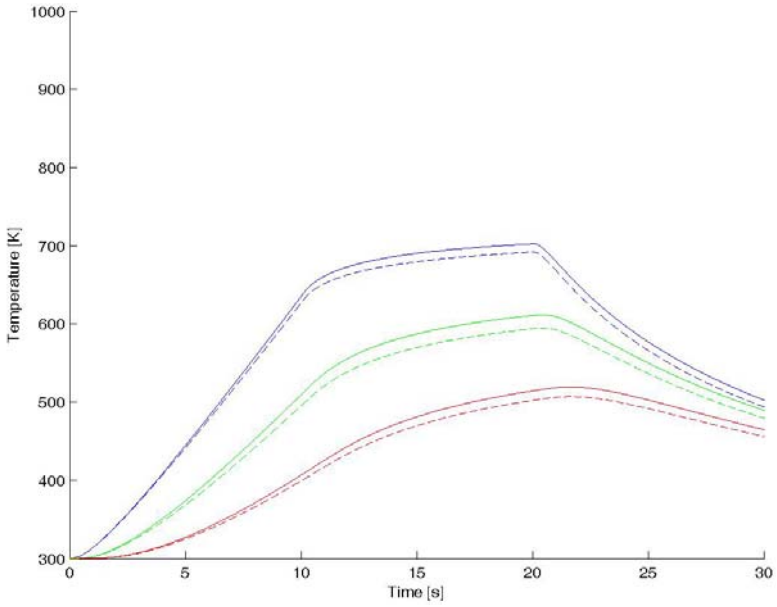

Figure 25. Effect on heat transfer due to the use of thermocouples.

The global equations are built the same way as shown in Section 6.1.1., above. An initial heat treatment scenario was simulated to determine the effect of the thermocouples. Figure 25 shows the comparison of a wire simulated without thermocouples and one simulated with a thermocouple at 5mm away for the center of beam application. The solid lines represent the temperature distribution in the wire without the effects of thermocouples. The dashed lines on the other hand represent the temperature distribution in the wire with the effects of thermocouples. Furthermore, the different colors represents the temperature of the wire at specific distances from the center of laser application where: blue is for 3mm, green is for 5mm, and red is for 8mm from the center of application. From Figure 25 it is easy to see that the thermocouple effects are quite minimal. The temperature difference between the two cases for the whole wire is generally less than 0.5% for the use of one thermocouple. For the particular case shown in Figure 25, it is 0.36%. The addition of multiple thermocouples will obviously increase the temperature difference due more energy being removed for each measurement.

While the effects of adding one thermocouple are quite minimal, several thermocouples could cause a significant decrease in wire temperature. Since the goal of this model is to preciously predict temperature distribution in the wire, it is desirable to model the effects of these thermocouples, even if the effect is quite small.

6.1.5 Basic Matlab Heat Transfer Model

The above sections are combined into a unified program in Matlab. This basic model allows one to input all the characteristics of the wire that will be heat treated, as well as the characteristics of the laser setup. A switch profile, a vector defining at what time to turn the laser emission on or off, must be supplied for the laser to operate in a desired fashion. The simulation can then be ran, and the result will be a solution for the temperature distribution in the wire, which is defined at any time step and finite element. With Matlab's graphical display capabilities, several different types of plots can be constructed to visualize the temperature distribution. These will be discussed in further detail when the final heat transfer Matlab model is presented. There are two important constant in the Matlab model that are not easily obtainable. The first one is the absorption of the laser beam. Understanding exactly how much of the laser beam is absorbed by the wire requires expensive equipment and extensive analysis. Similarly, understanding how much convection is occurring at different sections in the wire and how the convection coefficient changes with temperature requires much theoretical analysis. For the latter, an equation has been presented to determine the convection coefficient. In this equation lie two constants that are experimentally determined. Initially an educated guess is used to define the absorption and the convection coefficients. Then a series of validation experiments was completed in which the fine tuning of these values occurs. This will be discussed in Section 6.5. Note, the Matlab code for the final version of the laser treatment model is found in Appendix 11.8.

6.2 Laser Treatment Model and Laser Control

6.2.1 Advanced Features of Laser Treatment Model

The basic Matlab heat transfer model can be modified so that the program itself is capable of controlling the laser, having advanced heat treatment features, and be a more robust model. This section discusses some of the added features available with the most up to date version of the heat treatment program.

The first major improvement is a temperature distribution that is generated by the model which is continuous along the length of the wire and in time. This allows for two very beneficial graphical outputs. One, after the model has generated the continuous solution, different points or regions anywhere on the wire can be singled out and the temperature

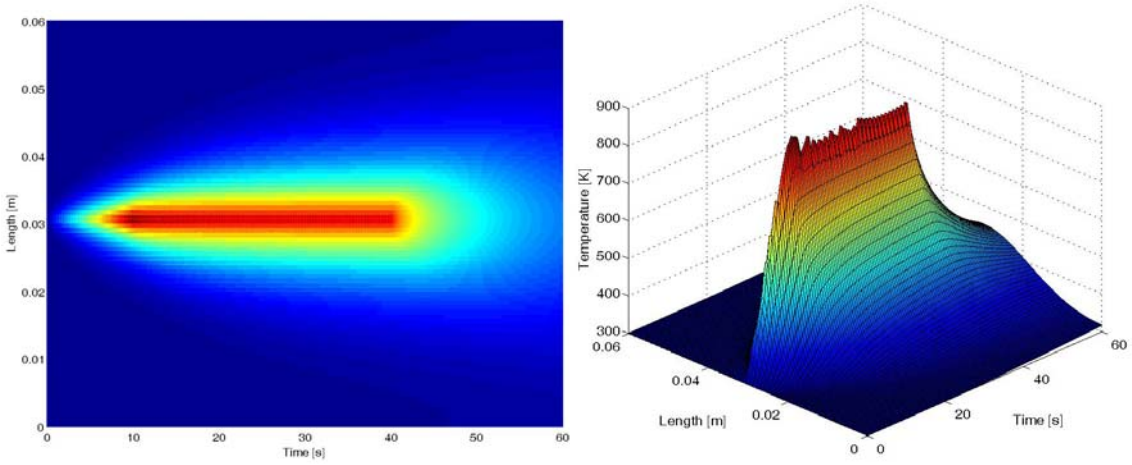

Figure 26. Temperature distribution in a wire plotted in time.

history for that particular point or region can be visualized in time. Two, the complete 3-D temperature distribution in the wire can be visualized where the xyz axes are: wire position, temperature, and time, respectively. Figure 26 gives a good example for a simple heat treatment.

The ability to calculate the convection coefficient "on-the-fly" is another important feature. This means that the program automatically changes the natural convection value in the model while the continuous solution for wire is being built. Several temperature dependent variables for helium such as kinematic viscosity, heat capacity, viscosity, and thermal conductivity are required to determine the convection coefficient. These variables are normally referenced from a table, but these tables have been incorporated into the computer code to make the program more robust.

The model also has the ability to simulate the effect of scanning the laser beam along the length of the wire, thus the laser beam moves a certain distance at a certain speed on the wire. Figure 27 is much like Figure 26, but now scanning has been incorporated. The importance of scanning is realized when a particular area to be heat treated is too large for a spot size with proper power density to be achieved. This situation is likely to be encountered when this process is implemented to produce commercial devices. For example, if a 5mm treated area is required on a wire that is 1mm in diameter the spot size would have to be increased to 5mm. In this situation there is a large area of the beam power that is not actually applied to the treated region, and the power of the laser would have to be increased to

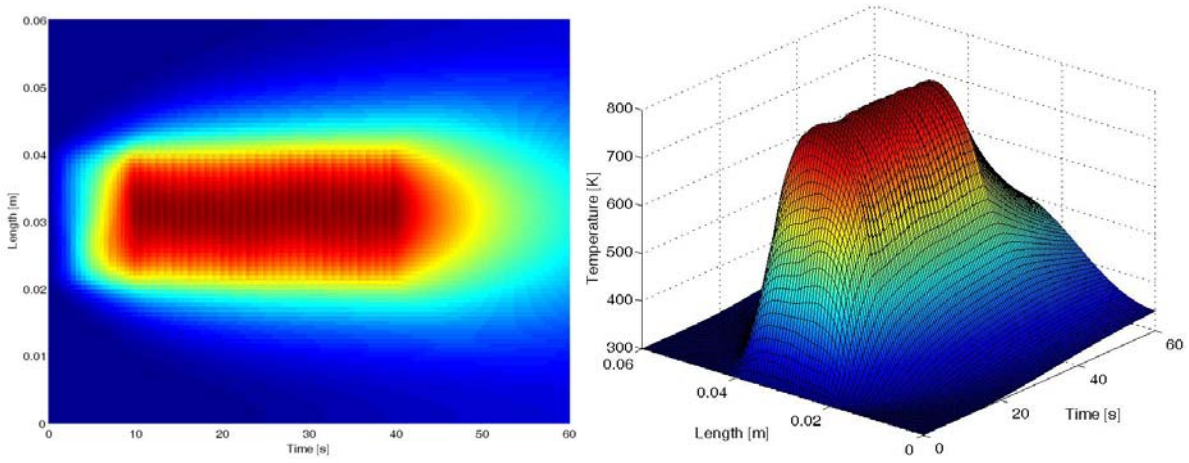

Figure 27. Temperature distribution of a laser scanned wire plotted in time.

compensate for this lack of energy input. Both of these combined create a drastic decrease in the laser treatment's efficiency. Since even the best lasers are only 20% efficient in terms of power consumption to output, wasting even more energy in the treatment process is not an option. Therefore, a smaller spot size could be scanned, and not only would more of the laser's beam be used, but the laser would run at a lower power, thus consuming less energy. This is an important issue to consider because it conveys the importance of this scanning feature.

The new model allows for the definition of a heat treatment profile instead of just a profile switching vector. Figure 28 is used to aid in the visualization of the characteristics of a particular heat treatment that is automatically generated by this computer model. The heat treatment is typically defined by three distinct stages: Heat-Up stage, Soak stage, and Cool-Down stage. The Heat-Up and Cool-Down stages are defined by the user with any two of these three characteristics: target temperature, time of stage, and rate of stage. The Soak stage is simply defined by a time, and is held at the target temperature for the proceeding Heat-Up stage. The user can create successive groups of these three stages, which can create virtually any kind of heat treatment desired. There is also a user defined temperature bandwidth for the entire heat treatment that acts like a temperature tolerance, and it is used by the model to determine when the laser should be in a 'high" state or "low" state as to conform to the desired heat treatment. For each stage in the heat treatment the laser's power values for the high and low states can be set. Also in each stage the laser beam's pulsing can be defined

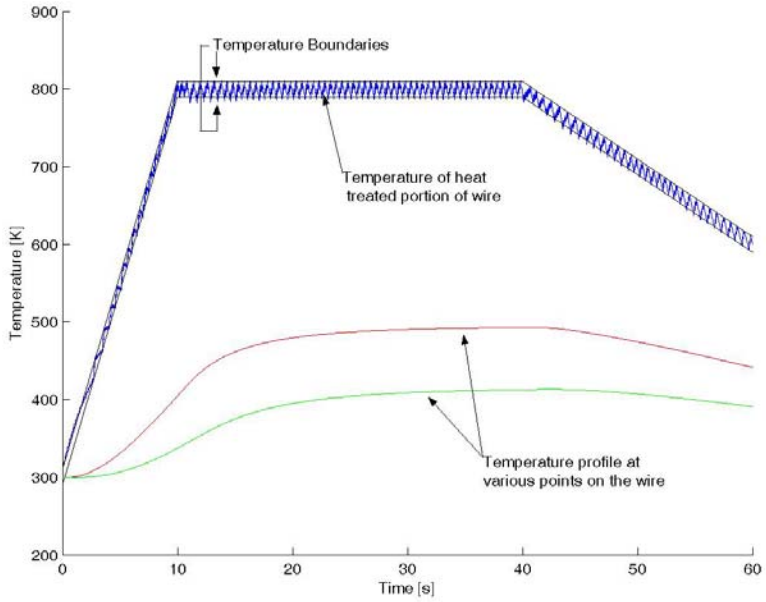

Figure 28. Heat treatment generated by the computer model.

with a unique pulse period and pulse width. The laser beam pulsing works in conjunction with the switching, and is discussed in detail in the next section.

Finally, any temperature measurements that has been acquired by the real-time data acquisition system during a heat treatment is directly loaded by Matlab and plotted against the predicted value to verify that the model is working correctly. This is how the model will be validated.

6.2.2 Implementation of Laser Treatment Model

The laser treatment model must be correctly implemented into a heat treatment setup for it to accurately predict the temperature of the SMA wire as well as control the laser. The actual approach to controlling the laser will be discussed in Section 6.2.3, but the implementation of the laser treatment model is shown below in Figure 29. To examine Figure 29 first look at the "Laser" block. For this block energy is emitted and input into the SMA wire. The same amount of energy is also simulated as an input into the laser treatment model. The laser treatment model uses the energy input to simulate the temperature response of the SMA wire. The output of this block is the predicted temperature in the wire. Offline measurements of the wire's actual temperature are made and compared against the predicted

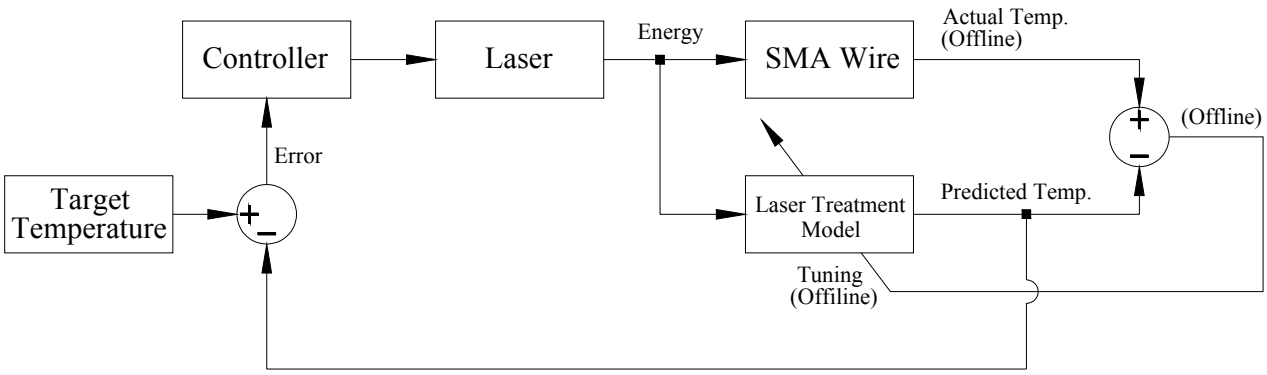

Figure 29. Implementation of laser treatment model in heat treatment system.

temperature. Then offline adjustments are made to the model until there is a minimal difference in these two temperatures. While online, the predicted temperature out of the laser treatment model is compared against the target temperature, which defines the state of the heat treatment for that instant in time. The resulting error of the target temperature and the predicted temperature is input into the controller to adjust the laser's output. The controller will essentially increase output from the laser if there is a positive error, meaning the wire's temperature is lower than the target temperature, or it will decrease the output of the laser if there is a negative error, which is a state where the wire's temperature is too high.

With this particular implementation the laser treatment model is effectively used to control the laser and produce precise heat treatments without having to record online temperature data. This will only works with a valid model that can accurately predict the temperature in the wire during a heat treatment. Thus, the offline measurements are made to hone the model to the correct parameters. Once this is done, complete control of the laser is determined by the laser treatment model.

6.2.3 Controlling the Laser

The laser treatment model is used to predict the outcome of a designed heat treatment, and the switching profile. This profile is essentially a history of when the model switched from the high state to the low state, and vise versa, and this symbolizes when the laser should be turned on and off.

The high/low switching is commonly referred to as a "bang-bang" approach to control. It is an open loop method where the wire's temperature reaches some maximum, the

laser is switched to a low state, and when a minimum temperature is reached the laser is switched back to the high state. This is a simple method that can involve a very high number of switching for one heat treatment. To alleviate some of the extra switching, a pulsed laser beam is introduced into the model since the laser has a 2kHz maximum modulation capability. Essentially, there are now two forms of switching occurring simultaneously. Figure 30 shows how the pulsing occur in conjunction with one another to affectively reduce the number of manual switches required by the laser. The pulsing is simply defined by a pulse period and pulse width, and is held constant for an entire heat treatment stage. This helps to reduce the length of the switching vector, which is the vector of specific times to toggle the laser's state.

While the model creates a switching vector with an implemented pulsing beam, this vector can still consist of a few hundred switches depending on the length, complexity, and temperature tolerance of the heat treatment. This vector, which is the heat treatment characteristics, and the laser pulsing characteristics, must all be converted to computer logic. All of this data must be interpreted by the laser through a serial interface that can accept digital and analog inputs. Connected to this interface is our data acquisition system, D-Space. This unit has many controllable digital and analog I/O ports, it operates in real-time, and is compatible with Simulink files. D-Space is then given specific commands from the Galil motion

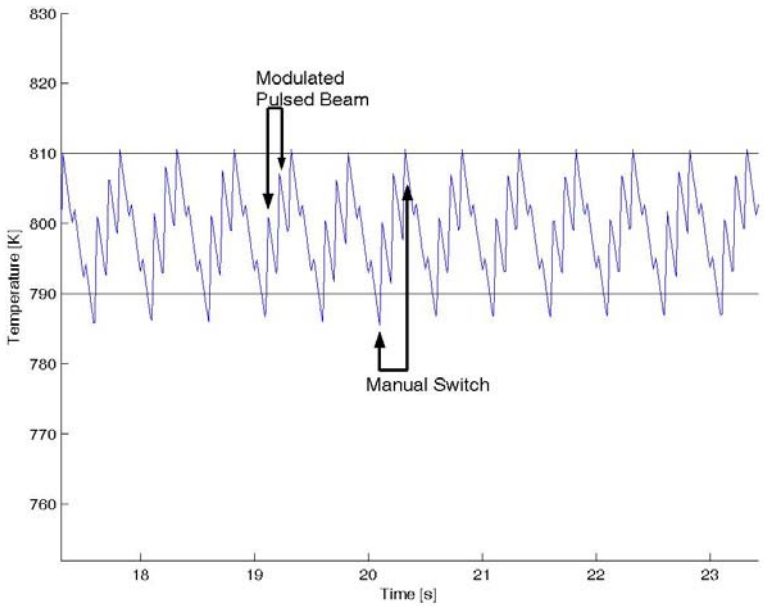

Figure 30. Simultaneous pulsing of laser beam.

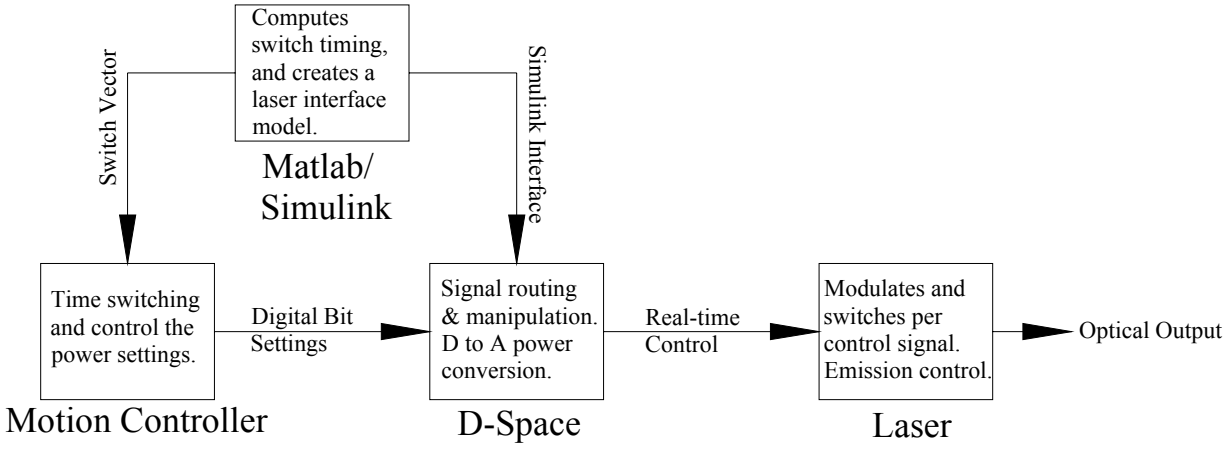

Figure 31. Communication hierarchy for controlling laser.

controller, and this unit allows for bitwise programming, as well as control of the linear motors which is used in scanning the laser beam. Figure 31 is a simplified schematic that shows the communication hierarchy used in controlling the laser. In Figure 31, it can be seen that D-Space is essentially the interpreter between the motion controller, which handles the switch file, and the laser. Matlab and Simulink are used to generate the programs that both the motion controller and D-Space use. The program that goes to the motion controller is a modified version of the switch vector that is generated by the laser treatment model, which has been formatted by another Matlab program to be compatible with the motion controller's program editor. The program simply sets and clears digital bits in D-Space at specifically determined times. The program can also control the motion of the linear motors, but this part of the code is not passed through D-Space. A Simulink model is loaded onto D-Space that essentially reads the incoming digital bits from the motion controller and routes them as designed. Depending on the combination of bits, the laser power is set, the laser is switched on and off, and the laser's modulation capabilities can be set and activated. This Simulink model is shown in Appendix 11.9. D-Space sends the laser digital signals and an analog signal to the serial interface on the laser, where the analog signal sets the output power of the laser. This type of total control of the laser is necessary to produce tailored heat treatments that achieve desirable results.

6.3 Heat Treatment Design

Designing heat treatments for SMA is quite a difficult task. In much of the background research of this thesis, several papers have commented on how much experience is needed to create heat treatments that will produce desirable effects that can be used in practical applications. Two separate papers even went as far as to describe this type of heat treatment design as an art form. While the scope of this research is to develop a tool to produce any desired form of laser heat treatment, designing a heat treatment that will produce some noticeable changes in the SMA is necessary in order to evaluate the initial effectiveness of the new laser heat treatment as a tool.

Superelastic wire has found many commercial uses. Therefore, the first heat treatment should be designed to alter a region of superelastic SMA. This would involve changing the superelastic properties into shape memory properties at room temperature. To do this, an aging process is to be employed. As discussed previously, the wire will be heated to a "soaking" temperature and held for a certain length of time until the proper amount of precipitates has formed. This reduces the amount of Ni that is in the Ti-Ni matrix, thus increasing transition temperatures. Although, these precipitates tend to form on grain boundaries and if too much precipitate is formed, the local stress naturally imposed by these precipitates will become large enough to hinder the martensitic transformation of the SME, and thus strengthen the SE. To determine what the best aging temperature and time is, a series of experiments can be performed, and these two parameters can be systematically varied. The idea is to look for the combination of soaking time and soaking temperature where the SME becomes more and more present, and then starts to decline due to this over development of precipitates.

A general heat treatment profile is shown below in Figure 32. This is rather typical for aging treatments. Due to the slower formation rate of precipitates, the soak time is going to be much longer than that of heat-up time. Also the cool down time is insignificant and is usually just an air cool, due to the natural occurrence of precipitation in Ni-rich SMA at elevated temperatures. If the wire is cooled down too fast then not all the possible precipitates will form. These are some basic considerations that must be made when designing SMA heat treatments.

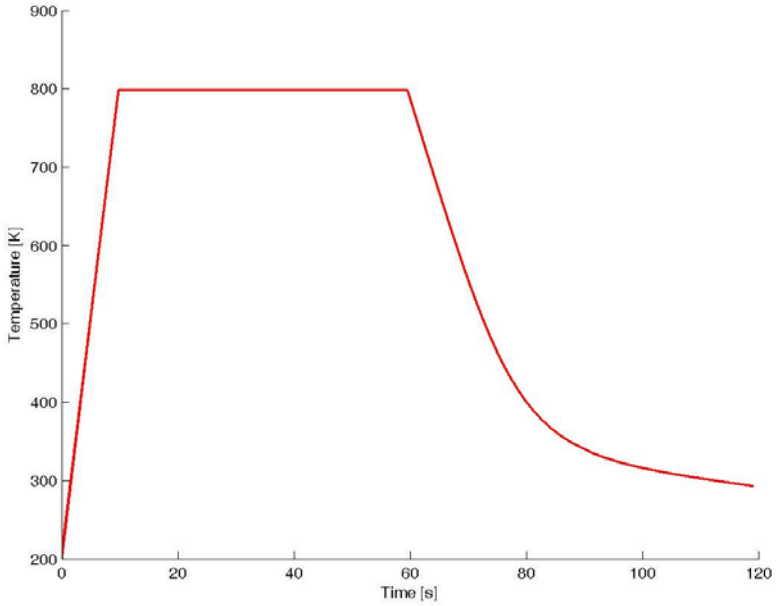

Figure 32. General aging heat treatment profile.

Extra considerations must be made when designing heat treatments that utilize a laser. The power density must not be overlooked when designing the treatment. Due to the high power of the laser, if this is not properly accounted for then melting can quickly occur and destroy the workpiece. Also, the length of the heat treatment should be shorter; the added power density increases the growth rate of the precipitate, and this accelerated growth should be confined to only the desired area by increasing power and lowering aging time. Due to the inefficiency of the laser the power consumption will become a factor, especially if this process is to be used for commercial products. The above information provides background on the considerations for laser heat treatments as well as the direction in which each should be approached.

6.4 Experimental Setup

6.4.1 Laser Workstation

One of the defining aspects of this research is the use of a laser beam to accurately heat treat a small portion of the wire. Therefore a sufficient laser workstation must be assembled to efficiently and accurately provide a laser energy source to the wire surface. The foundation of the workstation used for this research is a Vibraplane vibration isolation table (as known as an optical table) by Kinetic Systems. The table is supported by four gas

Figure 33. Vibraplane® optical table by Kinetic Systems.

pressurized legs, feed by a high purity nitrogen tank, to isolate any vibrations in the floor from the table surface. Due the small spot size of the laser beam and the small diameter of the wire, any vibration could cause the laser beam to shake away from the wire. This would cause ineffective heat treatment.

The laser that supplies the power is a 300W Ytterbium fiber laser, model YLR-300-AC, constructed by IPG Photonics. The laser beam is delivered through a 3 meter shielded, fiber cable to an aluminum structure attached to the optical table. The laser shines down perpendicularly from roughly a meter above the table surface. When the laser beam exits the collimator there is practically no divergence or convergence of the laser beam. Therefore, the focal point is theoretically infinity, and the beam diameter is 5mm. The wavelength of the beam is 1075nm. The advantage of using the fiber laser is the single mode beam profile. The laser beam has a distinct Gaussian beam profile, as shown in Figure 22 in Section 6.1.3, and this is important due to the nature of the research. As previously stated, if a laser heat treatment is to be applied accurately and precisely, a multimode beam will not give uniform heat input and can cause varying energy input across the wire, thus the properties of the treated region may vary due to the non-uniform energy input.

The beam is the passed into a beam expander, made by Linos, and expanded by five times. When the beam exits the beam expander the laser beam again has a focal length of infinity. Then the beam is passed through a single 50mm diameter plano-convex Gradium® focusing lens with a 150mm effective focal length, manufactured by LigthPath Technologies.

Figure 34. 300 Watt Ytterbium fiber laser by IPG Photonics.

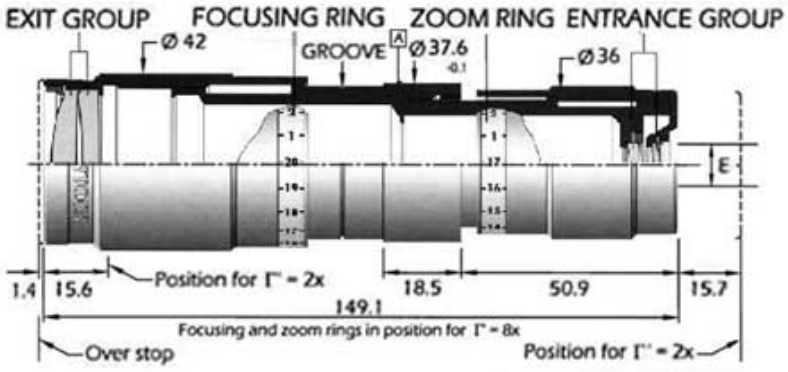

Figure 35. Beam expander by Linos.

The beam expander and focusing lens are attached to a three axis adjustable linear stage. The linear stage is attached to another, separate aluminum structure also secured to the optical table. The linear stage is a PT3/M 25mm travel linear translator, manufactured by Thor Labs. Each axis has a range of 25mm and is controlled manually by a micrometer style positioner. The linear stages help to insure that the laser beam out of the collimator is directed to the center of the beam expander and that the focal point of the laser beam is precisely at the desired height. The analog style positioners allow for exact positioning of the laser beam without the added cost, equipment, and computer burden of piezoelectric positioners, which have become quite popular in precision adjustment. Since there are no necessary adjustments to the linear stages need during a heat treatment, piezoelectric positioners would offer no benefit to this research.

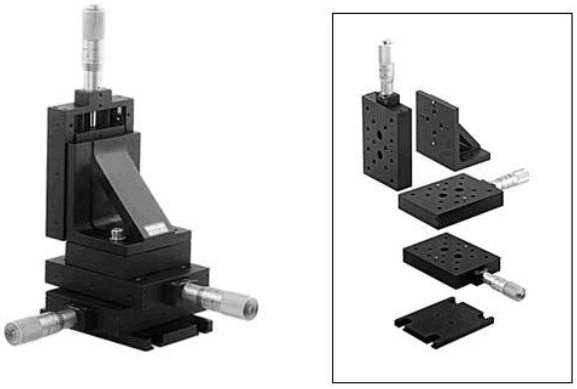

Figure 36. Three axis analog linear stages by Thor Labs.

Figure 37. Focusing optics assembly.

In between the two aluminum structures that support the collimator and focusing lens are two linear motor slides, attached to the optical table. The motors are step up in an X-Y configuration, if the Z axis is assumed to be perpendicular to the work table surface. The motors and motor amplifiers are manufactured by Parker Automation and the motors have a 0.5 micron resolution with a range of 40cm in either direction. The motors are controlled by a Galil motion control card integrated into a PC. Figure 38 shows the schematic of the motor on the right and the actual setup of two motors stacked in an X-Y configuration on the optical table. On top of the motors is a 300mm x 300mm Thor Labs anodized bread-board with 144 tapped M6 holes, and this plate is generally used to attach all different types of workpieces

Figure 38. Two single axis linear motors by Parker Automation.

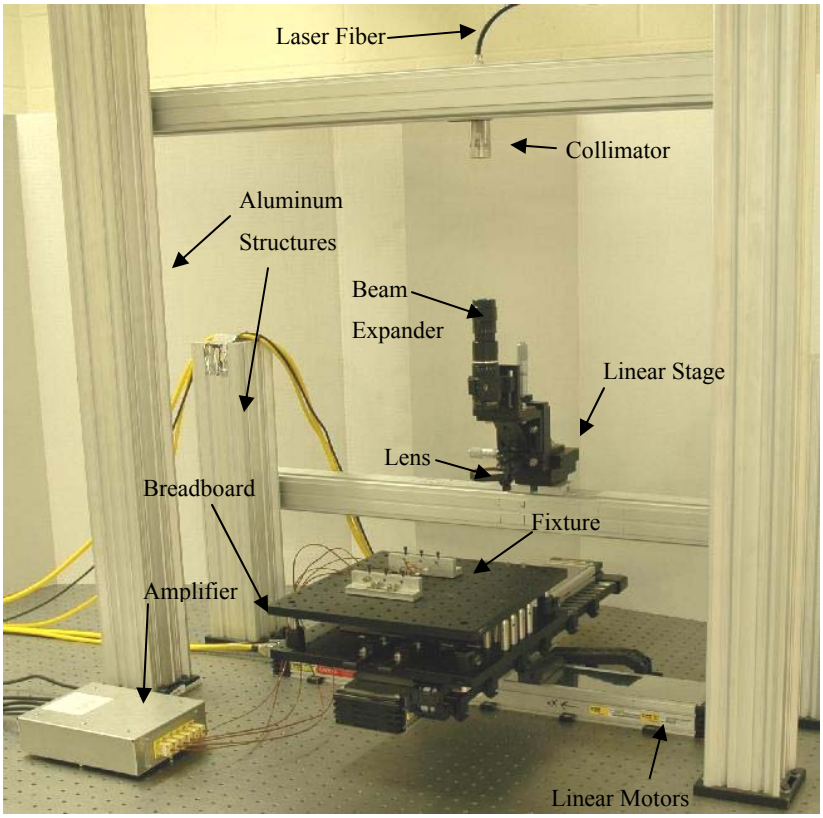

Figure 39. Entire laboratory setup.

and fixtures. In Section 6.4.2, the different types of fixtures will be discussed. The entire lab setup is shown in Figure 39. The setup in Figure 39 is the current setup used in this research and can provide accurate and precise heat treatment to shape memory alloys. Two PCs and D-Space are used to record data and control this system. The two PCs have a Galil control card and proprietary software on them to control the linear motors and the laser. D-Space, which will be discussed in more detail in Section 6.4.3, is used to record all the data from thermocouples.

6.4.2 Fixtures

In order to perform the different heat treatments and measurements necessary for this research, different fixtures had to be constructed. There was a total for four fixtures used; two were used for the actual heat treatments, one was used for taking real-time temperature measurements at select points on the wire, and the one more was used to record deformation and recovery angle measurements of treated SMA wires.

The first two fixtures were used to hold a SMA wire while a heat treatment was performed. This basic difference between the two fixtures is: one allowed the wire to be exposed to ambient air, and the other surrounded the wire with an inert gas, Helium, during the heat treatments. Figure 40 and Figure 41, below, show each fixture respectively.

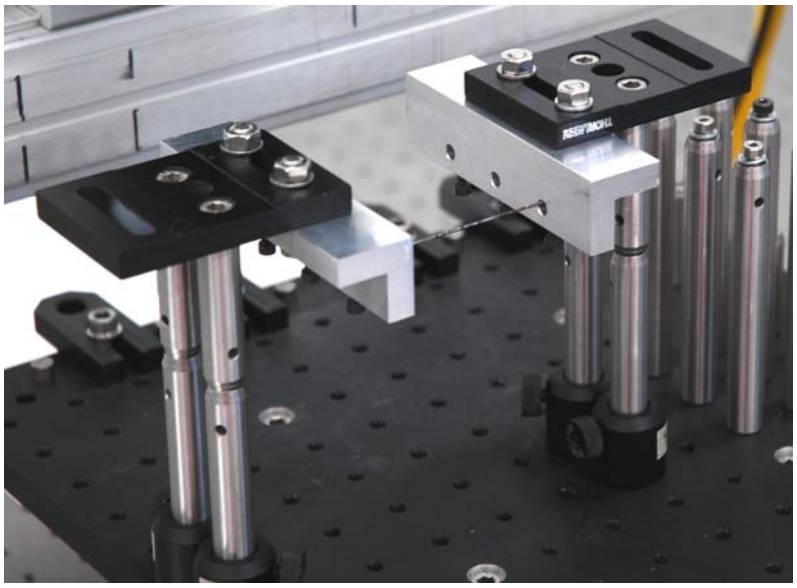

Figure 40. Simple fixture that exposes wire to ambient air during heat treatment.

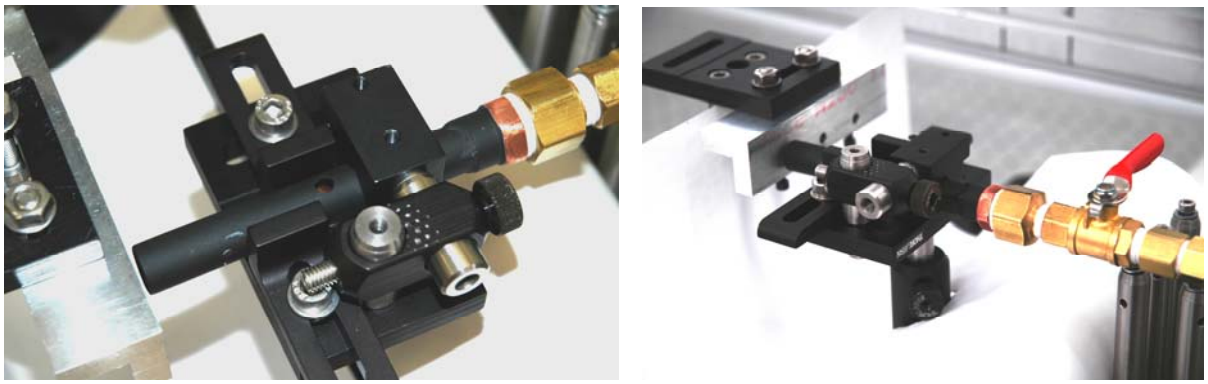

Figure 41. More complex fixture that encapsulates wire in an inert gas field during heat treatment.

The fixture in Figure 40 was the first fixture constructed to hold the wires during the heat treatments. It has two opposing wire holding blocks, which hold up to three wires, and rest atop optical post which are secured to the breadboard. Depending on the focal length of the lens and the experimental setup, different optical post can be fitted to the fixture so that the proper height of the wire can be achieved with some adjustment to the linear vertical stage.

The fixture in Figure 41 is a little more complex than that in Figure 40. After some initial experimentation and journal article research, it was discovered that during the heat treatment of a SMA wire, the Ti can begin to react with the ambient air and form oxides on the wire that not only degrade the finish of the wire, but also its transformation properties due to the high sensitivity to the Ti-Ni balance in the wire. Therefore, during most heat treatments a SMA wire must be treated in some vacuum or inert gas environment. (Melton, 1990) The device built in Figure 42 passes a very low flow rate of Helium gas axially down the wire, and the initial flow of the Helium evacuates the chamber of air. The actual chamber itself shown in Figure 42 is termed as a: variable flow inert gas heat treatment chamber, or VFIGHTC for short. The complete fixture as shown in Figure 41, works by using two independently standing halves, which are placed in very close proximity to each other. The left side of the fixture is exactly the same as that in Figure 40, and the wire is now held at one end tightly like a cantilever beam. The right side is essentially an adjustable vise for the VFIGHTC, which allows it to be slid around the wire and very close to the holding block. The through-hole in the cylindrical chamber is to allow a laser beam up to 5mm in diameter to pass through to the wire. The valve on the VFIGHTC regulates the flow rate of the

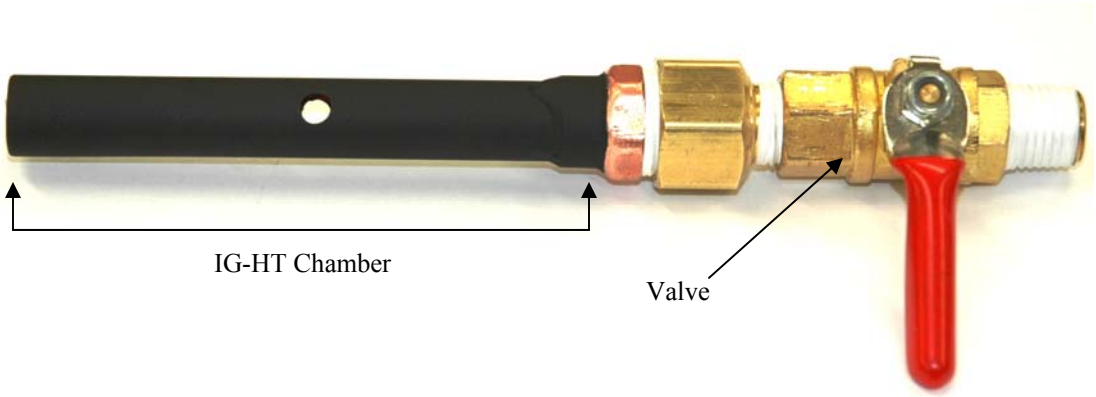

Figure 42. **V**ariable **F**low **I**nert **G**as **H**eat **T**reatment **C**hamber.

Helium, and the flow rate is kept as low as possible to not induce any significant forced convection heat transfer. The heat transfer model for the wire does not account for any forced convections, so great care must be exercised in keeping the flow rate as low as possible. Although, as in some high temperature annealing heat treatments, a quench is desired at the end of the treatment to essentially "freeze" the microstructure in some super-saturated form. An operator could be standing by at the end of the heat treatment and fully open the gas valve to produce an inert gas, convection type of quenching. This method is a viable solution because it is hard to get water to the heat treated region, thin wires can cool very fast naturally, and the wire would never be exposed to air during the quenching process.

The next fixture was designed solely to aid in the validation of the heat transfer model. A 300mm x 300mm breadboard, like that in Figure 43, rest on top of four optical posts that are attached at the corners to the bottom beardboard that is fixed to the motors. This raises the workpiece so that the desired spot size of the laser can be achieved on the surface of the wire. Secured to the breadboard are two wire holding blocks, see Figure 44, that can hold three pieces of wire 25mm apart from one another. The wire can be up to 280mm long or as short as 15mm. The only constraint on wire length is the distance between tapped holes on the bread board. The wires are secured in the fixtures with set screws that can lock the wires down from the top of the fixture.

Figure 43. 300mm by 300mm anodized aluminum breadboard by Thor Labs.

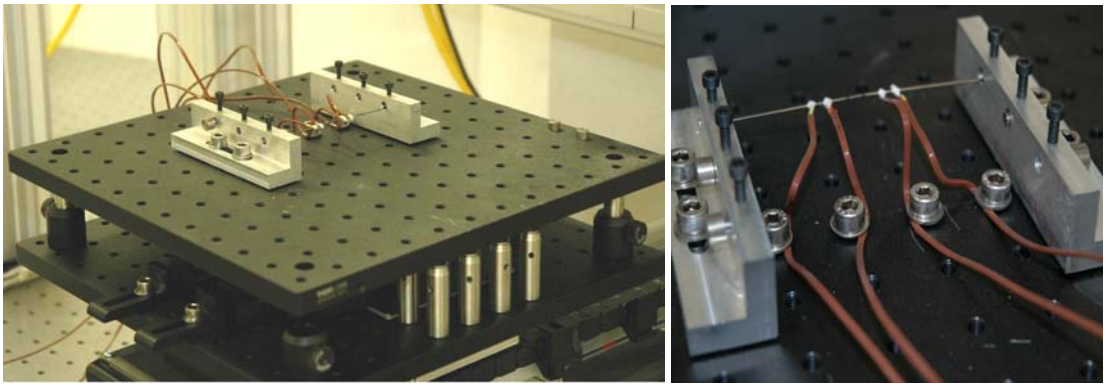

Figure 44. Workpiece setup on the aluminum breadboard.

In Figure 44, the thermocouples are attached to the wire with high temperature cement. It is important to note that the thermocouple wires are secured to the breadboard, as seen in Figure 44, with screws. This prevents the thermocouple from breaking away from the SMA wire when connecting the other end of the thermocouples into the amplifier. The interface between the thermocouple and wire is very important and quite fragile due to the porcelain like nature of the cured cement. The thermocouples are cemented to the bottom of the wire, and there should be a thin layer of cement between the wire and the thermocouple to add electric insulation. The amount of cement used should be minimal due to the added mass of the cement and its naturally high conductivity will remove energy from the wire. With this fixture, accurate temperature measurements can be recorded with certain repeatability, and without fear of damaging the fragile thermocouple interface during adjustments. This fixture is a necessity if accurate measurements are to be made in determining the validity of the heat transfer model of the SMA subject to a variety of heat treatments.

The last fixture utilized in this research measured deformation and recovery for a standard bending test, see Figure 45 below. After a particular heat treatment, the SMA wire is subjected to a test in which deformation is induced, and then some of the deformation is recovered. The fixture itself is quite simple; it has a wire clamp, and a separate angle measuring block. The clamp obviously keeps the wire in place during the test, while the measuring block is used to record the angle of deformation and the amount of recovery. The measuring block can be screwed down for repeatability in the angular measurements, or removed if a particular heat source needs to be applied for recovery. The test and use of the fixture are discussed further in Section 6.5.2.

Each fixture has a specific functionality in this research, and each fixture is designed to secure a wire during heat treatment without inducing any stress or stain while the treatment is being performed. Some of the fixtures even have special functions such as applying a shielding gas or securing thermocouples. These fixtures allow for proper heat treatments and accurate measurement.

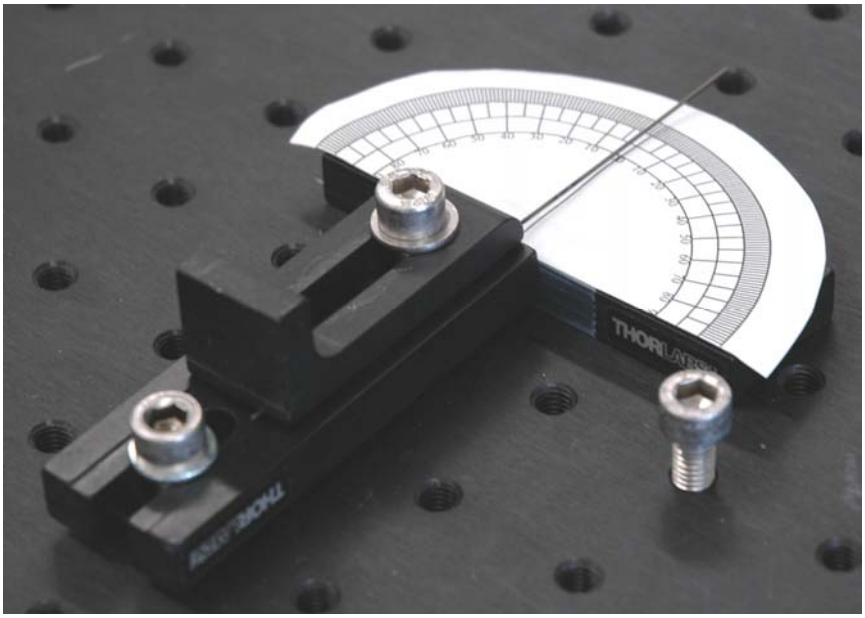

Figure 45. Deformation and recovery fixture.

6.4.3 Temperature Measurement and Sensor Calibration

Measuring the temperature of the wire is a very important task in this research. It helps determine how much energy is input into the wire and how the energy is conducted through the wire. Again, convection plays a major role in removing heat from the wire, and knowing the temperatures at specific points can reveal how much of the energy is actually convected away. This is important in the localization of the heat treatment. The more heat that is convected, the less there is to conduct, and the smaller and less severe the heat affected zone will be. Also if there is a prescribed heating or cooling rate this can be monitored and a feedback loop can even be established to increase or decrease laser power accordingly. Another important reason to measure temperature accurately has to do with validation of the heat transfer model. By running simple experiments and recording temperatures accurately at different points along the wire, a simulated model of the experiment can be adjusted to better match the results. Once this model is established many different "virtual" experiments can be simulated to determine a perfect heat treatment process. These "virtual" experiments save time, money, and allow for more efficient heat treatment process to be created. But before all of this can be done an accurate and reliable method of temperature measurement must be established.

There are two popular methods for recording temperatures in engineering applications and research. The first, and generally the best, is to use a thermal imaging camera. These cameras work by recording inferred wavelengths which are interrupted as temperature and recorded on a computer. This method is proven, accurate, and can account for the temperature of the whole wire in real-time. These cameras are also very expensive, and the funding is not available in this research to afford such a camera. Another method for recording temperature, and quite possibly the most popular, is to use a thermocouple. High temperature thermocouples can provide very accurate readings depending on the quality of the amplifier used to amplify the small voltages, on the order of millivolts, that thermocouples inherently produce. A thermocouple works by conducting a small voltage due to the contact of dissimilar metals in the presence of a temperature difference. Generally, one end of the thermocouple is placed in ice water to provide a reference, and the other end is attached to the body that is being sensed. All modern amplifiers have an electronic reference, therefore in modern setups there is only one contact, which is on the sensed body.

In this research thermocouples are used to measure the temperature of the wire. The type of thermocouple used is a K-type thermocouple from Omega Engineering Inc. The specific model number is FF-K-24-SLE. These are bonded to a wire by a high temperature, thermally conductive, and electrically insulating cement, also from Omega Engineering Inc. The specific product is Omega CC High Temperature Cement. These thermocouples are connected to a custom low noise thermocouple amplifier purchased from Lawson Labs to amplify the signal of the thermocouples. The output from the amplifier is connected to a D-Space DS1104 real-time data acquisition system, and this is the instrument that actually records the “temperature”, which is actually just a voltage from the amplifier. D-Space has the ability to sample up to eight signals at 20 kHz. The amplifier has a gain of 160 so that the thermocouple voltage is amplified enough for the data acquisition system to record, but there is not quite a linear relationship between the output voltage and corresponding temperature. Therefore a Simulink model is used to convert the voltage to temperature in the D-Space software, and the conversion is based on the curve below in Figure 46.

The amplifier has six channels that it can amplify simultaneously. Before experimental measurements are taken the thermocouple temperature conversion model and the amplifier must be validated. All six channels must produce similar values and the

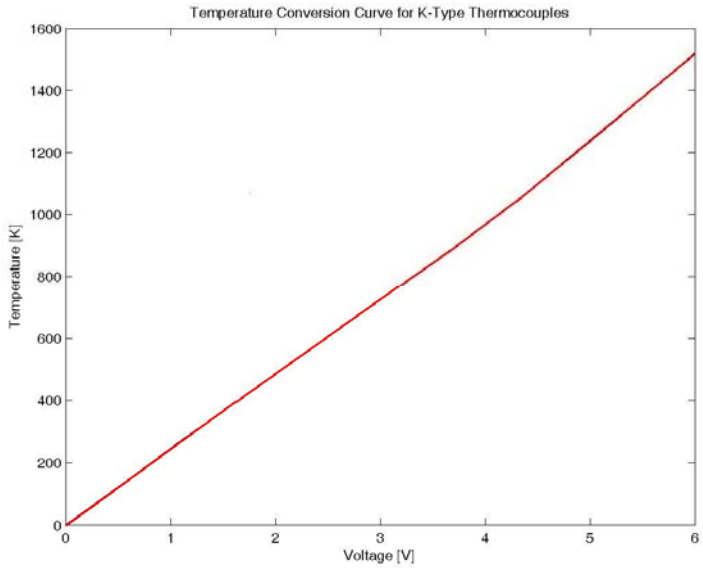

Figure 46. Temperature conversion curve used by Simulink to be record temperatures with D-Space.

temperature values will be compared to a thermocouple measurement by a Fluke meter for accuracy. A copper tube, 152mm long with an OD of 17.75mm and an ID of 17.00mm, has the Omega K-Type (Part #: FF-K-24-SLE) thermocouple cemented with the Omega High Temperature CC binder on one end. Very close to the Omega thermocouple is the Fluke K-Type thermocouple cemented with the same Omega cement. Note, the surface of the copper tube was prepared by sanding with 1500 grit sandpaper and cleaned with alcohol. The Fluke thermocouple is plugged into a Fluke 87V True RMS Multimeter, and the Omega thermocouple is plugged into the custom made Lawson Lab low-noise thermocouple amplifier. The Lawson amplifier is the connected to a D-Space data acquisition system for real-time data acquisition. The copper tube is held in a vise and is heated with a Bernzomatic propane torch. The experimental setup is shown below in Figure 47. After cycling all the channels from room temperature up to temperatures between 600K and 700K, and then recording the temperatures upon cooling every ten seconds on the Fluke and D-Space, the error between to two was examined and was determined to be no higher than 3% on any measurement. After this experiment, the temperature measuring system is assumed to be valid and ready for experiments involving the heat treatment of SMAs.

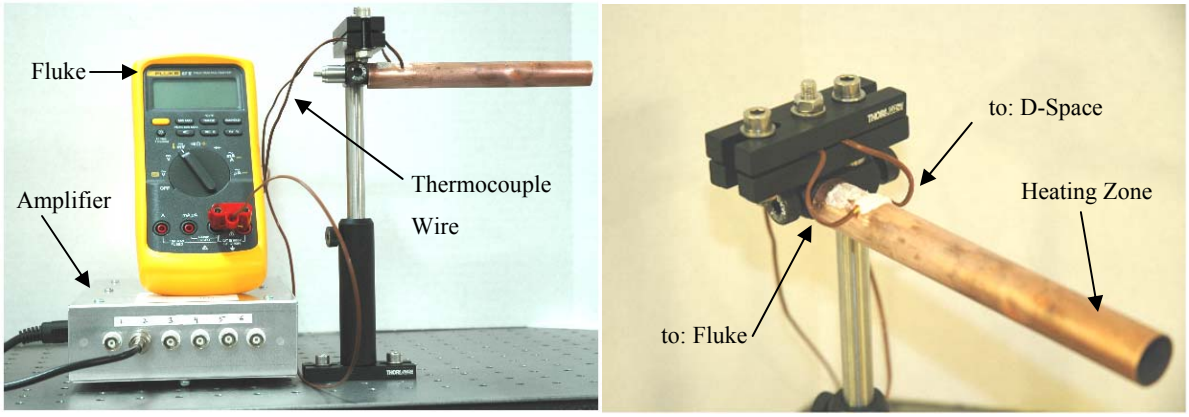

Figure 47. Experimental setup used to validate the thermocouples.

6.4.4 Laser Alignment

The alignment of the laser beam is crucial to creating accurate and precise heat treatments. There are four important aspects of laser alignment in this particular setup. First and foremost, all the work surfaces, stages, and instrument holders must be flat and level. The optical table should be level, but since everything is relative the optical table, everything must be level relative to the optical table work-surface. All surfaces should have no more than a flatness tolerance of 0.005 inches or less. The second aspect is the angle of the collimator with respect to the work-surface, and the laser beam needs to be delivered perpendicular to the work-surface. The third aspect is the tilt of the beam expander. This will again affect the perpendicularity of the beam with respect to the work-surface. Also if the tilt is too great the collimated beam may strike the inside of the beam expander thus absorbing part of the energy, thus the desired amount of energy will not reach the workpiece. The last aspect is the tilt of the lens holder. This can affect the angle at which the beam strikes the workpiece as well as the focal point of the laser beam, thus changing the energy density and spot size of the beam.

The first aspect of alignment is controlled by simply purchasing parts that meet the flatness tolerance of 0.005 inches or less, and taking care to mate parts perpendicular or parallel when assembling. All the components in the laser setup meet this criterion. Therefore, all mating surfaces should be secured tightly to one another so that there is no room for movement between the surfaces, and there are no gaps that would cause the surfaces to not mate properly. Also, when mating one part to another, the mating part should

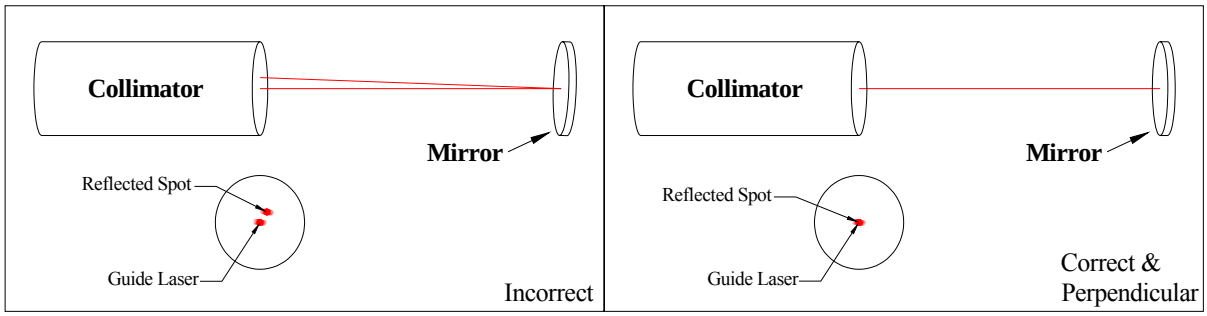

Figure 48. Reflected spot on collimator lens versus perpendicular alignment.

be centered on other part to ensure that all edges are parallel and perpendicular. This should be done with a set of calipers and a square.

A custom sleeve was designed to hold the collimator in a perpendicular fashion with respect to the work-surface. This cuff was designed to clamp around the outside of the collimator and attach to the aluminum structure as shown in Figure 39. A guide beam of visible wavelength is produced by the laser, and this is shined onto a reflective mirror resting on the optical table surface below. The beam is reflected back to collimator. If there is a reflected spot slightly off center of the collimator, then the beam is not perpendicular to the work surface, see Figure 48. Therefore, the cuff that holds the collimator is shimmed with thin wedges of steel to adjust for this. Once the reflected spot is in the center of the collimator the guide beam is perpendicular to the work-surface.

Once the collimator is aligned, the beam expander and linear stage must be implemented into the setup. First, the entrance of the beam expander must be level and perpendicular to the work-surface and collimator. The beam expander is attached to the linear stages as shown in Figure 37. The mirror is then placed on top of the beam expander, and the same process used to adjust the perpendicularity of the collimator is used on the beam expander. Again, Figure 48 shows how the reflected beam should line up with the collimated beam. A small circle, the size of the diameter of the entrance of the beam expander, is printed out with a crosshair in the middle. CAD software is used to print the circle to ensure the correct size and centering of this template. Then the micro-positioners on the linear stages are adjusted so that the crosshair is in the center of the guide beam. Once the beam is center on the template the mirror can be placed under the beam expander; the guide beam should come out of the collimator, through the beam expander, reflect off the mirror, go back through the beam expander, and shine on the collimator a the point where the guide beam initially exits.

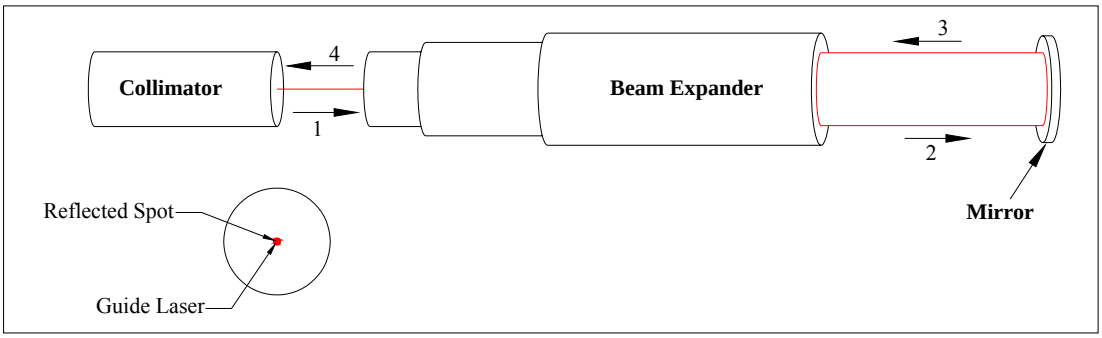

Figure 49. Perpendicular and centered beam expander and collimator.

When this is seen the beam expander is perpendicular to the work-surface and centered underneath the collimator. Figure 49 shows the path of the laser beam when these conditions are met.

The last component in aligning the laser is to align the lens. This is one of the most important parts of the laser setup. The lens focuses the beam and is the key component in increasing the power density and creating a small spot size. The lens is in a lens holder which is attached to an optical post, which fits into a post holder, and the post holder is attached to the linear stage. It is important to center this post holder with the calipers on the linear stage since the beam expander is also centered on this stage. Another paper template the size of the lens holder is printed out with a crosshair and 25mm diameter circle printed on it. The template is placed in the lens holder and the whole assembly is placed in the post holder. The post slides into the post holder, and the post holder is adjusted until the beam is centered on the template. Once the beam is centered the lens is placed in the post holder. The mirror is placed under the lens and the lens holder is tilted until the reflected spot on the collimator lines up, similar to that shown in Figure 50. The focusing setup is now aligned and the laser beam is now perpendicular to the work-surface. With the laser beam properly aligned, accurate and precise energy application can be applied, and the spot size can simply be changed by adjusting the vertical axis on the linear stage.

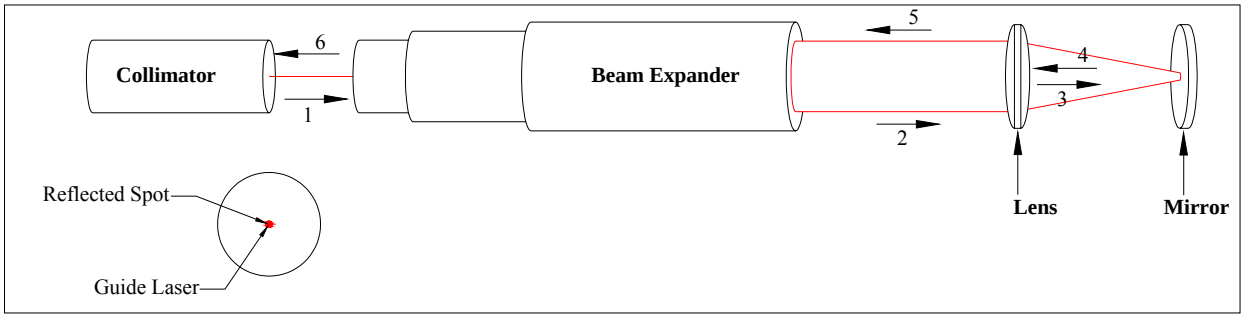

Figure 50. Final alignment of laser beam with focusing lens.

6.5 Validations

6.5.1 Laser Treatment Validation

The laser treatment model must be validated to demonstrate that the assumptions inherent in the model are correct. For this particular model, the prediction of the temperature distribution in the model needs to be verified. One method of validation is to take temperature measurements at various points along the wire, using thermocouples, and compare those measurements against the predicted temperature distribution in the wire. More specifically, different heat treatments can be performed on different sizes of wires, and the model will predict the temperature at each point in time. These predicted points will then be compared against real-time data collected from the thermocouple measurements. The heat treatments vary in degree from a simple heat-up, hold temperature, and air cool treatment, to a complex pulsing treatment with multiple stages and controlled cooling rates. This will help determine the applicability of the model, and should help to draw correlations for some experimentally determined constants, such as absorption and convection coefficient.

6.5.2 SMA Mechanical Property Change Validation

The goal of this research is to produce localized changes in the mechanical properties of SMA wires. Once heat treatments have been applied to specimens of SMA wire, the changes to the mechanical properties must be quantified in some manner. Since the goal of heat treating a superelastic wire is to induce a localized area that will exhibit the SME, and a simple bending deformation and recovery test is used to compare and contrast the different heat treatments. Examining different types and lengths of heat treatments using this method

and the deformation-recovery fixture allows one to see just how well one heat treatment changes the recovery, or SME, properties of the wire versus other heat treatments. Being able to analyze this information leads to more effective heat treatments which can produce a SME with more recovery and smaller heat affected zones.

The recorded deformation and recovery measurements are used to determine a ratio of recovery to deformation angle. This will help realize SME affects that may not show large amounts of deformation, but still recover a large percentage of what was deformed. Also from the measurements taken above, trends can be noticed in the deformation and recovery as a function of heat treatment time and temperature. All heat treatments have a limit at which the properties are best manipulated. Once that time or temperature is exceeded, properties will begin to decrease. This initial decrease should be a sign of the maximal properties for that particular set of parameters in the heat treatment. For aging, if the soak time is too long the precipitates will resist the SME and essentially strengthen the SE state again. Noting clues like these will help to identify the maximum change in properties that the SMA will obtain while subject to a particular heat treatment.

Determining essentially how localized an effect is in an SMA can be complicated. There are certain visual changes in the wire's surface due to the heat treatment, such as bright, shiny surface. While this gives a general idea of how localized the effects are, a better method is to look at the temperature distribution predicted by the model. Being able to look at the local temperature profile in time will allow one to know just how long a certain region of a wire stayed above some temperature, but an understanding of how an SMA will behave at an elevated temperature is required.

7 EXPERIMENTAL INVESTIGATION

7.1 Variable Flow Inert Gas Heat Treatment Chamber

7.1.1 Oxide Reduction Setup

The VFIGHTC was designed to alleviate the possible formation of oxides during heat treatments due to the reactivity of Ti at elevated temperatures. The physical attributes of the device are discussed in Section 6.4.2 and a picture is shown above in Figure 42. The

effectiveness of the device is evaluated by performing one simple experiment. A basic heat treatment, which is known to form oxide on a wire in open air, is performed two times. The treatment is performed the first time while the wire is in open air, and the second treatment occurs while the wire is in the VFIGHTC. A thermocouple is attached equal distances from the two different treatments and real-time temperature data is collected during each experiment. After the heat treatment is performed, the first check is a visual inspection of the wire for oxides. This evaluates how well the VFIGHTC protects the wire from the formation of oxides. The goal is to obviously find no oxides on the wire that was in the VFIGHTC. The second check is to calculate the difference in the temperature readings from the thermocouple measurements. A large difference in the temperatures for each treatment would suggest that the Helium flow rate is too high, thus causing a cooling, forced convection. As previously mentioned, the model is not designed to account for a forced convection situation. Therefore, the wire must be free of oxide when treated in the VFIGHTC, and the temperature measurements for each experiment must be relatively close to one another, hence confirming negligible forced convection, for the VFIGHTC to be applicable in this setup.

7.1.2 Oxide Reduction Results

Figure 51 shows two sections of wire subject to the same heat treatment. The section on the left was done in open air (OA), while the one of the right is performed in the VFIGHTC. The section of the wire that was done in open air has a tarnished section around the heat treatment, and a noticeable white crusty oxide in the middle. This oxide makes this section of wire very brittle and it tends to break easily. This oxide is thought to be TiO_2.

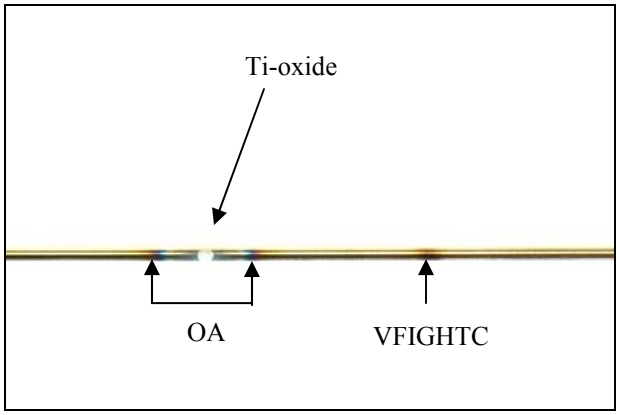

Figure 51. Comparison of a wire treated in air and in the VFIGHTC, respectively.

During the heat treatment, the wire heats up so hot, that when the naturally convecting air passes around the wire the highly reactive Ti phase pulls the oxygen out of the air. This creates the aforementioned oxide, which decimates the properties of the wire in that area. Now comparing the left side to the right side, it is easy to see that no oxides have formed on the right. There is only a small tarnished spot where the wire became very hot and cooled down. The Helium that surrounded the wire in the VFIGHTC, is inert, thus it does not react with the Ti during the heat treatment, which allows the treatment to obtain optimal properties. Now that the VFIGHTC has proven to eliminate the formation of oxides in heat treatments, the natural characteristics of the wire are preserved so that the heat treatment can fully achieve the desired properties; as a result this fixture has become an integral part in this setup.

7.2 Laser Treatment Model

7.2.1 Model Validation Setup

For the laser treatment model validation, three different diameters of wire: 1.04mm, 0.76mm, and 0.61mm, are heat treated separately using a simple heat treatment as shown in Figure 53a, and with a more advanced heat treatment in Figure 53b. A wire block is secured to the breadboard that rest on top of the lab setup, as presented above. The wire block holds a 55.8% Ti-Ni wire that is straight annealed to be superelastic. Four thermocouples are cemented to each wire at various locations to record real-time data, as shown below.

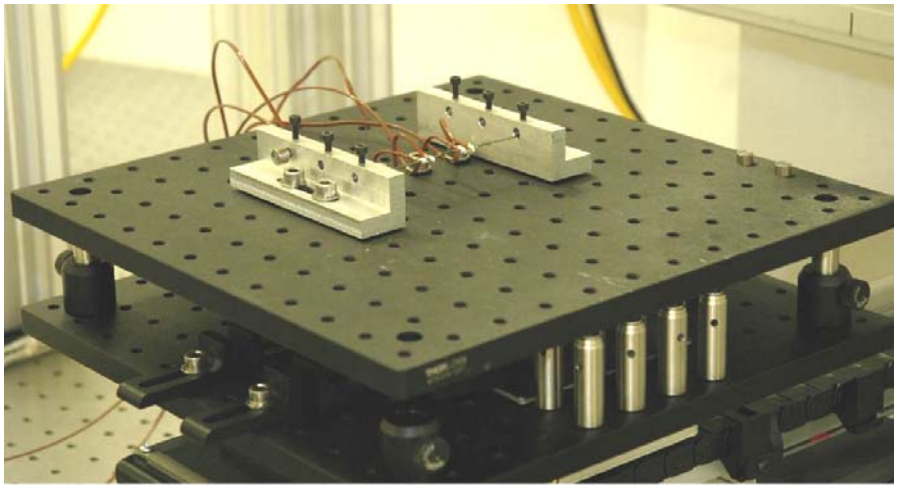

Figure 52. Temperature distribution prediction model validation wire setup.

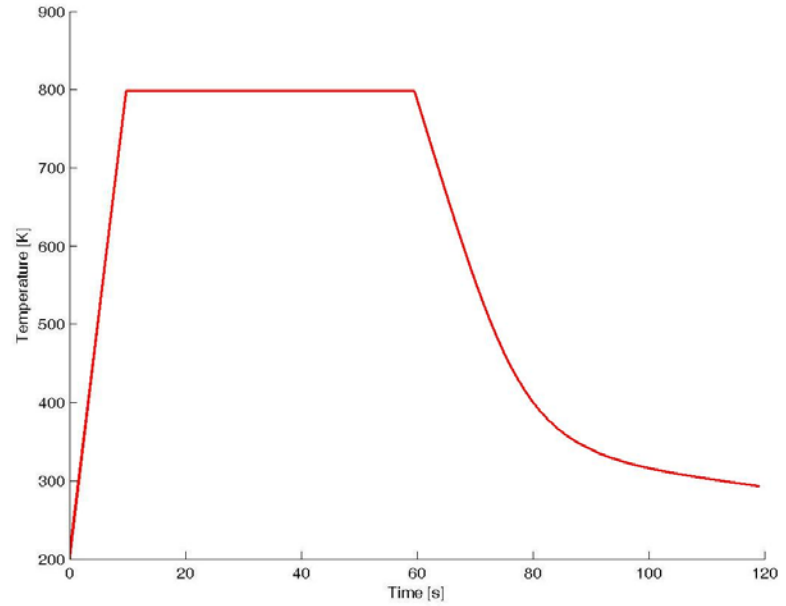

a

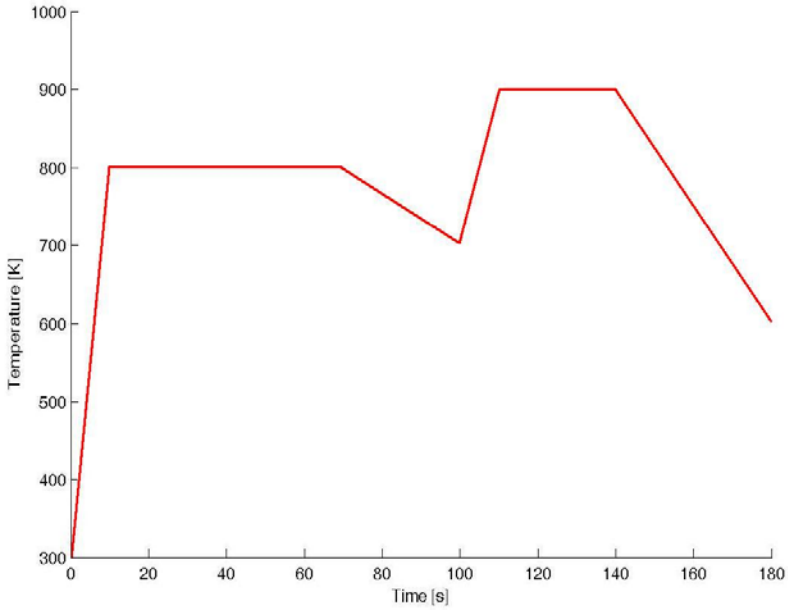

b

Figure 53. Simple (a) and advanced (b) heat treatment profiles.

7.2.2 Model Validation Results

The temperature distribution model proved to predict the temperature distribution of all three heat treated wires. The results for the simple heat treatments are shown below.

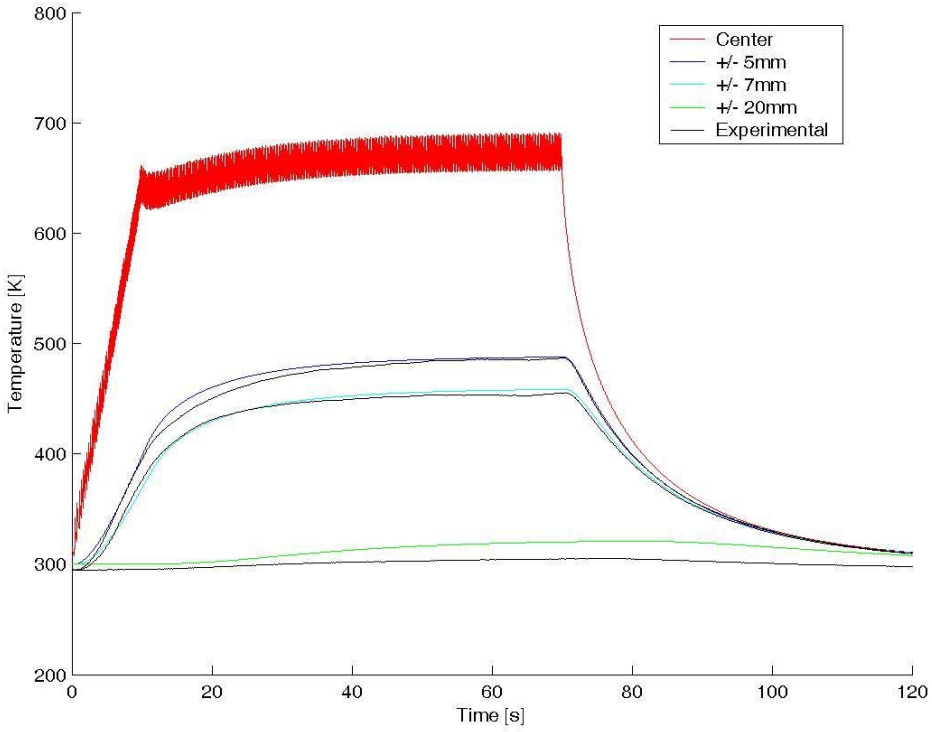

Figure 54. Simple heat treatment of 0.61mm diameter wire.

In Figure 54, above, the red plot represents the temperature history for the center element of the wire. This is where the laser beam is shining on the wire, as a result, this is the point of highest temperature in the wire. Notice how the temperature fluctuates between the defined tolerances, and how after 40 seconds a constant temperature range is established. This plot is purely predicted since a thermocouple placed under the laser beam would be melted. Therefore, the other three predictions in the plot above are used to verify that the model can correctly predict the temperature at specific points on the wire. The blue, cyan, and green wires represent points that are 5, 7, and 20 millimeters away from the point of laser application, respectively. These plots are the laser treatment model's prediction of the temperature history for that point on the wire. The black lines that closely follow each of the predicted temperature histories represent the real-time data collected during the actual heat treatment. The thermocouples closer to the center of the wire have a very tight fit between actual and predicted temperature histories. This close fit represents the model being a sound predictor of temperature histories in this particular wire. The thermocouple furthest from the

wire does not exhibit as good of a fit as the others do. This may represent that the model has a difficulty predicting temperatures closer to the ambient temperature. The convection coefficient is the likely culprit here. This is deduced from the fact that the model predicts the temperature during the heating phase, but once convection begins to play a major role in the prediction, the model starts of over estimate the temperature at that point. Since the temperatures are close to ambient, there is not a large temperature difference between the wire and the ambient air. This means that the natural convection will be quite low. Since there are numerous approximations going into the calculation of convection coefficient, the small temperature difference is causing even more problems. The model has predicted the convection coefficient to be too low this far away from the wire, resulting in the over prediction of temperature at that point. While this is the possible cause of the over estimation of temperature, the fact that this is occurring at a temperature below 400K and that the element is so far away for the center of laser application the error is negligible. Since the temperature is under 400K, no changes are being made to the SMA microstructure. Also, the model is over predicting the temperature, so the model can be thought of as a worse case scenario, which is much better than an under prediction of temperature. Combined with the fact that this artifact is occurring 20mm away from the center of the laser application, the error is even more insignificant. Therefore, it can be said that this model made an accurate prediction of the temperature distribution in this wire. But, for this model to be robust, it must continue to achieve this kind of prediction for other sizes of wire. Examine the results of the model in Figure 55.

In Figure 55, much of the same results are seen as that in Figure 54. In this particular heat treatment, the soaking stage is held quite constant early in the treatment. This is reflected in the temperature history of the thermocouple that is 5mm away from the center of laser application, the blue plot. Again, the black lines, the real-time data, is closely predicted by the model. Also, as mentioned in the pervious figure, the 20mm thermocouple show a over prediction of temperature after the heating phase, thus reiterating the under prediction of the convection coefficient. But again, it is under 400K, and is negligible with regards to the heat treatment. There is no 7mm thermocouple, because it was actually a mistake in the pervious experiment. There is really two 5mm thermocouples, and only one of the real-time

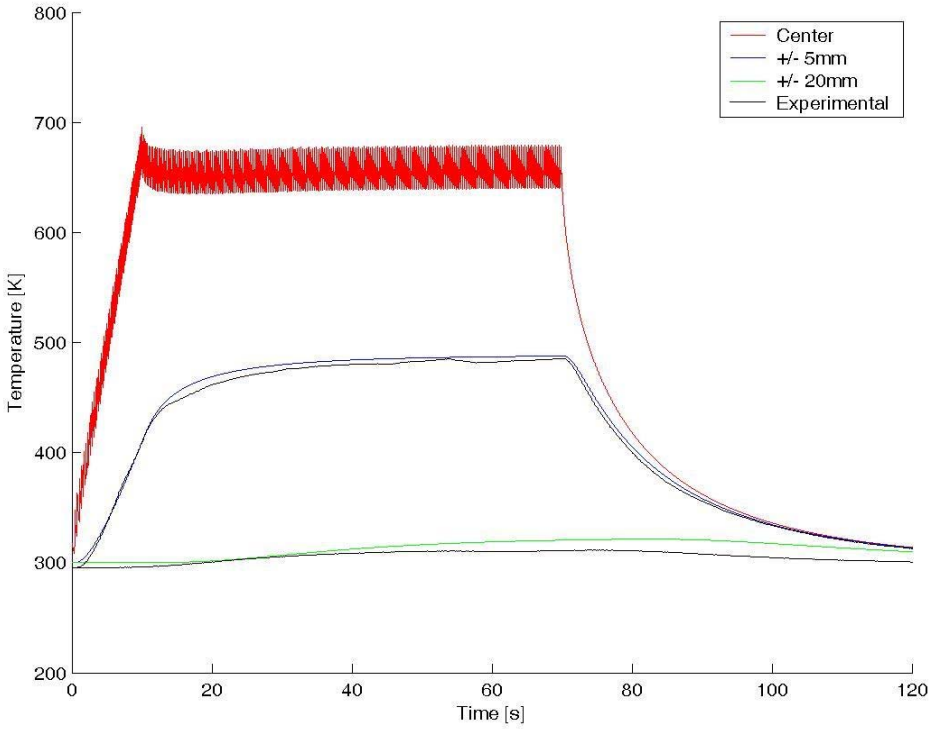

Figure 55. Simple heat treatment of 0.76mm diameter wire.

data arrays is plotted here because they are so close to one another, it caused confusion on the original plot. This is a good sign though; the energy from the heat treatment should propagate the same in direction down the length of the wire, and this is verified by similarity in the two real-time data measurements at 5mm for this wire. It is important to note that the absorption factor used in the model for this wire was different than that of the previous model. This issue will be addressed in detail below. Even with this small change in the model, a good prediction was achieved; therefore another size of wire should be examined.

Just like Figure 55, Figure 56 shows very similar results as that of Figure 54. There is a good prediction at 5mm, the 20mm prediction is over estimated due to the convection coefficient, and the absorption was again adjusted to create this model. After examining these three experiments it can be said that the model makes valid predictions of the temperature distributions in the SMA wires. The only problem is that the absorption of the laser beam tends to change depending on the diameter of the wire. Below, this problem will be addressed in detail.

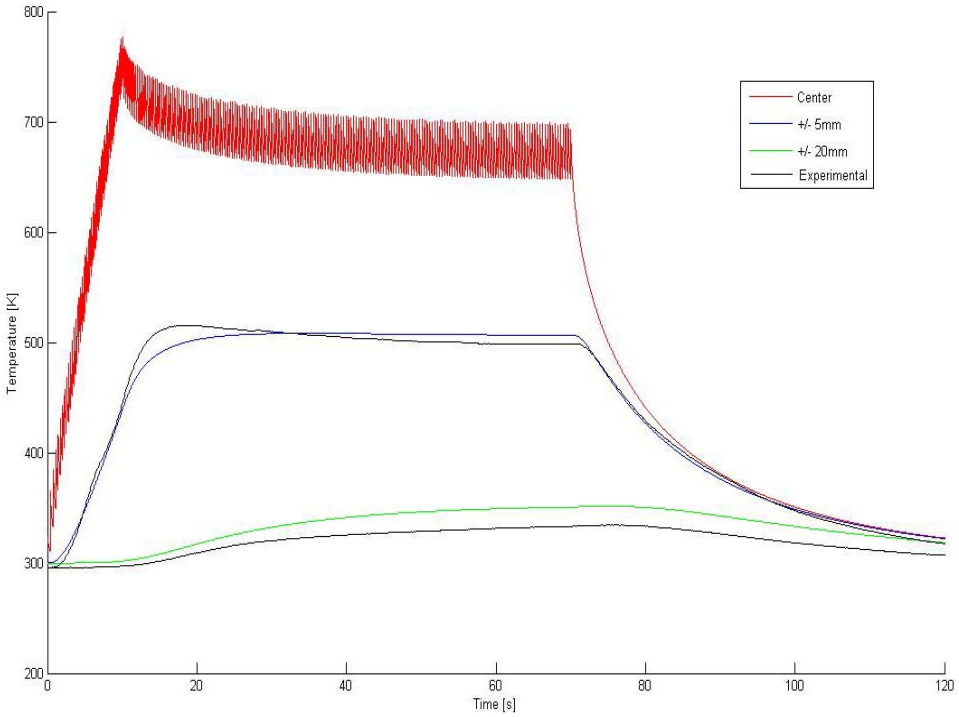

Figure 56. Simple heat treatment of 1.02mm diameter wire.

It can easily be seen that all the predicted temperatures follow the actual measurements. While these heat treatments look elementary, they all have the three basic components that make up any complex heat treatment: a controlled heating rate cycle, a soaking temperature cycle, and an uncontrolled cooling cycle. The cooling rate can just as easily be controlled as the heating rate, but the fact that this model predicts the cooling due purely to natural convection represents a correct convection coefficient. Since each wire's basic model can be predicted, the complex models are also predicted closely. Figure 57 shows a heat treatment performed on the 1.04mm wire.

In the complex heat treatment above, Figure 57, there are multiple points along the wire in which real-time data was collected. Again, the red plot represents the center of laser application, and the temperature history of that element. The blue, green, and cyan histories are the predictions of temperatures 5mm, 10mm, and 15mm from the center of application, respectively. Even with this complex heat treatment that has multiple heating, soaking, and cooling stages, the model does an outstanding job of creating the temperature histories of

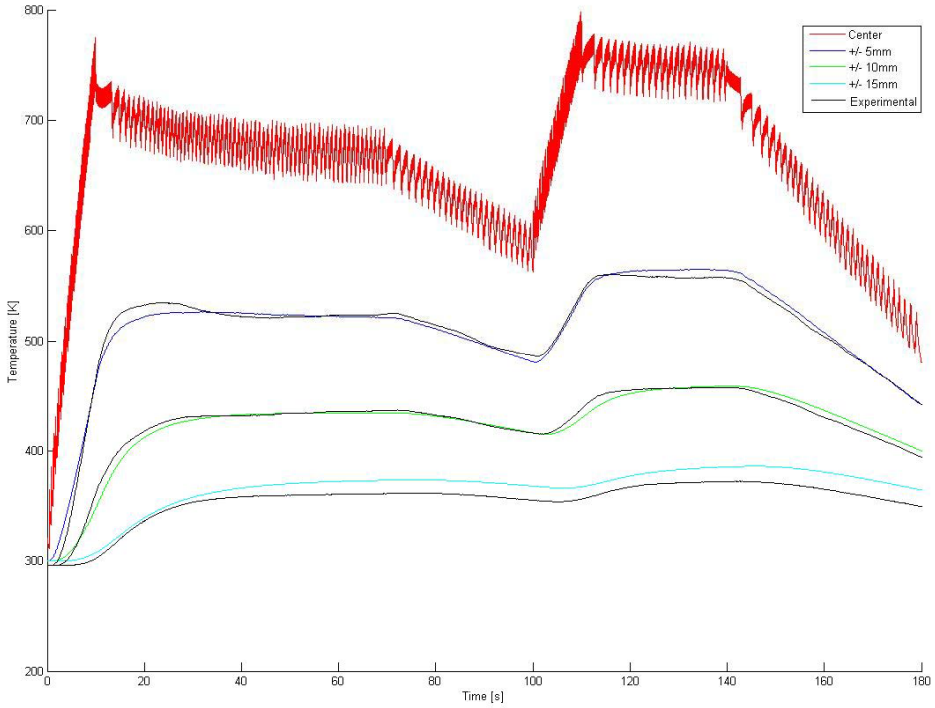

Figure 57. Complex heat treatment prediction and actual temperature distributions for a 1.04mm diameter wire.

three points on the wire. But, just like the simple heat treatments, the furthest thermocouple is under 400K, and begins to slightly over predict the temperature after the first initial heating stage. The error is not as severe as that at 20mm, but it is still evident in this heat treatment. But again, it is important to reiterate, that the temperature does not exceed 400K, therefore no changes in the SMA microstructure are occurring here anyway, thus this error is negligible. The two smaller diameters of wire were subjected similar heat treatments and produced similar results. These are not presented here, since the laser treatment model should now be quite a trustworthy tool for creating temperature distributions in SMA wires.

While much praise has been given to the model for its ability to precisely predict the temperature distribution in SMA wires, there are two glaring inconsistencies in the model. The absorption, which is the percentage of the laser beam absorbed, and the convection coefficient constant, “a1,” were adjusted for each wire size. These two constants stayed the same for the different heat treatments performed on a wire, but they were adjusted for each wire. It is necessary to determine why this is so, to truly validate the model. Initially, since

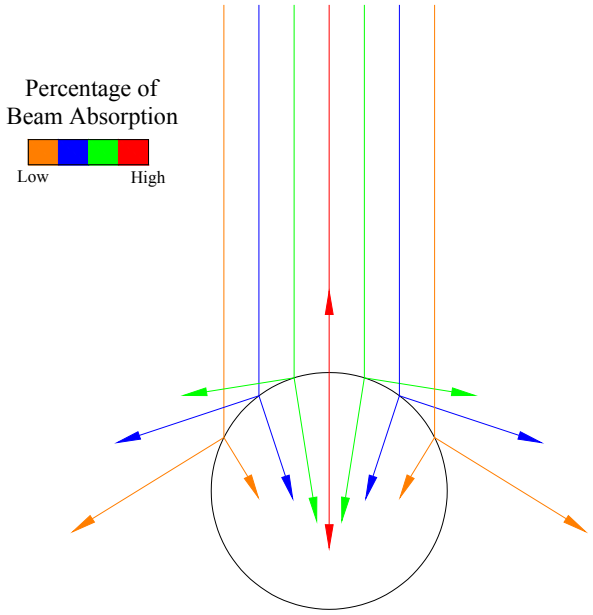

Figure 58. Effect on absorption for a laser beam incident on a round wire.

the constants only have to be adjusted when wire size is changed, this suggests that they are functions of the diameter of the wire. For the absorption of the laser beam it is important to consider that the laser beam is being shined on a round surface. Figure 58, above, illustrates how this can affect absorption. In Figure 58 the different colors represent the different angles at which a photon will strike the round wire. The cross-section of a wire is represented by the circle in the schematic above. Notice how the red photon will strike the surface perpendicularly and become mostly absorbed, where as the orange photon strikes the side, and only a fraction of the energy is absorbed. As shown in the legend in Figure 58, the different colors represent different absorption levels, and the length of the reflected and absorbed vectors depicts the relative magnitude of each. As one can see, different parts of the beam absorb different amounts of energy, the idea is to find the total amount of energy that the wire absorbs. Since the only changing characteristics of the heat treatment are the wire diameter and beam diameter, the experimentally determine values for absorption might be a function of beam coverage area. Table 1 has each wire size, beam diameter, coverage area, and the corresponding value for the absorption. If the beam coverage of the wire in Table 1 is divided into the corresponding value for absorption and plotted, Figure 59 is produced.

Table 1. Experimentally determined values for absorption

Beam Diameter	Wire Diameter	Coverage Area	Beam Absorption
2.000	1.020	2.040	0.385
2.000	0.760	1.520	0.270
2.000	0.610	1.220	0.225
2.000	0.360	0.720	0.130

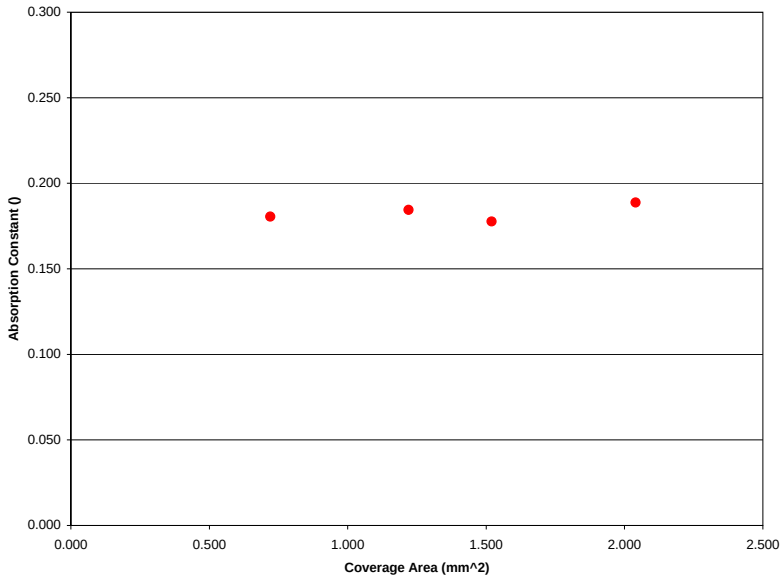

Figure 59. Absorption constants relative to the beam coverage.

The fact that all these values are relatively constant illustrates that the absorption in the heat transfer model can be approximated to some factor of beam coverage on the wire. The particular value for the absorption constant, α_c, for this model is approximately $0.183 mm^{-2}$. Thus yielding Equation 27, which calculates the amount of energy the laser is actually able to input into the wire.

(27) $$P_{in} = \alpha_c \times d_{wire} \times d_{beam} \times P_{output}$$

Where:

P_{in} = Average power input to the wire [W]

α_c = Absorption constant [$1/mm^2$]

d_{wire} = Diameter of wire [mm]

d_{beam} = Diameter of laser beam [mm]

P_{output} = Average power output from the laser [W]

Using this equation, the absorption for can be calculated based on wire and beam diameter, and no longer has to be experimentally derived.

The other ambiguity in the model is the convection coefficient constant. As stated in 6.2.2 "Convection Coefficient Model," Shu *et al.* created a model for the natural convection around a SMA wire. In this derivation Shu *et al.* introduced two constants in the equation for the Nusselt number, α1 and α2. There was no formal information given for the determination of these constants. Shu et al. described these constants as being "experimentally determined," and suggested that the Rayleigh number for very thin SMA wires is very low, therefore the constant must be determined experimentally. Therefore, α1 and α2 are determined by running a simple heat treatment like that shown in Figure 53a, and adjusting the constants until the proper fit is achieved. Since there is two constants, the best method for finding both is to set α2 to some constant number, and adjust α1until the fit is achieved. The last part of the treatment is a free convection cooling, therefore, in this region there is no energy input or other form of cooling. Since the convection coefficient pertains to only this type of cooling, this is the section of the treatment that must be matched. If the laser treatment model is simulated with α1 too high, this region of the graph will cool down too quickly, and if α1 is too low, the wire will not cool down fast enough. See the examples in Figure 60. Essentially, α1 controls the slope of the cooling curve; hence, finding this slope is the key to achieving a model with the proper convection coefficient.

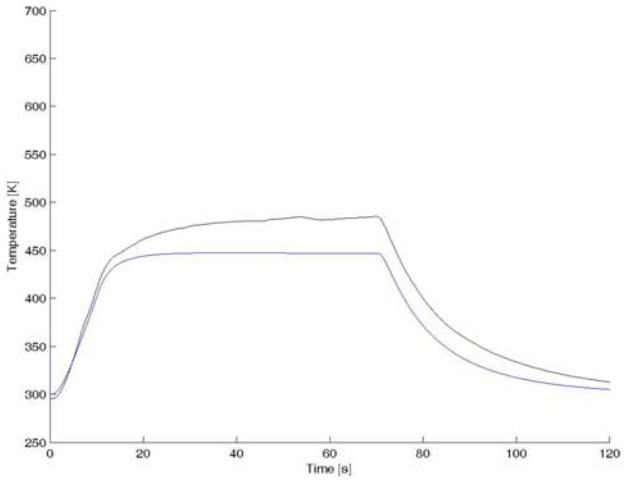

a)

Figure 60. Effect of convection coefficients: convection too high (a), convection too low (b), and the correct convection coefficient (c). (Continued on next page)

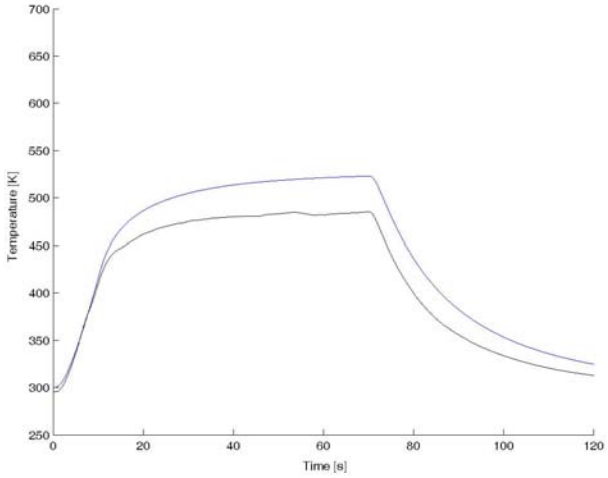

b)

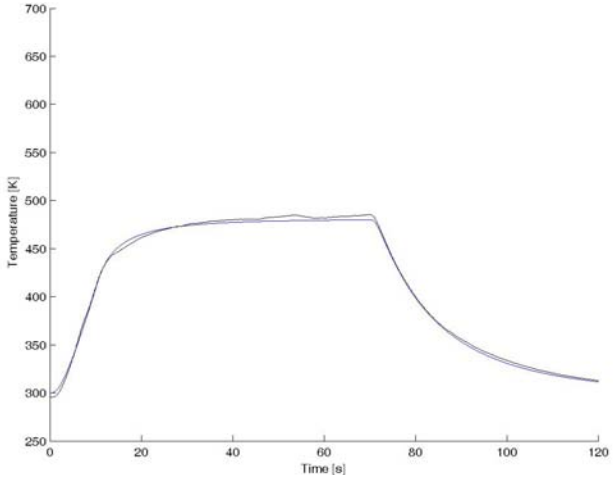

c)

Figure 60 continued. Effect of convection coefficients: convection too high (a), convection too low (b), and the correct convection coefficient (c).

Notice that in a) and b) from Figure 60 the slopes during the cooling parts of the heat treatments do exactly match that of the measured data, the black curve. In a) the slope is too steep and in b) the slope is too flat. Also, the predicted curve, the blue curve is lower in a) and higher in b) due to the incorrect amount of energy being removed. But in c), both the slope of the curve and the amount of energy removed is correct. This is when a proper convection coefficient is obtained.

Once these two issues have been resolved, the types of temperature predictions presented in this section can be achieved. With a valid temperature distribution model, virtually any prescribed laser heat treatment can be input into the model, and temperature

distribution in the wire can be predicted with confidence. Again, this is the first major step in developing localized heat treatments. Being able to know this information with this level of confidence is necessary to produce accurate heat treatments that can change the tenuous properties of a SMA alloy wire. Furthermore, the abilities of this model are necessary to produce very local heat treatments with confidence.

7.3 SMA Property Change

7.3.1 Property Change Setup

For the SMA property change validation, various heat treatments were performed on two different diameters of wire to determine the affects of an aging process on the superelastic Ti-Ni, used above. Table 2 shows the combination of heat treatments that were performed on different sizes of SMA wire. The heat treatments were performed in the VFIGHTC to protect the wire from the combination of the heat treatment and the ambient air. The heat treated wire is then placed into the bending vice, and a deformation and recovery test is performed on the wire to evaluate the effects of the heat treatment. Figure 61 shows the four step approach to the deformation and recovery test.

Table 2. Different aging heat treatments performed on the SMA wires.

Heat Treatment	Diameter [mm]	Temperature [K]	Time [s]
1	0.61	800	36
2	0.61	800	360
3	0.61	1000	36
4	0.61	1000	360
5	0.61	1200	36
6	0.61	1200	360
7	0.76	800	36
8	0.76	800	360
9	0.76	1000	36
10	0.76	1000	360
11	0.76	1200	36
12	0.76	1200	360

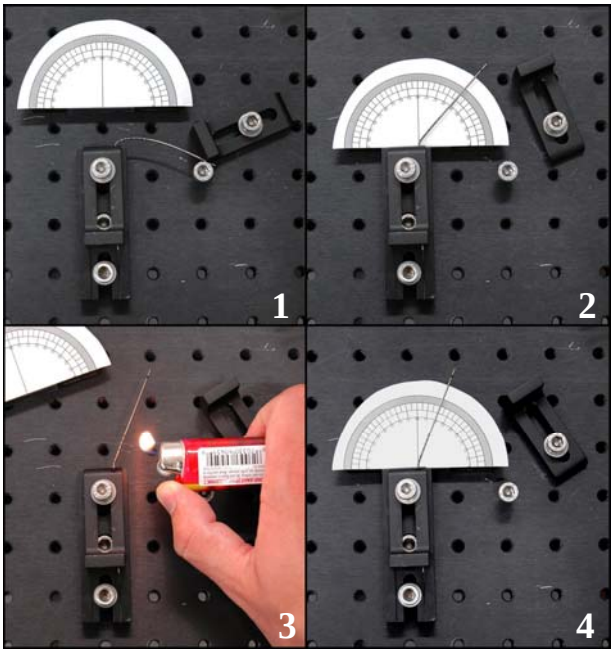

Figure 61. Deformation and recovery angle measurements.

In step 1 of Figure 61, an initially straight 80mm portion of the wire is screwed into the heat treatment block. The clamp is set so that just the edge of the heat treated section is at the base of the clamp. The wire is then bent by applying the necessary force at a point 50mm from the heat treated region to bend the wire back to the screw on the right. Step 2 shows the deformation after the force is released, and the angle being measured. In step 3, heat is applied to the specimen at the bent portion to induce any possible SME recovery. In the final step, the recovery is measured.

7.3.2 Property Change Results

Now that the temperature distribution model has been validated as an acceptable model to predict temperature distributions, heat treatments are to be generated using the model so that the localized properties of a SMA can be changed. This will determine if the new model can be used as a tool to locally heat treat shape memory alloys. The heat treatments described above were carried out and the results of the deformation and recovery test are presented in the table below. The results of the deformation and recovery test on the 0.61mm case are shown in Figure 62, below.

Table 3. Deformation and recovery test results.

Heat Treatment	Diameter [mm]	Temperature [K]	Time [s]	Deformation [degrees]	Recovery [degrees]	% Recovered
1	0.61	800	36	10	1	10.00
2	0.61	800	360	12	3	25.00
3	0.61	1000	36	17	2	11.76
4	0.61	1000	360	17	4	23.53
5	0.61	1200	36	20	1	5.00
6	0.61	1200	360	22	1	4.55
7	0.76	800	36	12	4	33.33
8	0.76	800	360	15	5	33.33
9	0.76	1000	36	32	9	28.13
10	0.76	1000	360	25	6	24.00
11	0.76	1200	36	16	4	25.00
12	0.76	1200	360	14	3	21.43

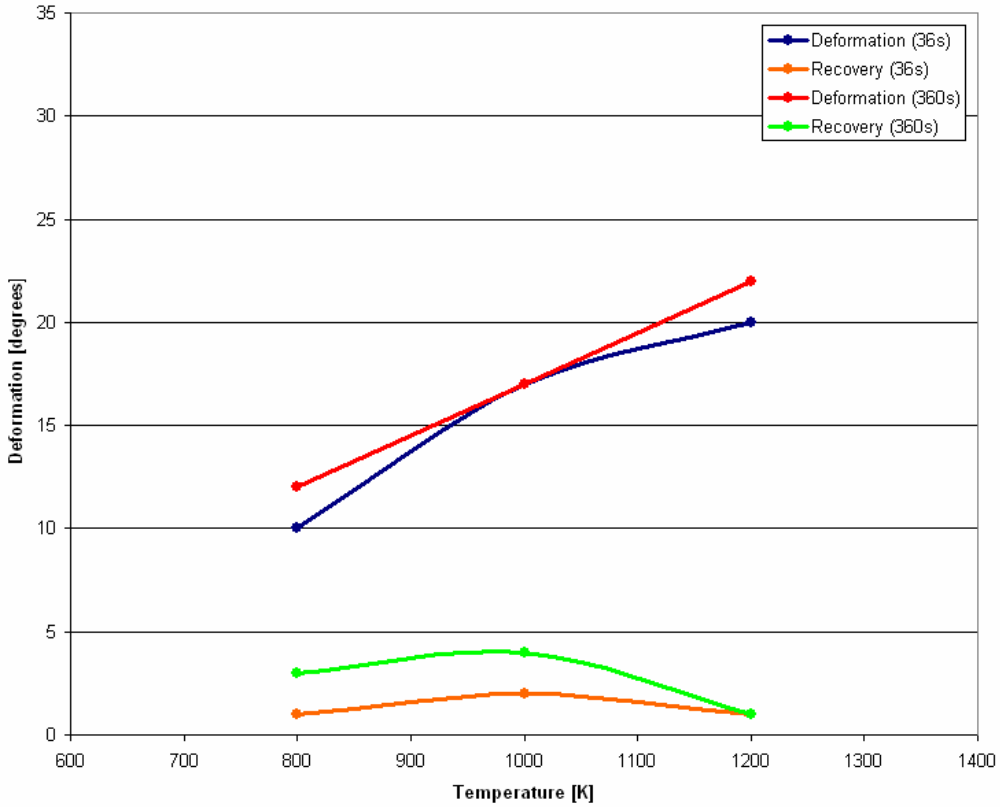

Figure 62. Results of deformation and recovery test for the 0.61mm diameter wire.

The top two plots in Figure 62 represent the deformation with respect to temperature change for the wires treated for 36 seconds, blue plot, and 360 seconds, red plot. First, notice how the deformation for each treatment increases with increasing heat treatment temperature. Since growth rates of precipitates are temperature dependent, it is sensible that more Ni-rich

precipitates will grow from the Ni-rich wire, which raises the transformation temperatures, thus causing the SMA to be more sensitive to deformation. This is an indication of the SME, and is present for both lengths of treatments. Also notice that the wire treated for 36 seconds, the blue plot, does not show as much deformation as the one treated for 360 seconds, the red plot. Since the precipitates are given longer to grow in the 360 second case, it is predictable that the wire will show more SMA properties. When the recovery for each case is examined, some of the same features are seen. For the recovery of the 360 second treated wire, the green plot, the recovery is higher than that of the 36 second treated wire, the orange plot. There is a small peak in the recovery, and then declination. This could represent precipitation hardening in the alloy. Although, if this were present, if would be expected for this similar condition to be reflected in the deformation of the wire as well. Since there is no definite peak in any of the heat treatments in the deformation test, the peaking in the recovery phase is not likely to represent precipitation hardening, but rather is due to the primitive aspects of these initial heat treatment processes. Multiple reproductions of these heat treatments would be required to investigate this aspect. This is not the scope of this research, plus there are material supply and time limitations. Since there is no peak and then declination in the deformation results of theses wires, it is suggested that either the aging temperature or the aging time should be increased until the deformation and recovery peaks begins to fall off. This would be a definite sign of precipitation hardening. Although, overaging in not seen in these heat treatments, there is a obvious reduction in SE and a definite presence of a local SME in the wires, and this is the ultimate goal. Next the results for the treatments on the 0.76mm diameter wire are investigated.

The results of the deformation and recovery test on the 0.76mm case are shown in Figure 63, below. In Figure 63 the deformation for the heat treatments that occurred over 36 seconds, the blue plot, showed better deformation characteristics than the 360 second treatments, the red plots. For each treatment there is an obvious peak in deformation at the 1000K heat treatments, and this obviously indicates that for this diameter wire and treatment the SME is best realized at 1000K, regardless of treatment time. This suggests that there is a Ni rich phase precipitating out, due to the loss of the SE property. But as previously

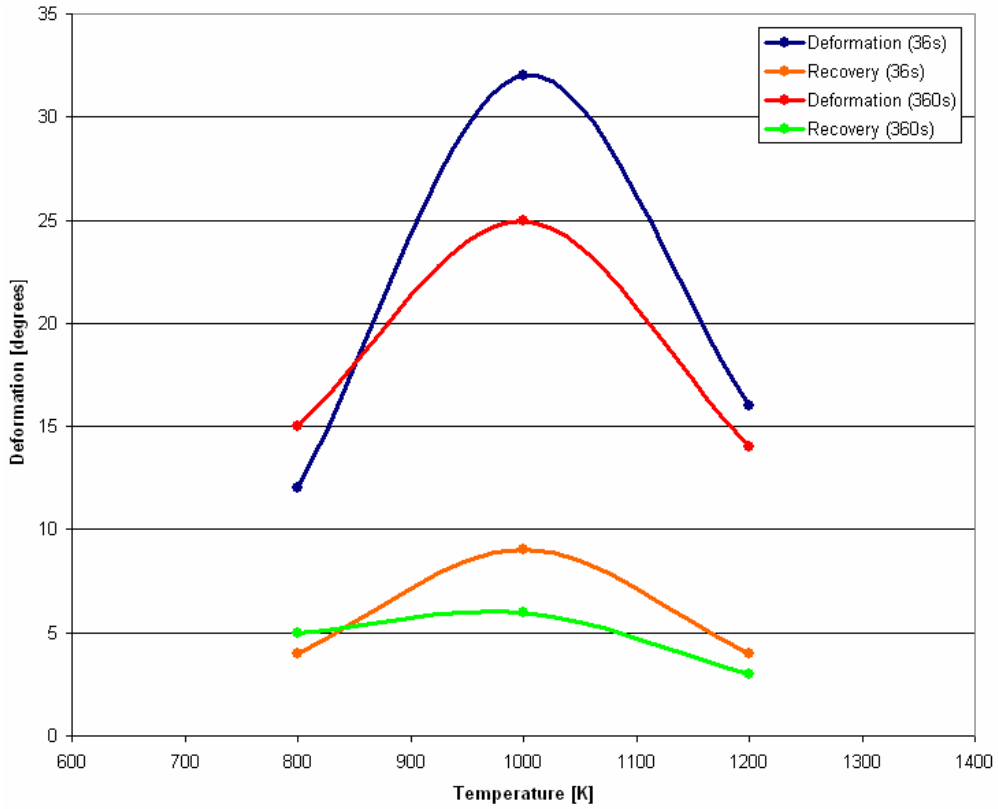

Figure 63. Results of deformation and recovery test for the 0.76mm diameter wire.

mentioned, if two much of the phase is precipitated, then internal stresses are built up at grain boundaries and then the martensitic transformation for the shape memory recovery to occur is resisted, and this is exemplified in both treatments at 1200K due to the reduction in deformation. Now if one is to compare the difference between the 36 second treatment and the 360 second treatment, each temperature should be examined. At the 800K temperature, it is seen that the 360 second treatment produces better deformation. This suggests that since the aging temperature is lower, it takes more time for the precipitates to form; therefore, the 360 second case shows better deformation at this temperature. But, at the next aging temperature, 1000K, the 36 second heat treatment shows the best deformation properties yet. This signifies that when the wire is aged 360 seconds too many precipitates form, causing the SME to be reduced. Then at the 1200K aging temperature, the 36 second treatment still shows better deformation than the 360 second treatment at this temperature, hence the 360 second case has been precipitation hardened more. As previously mention though, the 1200K case for both lengths of treatments, shows precipitation hardening when compared to the 1000K case. The point that is being made here is that the 36s-1200K shows significant

precipitation hardening, but not as much as the 360s-1200K treatment. This is expected since the treatment is longer. If the recovery results are examined, the 36 second treatment, the orange plot, and the 360 second treatment, the green plot, show the exact same trends as the deformation results. If the precipitation of a Ni-rich phase is occurring during the heat treatments, the recovery results should be very similar to the deformation results, since the amount of precipitates provides the mechanism for recovery just like they did for the deformation. Therefore, the recovery results simply reiterate the deformation results and prove the trends established defining the phase precipitation instilling the presence of the local SME. Just like in the deformation test, the 36s-1000K treatment shows the overall best recovery, and the 1000K displays the best temperature to achieve maximum recovery. Furthermore, 1200K treatments show the presence of precipitation hardening due to the reduced recovery, and the 360 second treatment shows more due to the increased aging time. With both the deformation and recovery results showing the exact same trends, it can be stated with confidence that overaging is shown too occur in the 360 second treatments at 1000K and greater aging temperatures, as well as at 1200K and greater temperatures for specimens aged for 36 seconds. For this particular diameter of wire and heat treatments, the aging of the wire at 1000K for 36 seconds showed the greatest presence of SME locally. Again, the most important goal is the simple presence of a local SME in a superelastic wire, but the presence of overaging signifies that Ni-rich precipitation is actually being formed. This is very important, and reiterates that this laser treatment model is an effective tool in generating localized properties in SMA wires.

While ideal shape memory characteristics may have not been achieved in the superelastic wires, the laser treatment model did provide a precisely controlled treatment which did locally change the properties of the superelastic wire so that a shape memory effect was observed in the wire. This validates the laser treatment model as a tool for SMA treatment which produces localized properties.

8 CONCLUSIONS

A localized heat treatment system based on a one-dimensional heat transfer model coupled with the precise control of a high powered fiber laser has been developed. With a prescribed heat treatment temperature profile, this model can accurately predict the temperature distribution in the wire as well as generate the necessary logic to perform that particular laser treatment using the laboratory setup described in the thesis. In this particular setup a variable flow inert gas heat treatment chamber, VFIGHTC, has been specially designed in which the tailored laser treatments are performed. The VFIGHTC has been proven to eliminate the formation of oxides due to the heat treatment without adding significant cooling effects to the treatment. Several experiments have been performed and presented in which various heat treatments are prescribed based on the model, and validated by the real-time thermocouple temperature measurements. A relation of the beam absorption and the wire's diameter has been established, and proven to be consistent across several different diameter sizes of wire. Due to the model's built-in capabilities, such as scanning laser beam, pulsing laser beam, and Gaussian beam segmentation, it is a very desirable tool for the use of localized heat treatments in shape memory alloys. More studies are needed to determine specific heat treatment process for desired SMA properties which go beyond the scope of this thesis. For current work, it has been demonstrated that localized changes in superelasticity occur, and the treated region of a superelastic wire takes on shape memory effect properties. Signs of overaging occurred, which resulted in partial recovery of superelastic effect due to the precipitates. In conclusion, a laser treatment tool has been successfully developed that can create tailored heat treatments that induce localized properties in shape memory alloy wires.

9 FUTURE WORK

As stated before, this laser heat treatment model is only the first step in developing the localized shape memory or superelastic effects. Now that there is a model that can provide a precise heat treatment, as defined by the operator, different methods of heat treating can be explored to obtain the best possible set of SME and SE properties on one wire. This is likely to be the next step in this research, but sufficient experience and

background in shape memory alloys is necessary to develop heat treatments due to the alloy's sensitive nature.

A new version of the model could be developed to include forced convection. The addition of forced convection would allow one to keep the localization of the heat treatment even smaller by removing the input energy before it even has time to propagate in the medium.

If a thermal imaging camera is implemented in the laser treatment setup, then closed loop forms of control could be added to the laser treatment model. The power of the laser could be dynamically controlled based on the readings of temperature in the wire from the camera. Adding in this feature would simplify the logic used to control the laser by adding in looping features instead the current rigid switching profile produced by the laser treatment model.

After the laser treatment model is used to successfully create co-existing SME and SE properties, new products and devices could be made. One example of a device that could be designed from this research is a temperature dependent flow control valve. Figure 64 shows a 2-D schematic of the idealized design and operation. In Figure 64 part A the valve is exposed to a flow with at an initial temperature, and the valve is fully open. In part B, the flow inlet temperature is increased, causing a region of the SMA valve spring, shaded in red, to transform to a set shape that is longer that the original length. This would partially close the valve. In part C, the flow inlet temperature has increased even further, causing another part of the spring, shaded in blue, to transform and fully close this valve. The example shows how a single SMA valve spring could have multiple transformation temperatures, and depending on how hot the inlet flow is, the valve will allow a certain percentage of passage. The characteristics of this valve are determined solely by heat treatment applied to the SMA valve spring, which would not be capable without a localized heat treatment method that utilizes the laser treatment model in this research. While there are currently commercial products that perform flow restriction based on temperature, this method is a much simpler design.

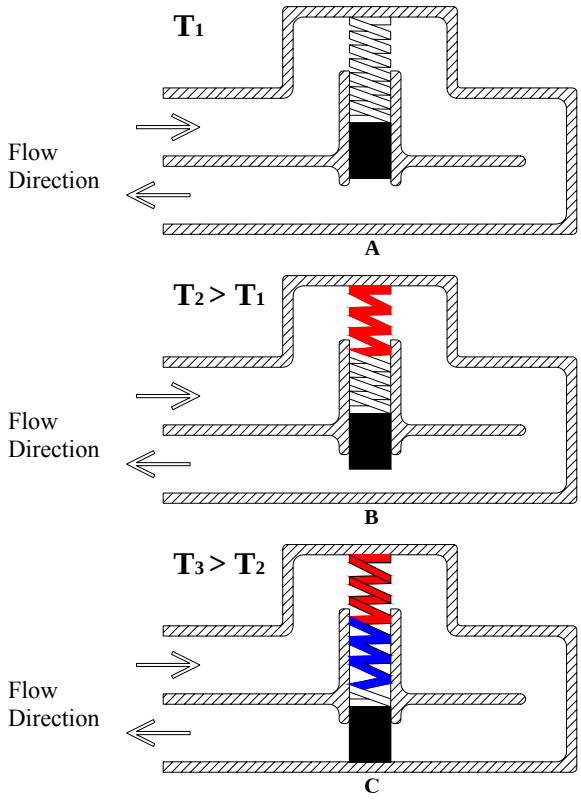

Figure 64. Temperature dependent flow control valve using specially designed SMA spring.

Another example of a device that could be produced from this research is a solid form hinge. Figure 65, below, shows the idealized design and operation. In Figure 65 a SMA hinge is shown in its two inherent states that consist of a single piece of material. A typical hinge consists of three parts, two plates and a pin, whereas this hinge is made from one sheet of SMA. The disadvantages of the typical hinge are the forming the goes into fabrication of the hinge, the friction issues associated with the pin, and the need for some external force to actuate the hinge. The hinge above would be constructed of a work harden SMA, for rigidity and strength, with a thin region down the middle of the hinge that has been treated to have a shape memory effect, and this is where the hinge will bend. This treatment would not be possible without a localized heat treatment method that utilizes the laser treatment model in this research. By applying Joule heating, via an electric current, across the hinge, actuation of the hinge could occur. The advantages of this are: there is no need for an external force to actuate the hinge, just and electric current, there are no friction issue associated with this solid form hinge, and the fabrication is much simpler than that of the typical hinge.

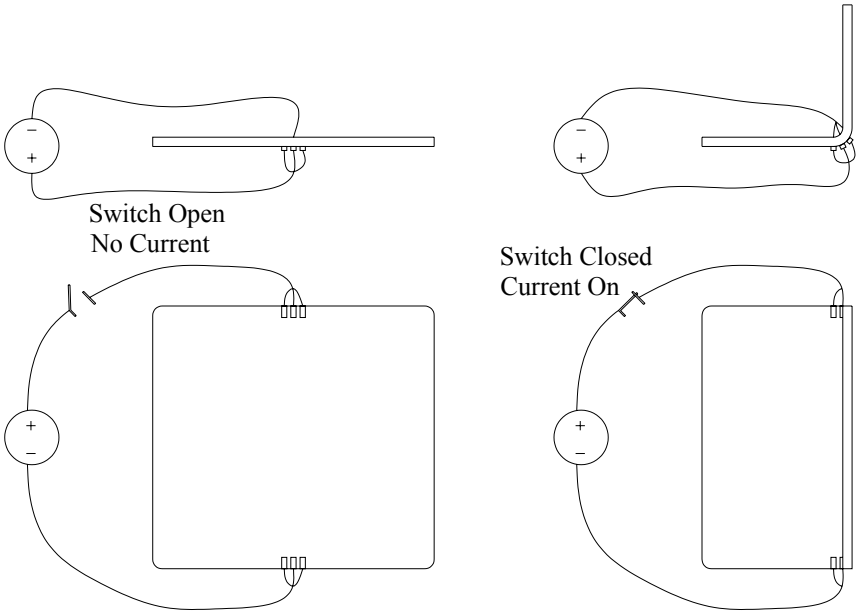

Figure 65. Solid form hinge designed from work hardened Ti-Ni with a shape memory region.

A finial example of the benefits that can be reaped from this research is in artery stents used medical applications, which is an area that shape memory alloys have already gained much use. Figure 66, below, shows the current design of these stents and the shape of the artery in which it is placed.

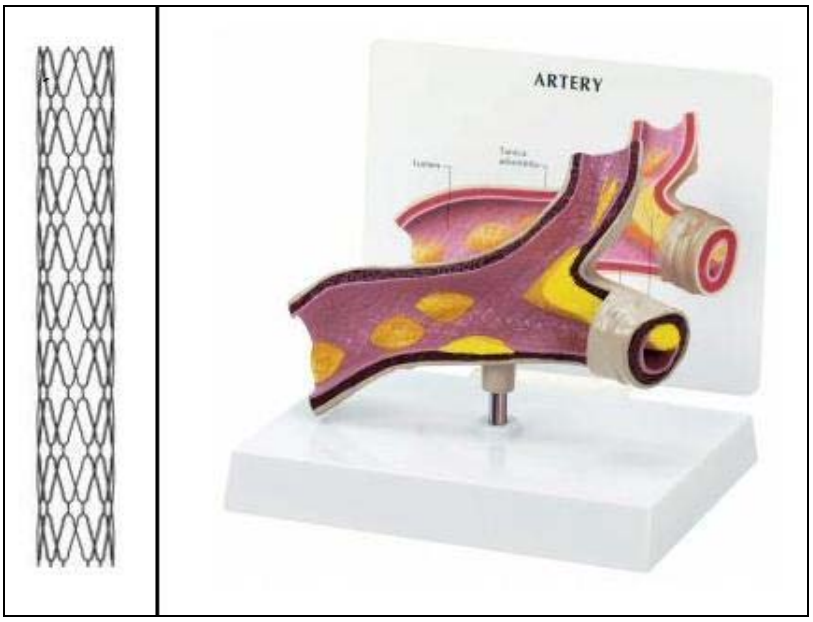

Figure 66. Typical stent used to support an artery, left, and the shape of a typical artery that it would be used in, right. (www. istockphoto.com, 2004)

Being able to locally heat treat a stent like the one shown in Figure 66 would allow the stent to have certain areas with a particular set shape, and the collection of these shape set regions could create a complex overall shape that would allow the stent to tailor shaped for an individual's artery. This would help to eliminate the likelihood of a stent slipping out of place when placed in the body, and this is very important when these stents are placed in arteries near a patient's heart.

10 BIBLIOGRAPHY

1. Begmann, H.W., Eltze, K., 1987, and Mordike, B.L., ed., "Annealing by laser treatment," *Laser Treatment of Materials*, Informationsgesellschaft-Verlag, Germany, 419-420.
2. Bellouard, Y., Lehnert, T., Bidaux, J.-E., Sidler, T., Clavel, R., and Gotthardt, R., 1999, "Local annealing of complex mechanical devices: a new approach for developing monolithic micro-devices," *Materials Science and Engineering*, **A273-275**:795-798.
3. Callister, W. D., 1997, *Materials Science and Engineering and Introduction*, 4th, John Wiley & Sons Inc., New York, 322 & 335-336.
4. Funakubo, H., ed., 1984, *Shape Memory Alloys*, Gordon and Breach Science Publishers, New York, 15-16, 30 & 196-197.
5. Gapontsev, V., and Krupke, W., 2002, "Fiber lasers grow in power." *Laser Focus World*, **8:**83-87.
6. Gapontsev, V.P., and Samartsev, L. E., 1991, "High-power fiber laser," Optical Society of America Trends in Optics and Photonics Series on Advanced Solid-State Lasers Proceedings, **6**:258-262.
7. Gautier, E., Patoor, E., Berveiller, M., ed., and Fischer, F.D., ed., 1997, "Experimental observations for shape memory alloys and transformation induced plasticity phenomena," *Mechanics of Solids with Phase Changes*, Springer-Wien, New York, 69-103.
8. Gil, F.J., and Planell, J.A., 2000, "Behaviour of normal grain growth kinetics in single phase titanium and titanium alloys," *Materials Science and Engineering*, Elsevier Science S.A., **A283**:17–24.
9. Gnanamuthu, D.S., and Shankar, V.S., Jacobs, R.R., ed., 1985, "Laser heat treatment of iron-based alloys," *Proceeding of SPIE-The International Society for Optical Engineering*, **527**(11):56-72.
10. Hafez, M., Bellouard, Y., Sidler, T., Clavel, R., and Salathe, R.P., 2000, "Local annealing of shape memory alloys using laser scanning and computer vision," *First*

International Symposium on Laser Precision Microfabrication, Proceeding of SPIE-The International Society for Optical Engineering, **4088**:160-163.

11. Hesselbach, J., and Janocha, J., ed., 1999, *Adaptronics and Smart Structures*, Springer-Verlag, New York, 144-146.
12. Hitz, B., Ewing, J.J., and Hecht, J., 1991, *Introduction to Laser Technology*, 2nd, IEEE Press, New York, 3-5.
13. Hodgson D. E., Russell, ed., and Pelton, ed., 2000, "Fabrication, Heat Treatment and Joining of Nitinol Components" *SMST-2000 Proceedings of the Third International Conference on Shape Memory and Superelastic Technologies*, 11-24.
14. Hsieh, S. F., and Wu, S. K., 1997, "A study on the nickel-rich ternary Ti-Ni-Al shape memory alloys," *Journal of Materials Science*, **32**:989-996.
15. Icardi, U., 2001, "Large bending actuator made with SMA contractile wires: Theory, numerical simulation, and experiments," *Composites Part B: Engineering*, **32-3**:259-267.
16. Jenkins, F.A., and White, H.E., eds., 1976, *Fundamental Optics*, 4th, McGraw-Hill Book Company, New York, 535.
17. Jiangnan, L., Jianlu, M., Zhengpin, W., and Guangxi, W., 2003, "Effects of Aging Treatment on Shape Memory Characteristics of Ni-Ti-Ta Alloy," *Rare Metal Material and Engineering*, **32**(10):777-781.
18. Kaieda, Y., 2003, "Fabrication of composition-controlled Ti-Ni shape memory wire using combustion synthesis process and the influence of Ni content on phase transformation behavior," *Science and Technology of Advanced Materials*, Elsevier Science S.A., **4**:239-246.
19. Khalil-Allafi, J., Dlouhy, A., and Eggeler, G., 2002, "Ni_4Ti_3-precipitation during aging of NiTi shape memory alloys and its influence on martensitic phase transformations," *Acta Materialia*, **50**:4255-4274.
20. Massalski, T.B., Okamoto, H., Subramanian, P.R., and Kacprzak, L., eds., 1990, *Binary Alloy Phase Diagrams*, 2nd, ASM International, Materials Park, OH, **3**:2874.
21. Melton, K.N., Duering, T.W. *et al*., ed., 1990, "Ni-Ti Based Shape Memory Alloys," *Engineering Aspects of Shape Memory Alloys*, Butterworth, London, 28-34.

22. Metev, S.M., and Veiko, V.P., 1994, *Laser-Assisted Microtechnology*, Springer-Verlag, New York, 93-97.
23. Nishida, M., Wayman, C.M., and Honma, T., 1986, "Precipitation Processes in Near-Equiatomic TiNi Shape Memory Alloys," *Metallurgical Transactions A*, **17A**:1505-1515.
24. Otsuka, K., and Kakeshita, T., eds., 2002, "Science and technology of shape-memory alloys: New developments," *Materials Research Society Bulletin*, **2**:91-98.
25. Otsuka, K., and Wayman, C.M., 1998, *Shape Memory Materials*, Cambridge University Press, New York, 3-5, 11, 19, 28-30, 36-42, & 53-55.
26. Pilic, V., 1996, "Profit by selective heat treatment," *Advanced Materials and Processes*, **2**:37-39.
27. Ramrkahyani, D.S., Lesieutre, G.A., Frecker, M., and Bharti, S., 2004, "Aircraft structural morphing using tendon actuated compliant cellular trusses," *AIAA/ASME/ASCE/AHS/ASC Structures, Structural Dynamics & Materials Conference*, **45**:19-22.
28. Sharp, M., Henry, P., Steen, W.M., and Lim, G.C., 1983, "An analysis of the effects of mode structure on laser material processing," *Proc. Laser '83 Optoelectronics Conf.*, Waidelich, Munich, 243-246.
29. Shiner, B., 2005, "Advances in fiber lasers for material processing," *IPG Photonics Corp. Product Presentation Literature*.
30. Shiner, B., 2004, "Fiber lasers for material processing," *IPG Photonics Corp. Press Release*, 1-9.
31. Shu, S. G., Lagoudas, D. C., Hughes, D., and Wen, J. T., 1997, "Modeling of a flexible beam actuated by shape memory alloy wires," *Smart Materials and Structures*, **6**:265-277.
32. Shurcliff, W.A., ed., 1966, *Polarized Light*, Harvard University Press, 78.
33. Surbled, P., Clerc, C., Le Pioufle, B., Ataka, M., and Hiroyuli, F., 2001, "Effect of the composition and thermal annealing on the transformation temperatures of sputtered TiNi shape memory alloy thin film," *Thin Solid Films*, **401**:52-59.

34. Tobushi, H., Nakahara, T., Hashimoto, T., Shimeno, Y., and Tanaka, K., 1998, "Thermomechanical properties of TiNi shape memory alloy and their applications," *Shape Memory Alloys*, 341-348.
35. Wang, G., and Shahinpoor, M., 1996, "New design for a bending muscle with an embedded SMA actuator," *International Society for Optical Engineering*, **2715**:51-61.
36. Xie, Q., Huang, W., Hong, M., Song, W., and Chong, T.C., 2003, "Excimer laser annealing of TiNi shape memory alloy thin film," *SPIE-The International Society of Optical Engineering: Third International Symposium on: Laser Precision Microfabrication*, **4830**:403-407.
37. Yoshida, I., Monma, D., Iino, K., Ono, T., Otsuka, K., and Asai, M., 2004, "Internal friction of Ti-Ni-Cu ternary shape memory alloys" *Materials Science and Engineering*, **A370**:444-448.
38. Zhang, C., Thoma, P.E., Zee, R.H., and George, E.P., ed., 1997, "The influence of Hafnium content, cold work, and heat treatment on the R-phase transformation of NiTi based shape memory alloys," *Materials for Smart Systems II*, **459**:281-293.
39. Zwillinger, D., 2003, *Standard Mathematical Tables and Formulae*, 31st, Chapman & Hall/CRC, New York, 443.

11 APPENDICES

11.1 Appendix: Background on Shape Memory Alloys

One of the defining properties of a SMA is its transition temperatures. It is particularly important to understand how the crystallography dictates which effect will appear and the temperature ranges, i.e. the transition temperatures, under which the effect will occur. When the SMA is above the Austenite transition temperature it has a crystalline structure that takes on a high elastic modulus and this is due to the symmetry in the crystalline structure, referred to as the parent phase. The parent phase is shown below in Figure 67. But when the SMA is below the Martensite transformation temperature a martensitic crystalline structure will be more thermodynamically stable. This is a twinned martensite phase, which means the boundaries can be easily moved, thus the SMA can be deformed with quite low forces in this state.

The martensite phase in SMA is not the typical martensite phase found in steel. The martensite phase here is a relatively ductile and soft phase. By definition the martensitic transformation is a diffusionless phase transformation in solids, in which atoms move cooperatively, and often by a shear-like mechanism. (Otsuka and Wayman, 1998) Typically the parent phase is a high temperature cubic phase and the martensite is a lower temperature and lower symmetry phase.

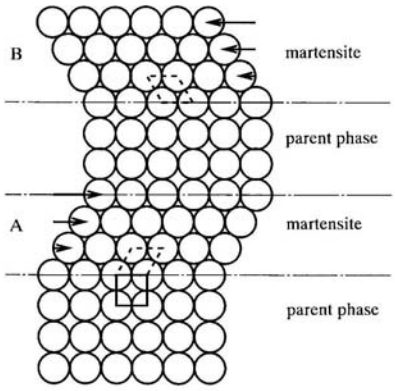

Figure 67. Parent and martensitic phases. (Otsuka and Wayman, 1998)

Therefore, the martensite phase is not defined by its renowned mechanical properties typically associated with steel, but rather by the diffusionless transformation from which it is formed. The martensite transformation (MT) is a first order transformation, it proceeds by nucleation and growth, and a large strain arises around the martensite when it is formed in the parent phase. The strain is attributed to the shape change, shown in Figure 68 (a), inherent in MT. The strain, which must be must be reduced in order for nucleation and growth to occur, is relieved in two ways; either a slip is introduced as shown in Figure 68 (b), or by introducing twins as shown in Figure 68 (c). The shearing shown in Figure 68 is a lattice invariant shear, since neither process changes the structure of the martensite. The kind of alloy elements determines whether slip or twinning will occur, but typically twinning is the dislocation found in SMAs, including the Ti-Ni binary alloy. The growth of martensite in its parent phase is shown in Figure 69, below. Here it is easy to see the parent phase, the flat region in light contrast, and the twinned martensite structure, in the spear-like light and dark contrast.

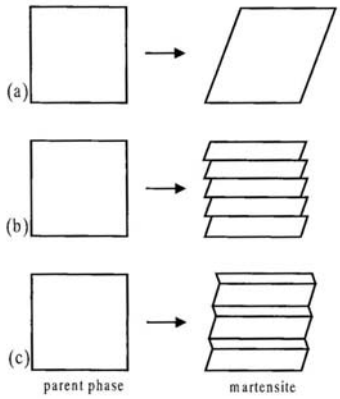

Figure 68. Lattice invariant shear, schematically shown, is required upon MT; (a) shape change upon martensitic transformation; (b) and (c) represent the accommodation of strain by introducing slip (b) or twins (c), respectively. (Otsuka and Wayman, 1998)

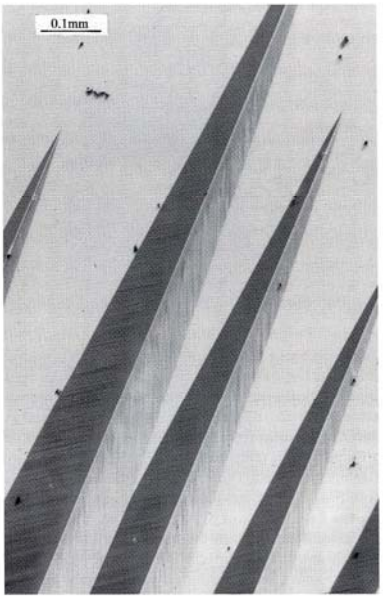

Figure 69. Optical micrograph of spear-like martensite. (Otsuka and Wayman, 1998)

While the twinning of martensite relieves the strain induced by the MT, there is still the issue of the shear that is created. To alleviate this, the different bands of martensite will self-accommodate. This is where many different favorable two or four habit plane variants combine in such of way that there is no bulk stain. This can be seen in Figure 70, below.

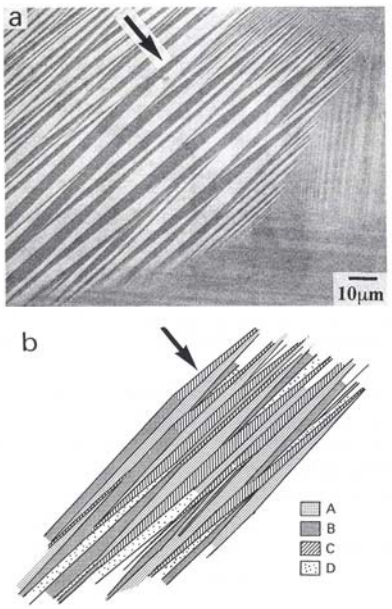

Figure 70. Self-accommodation of martensite; (a) a typical SEM micrograph; (b) Four habit plane variants (A, B, C, D). (Otsuka and Wayman, 1998)

The formation of martensite in SMAs, again, is simply a diffusion transformation with the characteristics listed above, and the MT is typically driven by a temperature change and/or externally induced stain. The MT is what drives the two unique effects exhibited by SMAs, and the MT occurs across transition temperatures. Understanding each transition temperature is crucial to understanding how the MT drives both SME and SE.

Another important aspect of SMA is the inherent hysteresis observed in a stress versus strain plot, as shown in Figure 71 below, again this is another idealized schematic. This hysteresis loop is due to the behavior of the free energies during the phase transformations. It is quite obvious that upon loading and unloading of the specimen it will have deformation, even when the specimen is at under zero load. The SME is exhibited when the specimen is heated to a higher temperature with and held at a constant stress defined by the red point, and the shape of the hysteresis loop progresses as shown in Figure 72.

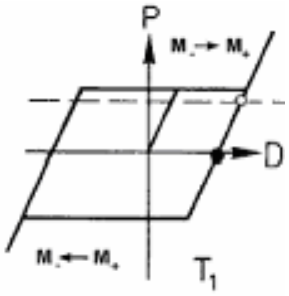

Figure 71. Idealized stress vs. strain in a typical SMA.

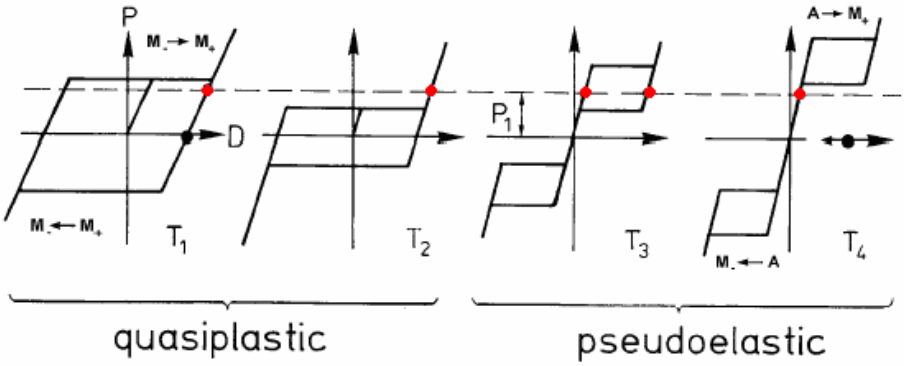

Figure 72. Progression of the idealized hysteresis loop due to increasing temperature.

Notice how increasing the temperature eliminates the hysteresis at constant stress point, which also signifies a phase change. The linear portion between the two smaller hysteresis loops at T_3 and T_4 is representative of the Austenite phase. Even if a specimen is deformed below the A_s, it can regain its original shape by the reverse transformation upon heating the material above A_f. (Otsuka and Wayman, 1998) The deformation can be of any type as long it is below some critical value.

An ideal SME will be below the Mf when at its respective ambient temperature. Figure 73 schematically represents the crystal transformations associated with the SME. Figure 73 (a) is the parent phase of the material when above A_f, and Figure 73 (b) is self-accommodated martensite below M_f. Upon heating and cooling, and in the absence of external forces, the crystal structures will cycle between (a) and (b), respectively. If an external force is applied, the twin boundaries move so as to accommodate the applied stress, as shown in (c) or (d), and if the stress is high enough, it will become a single variant of martensite under stress. When the specimen in (d) is heated above A_f, the reverse transformation occurs, and the original shape is regained as in (e). The example above assumes that the deformation proceeds solely by the movement of twin boundaries and that the transformation is crystallographically reversible. If any of these conditions are not satisfied the complete SME is not obtained.

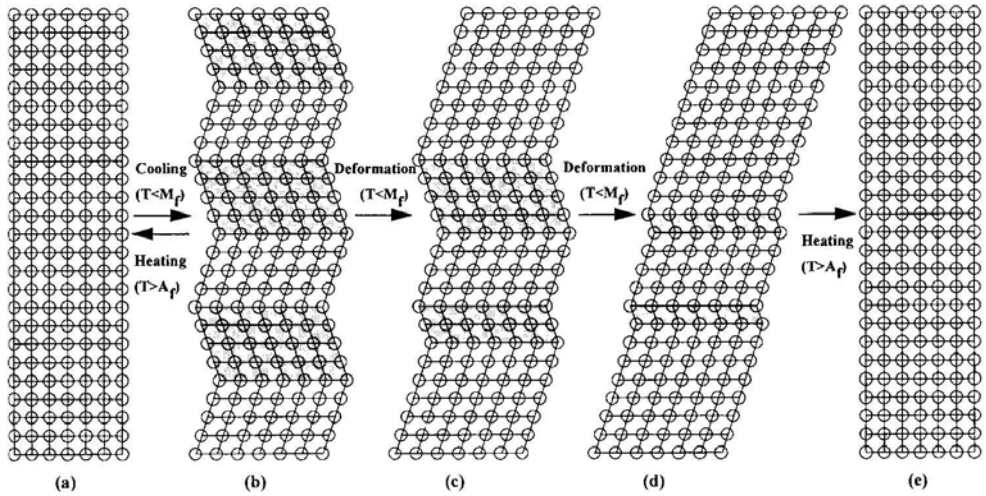

Figure 73. Mechanism of SME; (a) original parent single crystal, (b) self-accommodated martensite, (c-d) deformation in martensite proceeds by the growth of one variant at the expense of the other; (e) heating above Af, each variant reverts to the parent phase (Otsuka and Wayman, 1998)

The SE occurs only when the material is above the A_f. The material tends to behave in an elastic fashion up to some critical stress load, σ_s, and this is shown below in Figure 74. (Gautier and Patoor, 1997) When this critical stress, σ_s, is reached the transformation strain plays the major role. When the stress is higher than σ_f then the elastic behavior of the martensite is observed. On unloading, the same general shape is observed, but now a hysteresis loop is present, where σ_{As} represents the beginning of the reverse transformation, and the σ_{Af} is the end of the reverse transformation. The SE is realized when a specimen is stressed above Af, and is due to the formation of a martensitic phase that is stress induced. (Otsuka and Wayman, 1998) Figure 75 shows the growth of martensite, the light contrast, in the parent phase, the dark contrast.

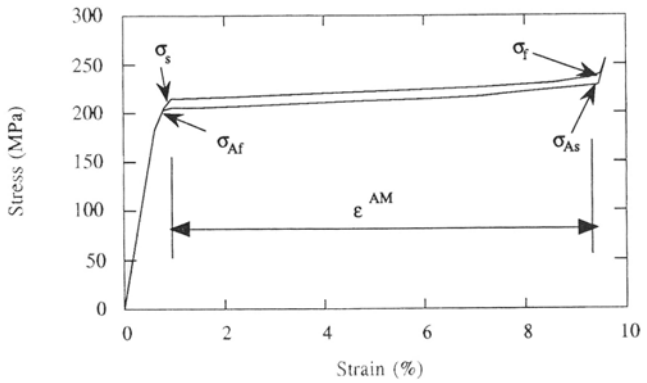

Figure 74. Superelastic behavior. (Gautier and Patoor, 1997)

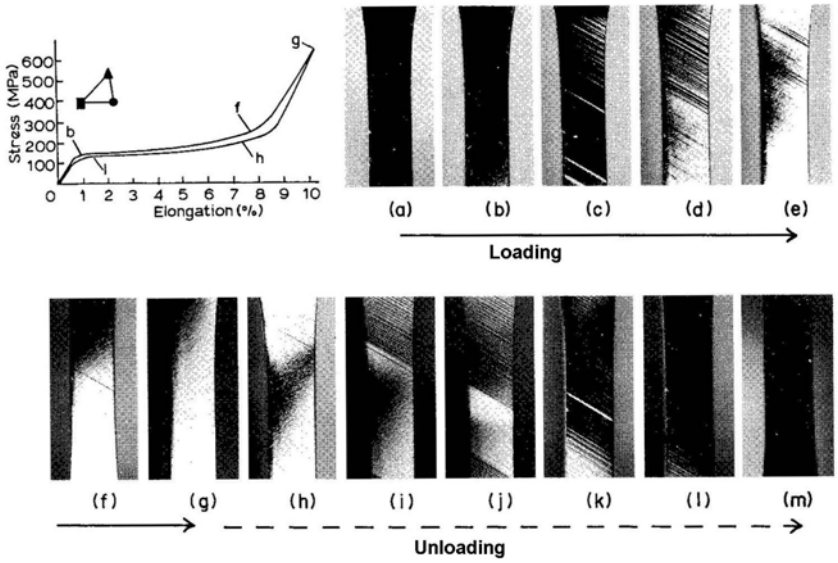

Figure 75. Stress-induced martensite which drives the SE. (Otsuka and Wayman, 1998)

When the sample is strained martensite will form to accommodate the internal stresses that are being created. This parallels the stresses that are induced upon cooling below As and the formation of martensite which the SME. The martensite will continue to grow and nucleate as shown in Figure 75 (a)-(g). But once the loading is released the martensite will begin a reverse transformation back to the parent phase, since the martensite is only stable under stress, and this is shown in Figure 75 (g)-(m).

There is another phase to be considered when dealing with a near-equiatomic Ti-Ni alloys, and that is the Rhombohedral phase, also know as the R-phase. This phase has a triagonal structure, and it is evident only in certain Ti-Ni alloys. (Otsuka and Wayman, 1998) Factors such as Ni content and the addition of alloying elements determine how prominent the R-phase is in the phase transformations. When it is identifiable, it occurs between the martensite and austenite phase transformation. When austenite transforms to the R-phase nucleation and grain growth occur. The R-phase will nucleate from the dislocations in the structure, join and continue to grow. Upon further cooling the plates will continue to form and finally the entire region changes to the R-phase. Subsequently, upon heating the R-phase will shrink and disappear in the same manner as they grew. The appearance and disappearance of the R-phase repeats in the same manner upon repeated cooling and heating, and it is well known that the rhombohedral phase transformation has superior cyclic deformation properties when compared to the martensite phase transformation. (Tobushi *et al.*, 1998) Heat treatment and cold work can affect the transformation temperature of the R-phase. For a Ti rich binary SMA, the austenite to R-phase transformation temperature decrease with increasing cold work at lower heat treatment temperatures, and is not sensitive at all to cold work at higher heat treatment temperatures. (Zhang *et al.*, 1997) Similarly, the transformation temperature will decrease with decreasing heat treatment temperatures, and it tends to be the greatest for large amounts of cold work. Furthermore, at the higher heat treatment temperatures the R-phase transformation is not observed, no matter the amount of cold work.

11.2 Appendix: Larger Version of Ti-Ni Binary Phase Diagram

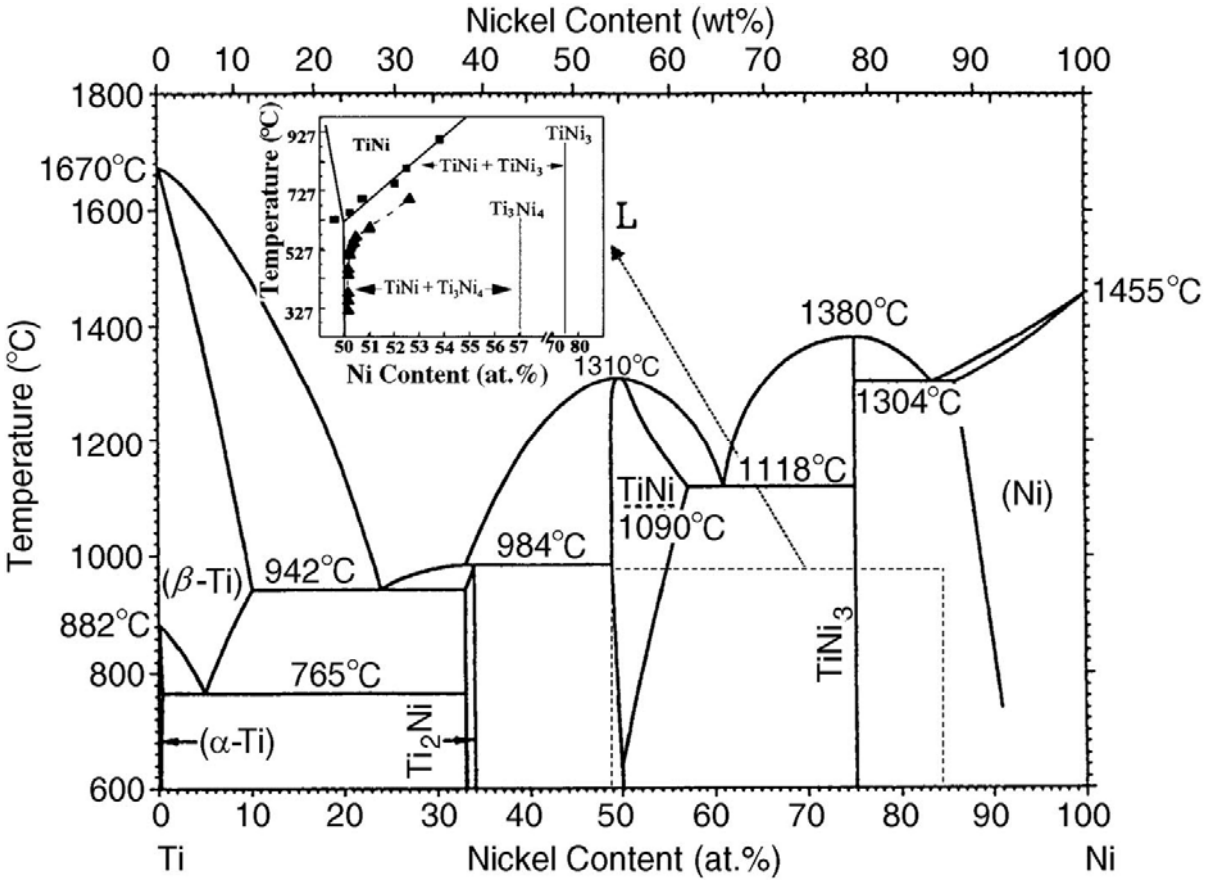

Figure 76. Phase diagram for Ti-Ni alloy

11.3 Appendix: Background in Heat Treatments

Aging, as it is commonly called, is really a precipitation heat treatment in which the supersaturated solid solution is heated to some intermediate temperature in the α+β two-phase region. (Callister, 1997) Here diffusion rates increase to the point that β phase precipitates and form finely dispersed particles. The time it takes to form the desired amount of precipitate is called the aging time, and this can be from a few minutes to a few hundred hours. After this time the heating is removed and the workpiece is allowed to air cool naturally. Due to lengthy heating process required to age a sample, the finished product is not generally affected by cooling time. The formation of the precipitate is largely dependent not only on the composition of the sample, but also largely depends on the time and temperature at which a sample is aged. The effect of aging on the mechanical properties generally includes an increase in strength and hardness, but if aging is carried out for too long overaging can occur. When overaging occurs the mechanical properties actually stop increasing and begin to decrease. Another heat treatment process, annealing, is performed in a similar manner as aging, but it affects the properties of the workpiece quite differently.

Annealing is a heat treatment process that is carried out in three distinct stages: (1) heating to the desired temperature, (2) holding or "soaking" at that temperature, and (3) cooling, usually to room temperature. (Callister, 1997) Time is a very important parameter in each step and will ultimately dictate the effects of the treatment process. Annealing can be used to increase softness, ductility, toughness, relieve stresses, and produce a desired microstructure. Process annealing is a specific type of annealing in which the heat treatment is used to combat the adverse effects of cold work. After process annealing a workpiece will be softened with an increase in ductility as compared to the previously strain hardened material. This process is generally used during and after fabrication to reduce the possibility of fracture and to reduce the required force to perform subsequent deformation procedures. Stress relief annealing is used to relieve internal residual stresses that could have developed form plastic deformation process (e.g. machining and grinding), nonuniform cooling during fabrication, and phase transformation that is induce upon cooling wherein parent and product phases have different densities. Usually annealing temperatures are low enough to have a negligible effect on cold work and other heat treatments, but held long enough for the

workpiece to reach a uniform temperature and then air cooled to room temperature. The usage of the above heat treatment processes is almost always across the entire workpiece, but sometimes it is quite desirable to localize the heat treatment.

Localization of heat treatments are used to change the material's properties only over a small region, such as localized hardening of gear teeth, stress relief and repair of welded joints, annealing of work hardened flexible joints, etc. Developing a localized heat treatment in a material would allow the material to exhibit different properties across the length of the material, which in turn would allow an engineer to tailor a material to meet different specific demands on the same workpiece. This can be quite advantageous when one workpiece is desired to be subjected to very different loading cases, temperature differences, etc. Typically an entire metal part is heat treated after machining to improve mechanical properties such as yield strength, hardness, and resistance to brittle failure. The part may not provide the optimum performance in service if different properties are required at different locations. Also, heat treating a whole part may also subject areas to unnecessary distortion. Localized hardening can remedy both these problems. For example, the internal edges of the claw on a hammer requires the high yield strength and hardness to resist deformation and wear due to extracting nails, but the rest of the cross-section of the claw must resist brittle failure, thus a localized hardening is required on the internal edges only. Also, localized hardening is very useful in increasing the wear resistance of pinion gears, splines, and journals on shafts. (Pilic, 1996) During fabrication of many metal parts cold deformation must be performed several times until a piece is in its final shape. Cold deformation leads to an increase in strength and hardness, but a decrease in ductility. If only a small portion of a part requires further deformation, localized annealing would be the best method of restoring ductility so that the final shape can be set. (Pilic, 1996) Localized annealing has been used during the fabrication of brass door knobs, aluminum reflectors, and stainless steel wheel disk. One of the complexities of localized heat treatment is the ability to keep the treatment effects confined to the desired area, also finding a heat source to apply the heat so preciously can be difficult. Induction coils are one of the primary means of conducting localized heat treatments, and lasers are becoming ever more popular for conducting localized heat treatments for fine wires, narrow tubes, thin plates, and micro-devices.

11.4 Appendix: Background on Lasers

The following is a list of important factors for laser heat treatment: intensity profile of laser beam, beam absorption, heat conduction from the surface into subsurface layers, and structural transformation in workpieces along the regions subjected to a thermal cycle. (Gnanamuthu and Shankar, 1985) While a Gaussian profile beam is most desirable for welding and cutting applications, due to the ability to focus the beam to the smallest spot size, thus creating the highest power density, this can cause non-uniform surface heating, thus causing localized melting. The need for laser beams with uniform spatial intensity will require the integration of special optics, especially if one is using a fiber laser; because of its near Gaussian beam profile. One way of creating a uniform density beam is to dissect the beam into a large number of segments and superposition those segments to a common focal point using a beam integrator. A typical setup to perform this beam transformation is to have the beam pass to a flat mirror, then a spherical convex mirror, and then to a spherical concave beam integrator. All of these should be water cooled to dissipate the energy absorbed from the laser beam. (Gnanamuthu and Shankar, 1985) Another important aspect of laser heat treatment is the beam absorption along the metal surface. Two common ways of increasing the absorption of the laser beam is to coat the workpiece or use polarized light. Coating the metal with zinc, manganese, iron phosphate, or paint that contains a carbon black and sodium or potassium silicate all increase the absorption with a near inferred laser beam. Also, metals have a lower reflectance for linear polarized electromagnetic radiation. (Jenkins and White eds., 1976) When an unpolarized beam is incident on a metal mirror at a specific angle of incidence, the reflected beam will be linearly polarized. (Gnanamuthu and Shankar, 1985) When a beam is linearly polarized it's predominate vibration direction is perpendicular to the plane that contains both the incident laser beam and the normal to the reflecting surface. Below, Figure 77 shows the conversion of the unpolarized beam to a linearly polarized beam by reflection at a specific angle of incidence.

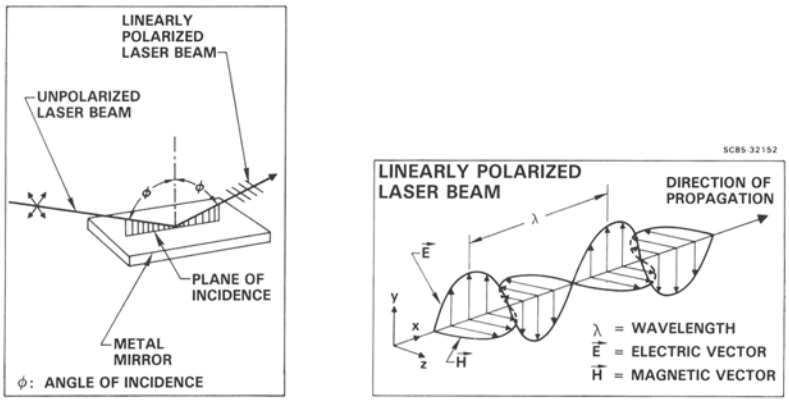

Figure 77. Conversion of an unpolarized beam to a polarized beam. (Shurcliff ed., 1966)

A laser seems to be quite a likely candidate to induce a localized heat treatment, and this is due to its ability to focus a beam of light to a very tiny area and exceed heating and cooling rates of 10^8 K/s. (Metev and Veiko, 1994) This would allow the precise control of thermally-induced structural modifications of the material only in the zone under treatment, thus creating a sharp control boundary where different material properties can exist on un-irradiated areas. The size of the heat affected zone is determined initially by the depth, δ, of light penetration in the medium, and increases with the time, t, as $\sqrt{\kappa t}$, where κ is the thermal diffusivity of the solid. Laser heating can cause the same conventional phenomena that other types of heating induce, and this includes activating diffusion processes in solids and certain chemical reactions on the surface and adjacent layers. Also, the speed of heating (up to 10^{10} K/s) and cooling (up to 10^8 K/s) that can be achieved with lasers allows phase transitions to become possible due to the crystal lattice rearrangement. Certain high-temperature structural modifications can be preserved after fast cooling, which otherwise disappear under slow cooling.

One of the most common heat treatment processes with a laser beam is annealing, although bulk treatments with lasers are still not widely used due to the low efficiency characteristically associated with lasers. (Begmann and Eltze, 1987) However, there are special applications where it is beneficial to use a laser for bulk treatments. One example is the soft annealing of cold worked or age hardened materials. If a cold rolled sheet is formed to a quadrangular tube then it would be necessary to bend the rectangular edge by using several rolling mills. If a complete soft annealing of the rolled sheet where to be used, it

would reduce the overall strength of the piece. A laser makes it possible to only local soft annealing the regions that are to bend. (Begmann and Eltze, 1987) See Figure 78.

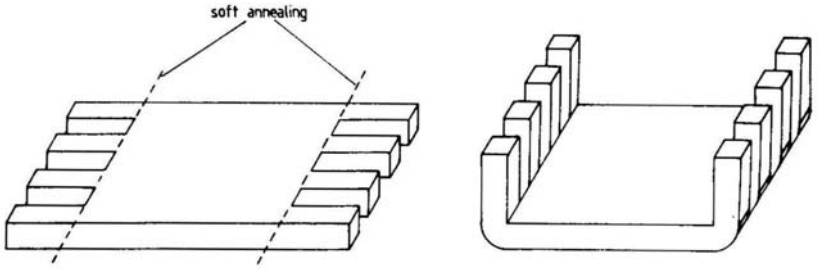

Figure 78. Local soft annealing of quadrangular tube. (Begmann and Eltze, 1987)

11.5 Appendix: Derivation of Heat Transfer Equation

The following is a derivation of the local matrices that describe the heat transfer in and out of the control volume. First begin with the basic energy equation:

(28) $$E_{in} + E_g - E_{out} = E_{st}$$

Where: E_{in} = Energy into control volume [W]

E_g = Energy generated inside control volume [W]

E_{out} = Energy out of control volume [W]

E_{st} = Energy stored [W]

Substituting in for these values from Figure 19:

(29) $$\underbrace{q_{cond} + q_{laser}}_{E_{in}} \underbrace{- q_{cond+dx} - q_{conv}}_{E_{out}} = E_{st}$$

Each of the components in Equation 29 can be expanded into:

(30) $$q_{cond} = -k\frac{\partial T}{\partial x} A dt$$

(31) $$q_{cond+dx} = q_{cond} + \frac{\partial q_{cond}}{\partial x} dx$$

(32) $$q_{laser} = Q_{laser} A dx dt$$

(33) $$q_{conv} = h(T(x,t) - T_\infty) P dx dt$$

(34) $$E_{st} = c_p(\rho A dx) dT$$

Where: A = Cross-sectional area of the SMA wire [m^2]

c_p = Specific heat of wire [J/(kg*K)]

h = Convection coefficient [W/(m^2*K)]

k = Thermal conductivity [W/(m*K)]

Q_{laser} = Volumetric laser power [W/m^3]

T = Temperature of a particular point [K]

T_∞ = Ambient temperature [K]

t = Time [s]

x = Position along wire [m]

ρ = Density of SMA wire [kg/m^3]

Combining Equations 29 through 34 the equation for heat transfer in the wire is realized in Equation 35.

(35)

$$E_{st} = -k\frac{\partial T}{\partial x}Adt + Q_{laser}Adxdt - \left(-k\frac{\partial T}{\partial x}Adt + \frac{\partial}{\partial x}\left(-k\frac{\partial T}{\partial x}Adt\right)dx\right) - \left(h\left(T(x,t) - T_\infty\right)Pdxdt\right) = c_p\rho AdxdT$$

Simplifing:

(36) $$Q_{laser}Adxdt - \left(\frac{\partial}{\partial x}\left(-k\frac{\partial T}{\partial x}Adt\right)dx\right) - \left(h\left(T(x,t) - T_\infty\right)Pdxdt\right) = c_p\rho AdxdT$$

Divide through by "Adxdt" to eliminate common terms

(37) $$Q_{laser} + \frac{\partial}{\partial x}\left(k\frac{\partial T}{\partial x}\right) - \frac{hP}{A}\left(T(x,t) - T_\infty\right) = c_p\rho\frac{dT}{dt}$$

The temperature distribution is assumed to be linear in the each finite element. When this approximate solution is substituted into the governing differential equation, Equation 37, an error will result. In order to try and drive this error to zero Galerkin's Method of Weighted Residuals (GMWR) is employed. Let the linear shape function be:

(38) $$N = \left[1 - \frac{\hat{x}}{L}, \frac{\hat{x}}{L}\right]$$

Where: $\hat{x}$ = Distance from left side of finite element [m]

L = Total length of finite element [m]

Rearranging Equation 37:

(39) $$Q_{laser} + \frac{\partial}{\partial x}\left(k\frac{\partial T}{\partial x}\right) - \frac{hP}{A}\left(T(x,t) - T_{\infty}\right) - c_p \rho \frac{dT}{dt} = 0$$

Let: $\Psi = T$, $c_1 = k$, $c_2 = -h*P/A$, $c_3 = h*P/A*T_{\infty}+Q_{laser}$, $c_4 = c_p\rho$ so that the rest of the numerical analysis will be generalized and easier to conceptualize. Rewriting Equation 39 with substitutions:

(40) $$c_1 \frac{\partial^2 \Psi}{\partial \hat{x}^2} + c_2 \Psi + c_3 + c_4 \frac{\partial \Psi}{\partial t} = 0$$

The general form used for GMWR is:

(41) $$\iiint_V RN dV = 0$$

Where: $$R = c_1 \frac{\partial^2 \Psi}{\partial \hat{x}^2} + c_2 \Psi + c_3 + c_4 \frac{\partial \Psi}{\partial t}$$

$$N = \left[1 - \frac{\hat{x}}{L}, \frac{\hat{x}}{L}\right]$$

Substituting in for Equation 41:

(42) $$\iiint_V N_i \left(c_1 \frac{\partial^2 \Psi}{\partial \hat{x}^2} + c_2 \Psi + c_3 + c_4 \frac{\partial \Psi}{\partial t} \right) d\hat{x} d\hat{y} d\hat{z} = 0$$

Since this is only a one-dimensional heat transfer problem in $d\hat{x}$, Equation 42 simplifies to:

(43) $$\int_{\hat{x}} N_i \left(c_1 \frac{\partial^2 \Psi}{\partial \hat{x}^2} + c_2 \Psi + c_3 + c_4 \frac{\partial \Psi}{\partial t} \right) d\hat{x} = 0$$

Due to the linear shape functions used in this model, the term $c_1 \frac{\partial^2 \Psi}{\partial \hat{x}^2}$ will become zero when the approximate solution is substituted in, therefore the second order partial differential term needs to be expressed in first order terms. This can be done by recognizing the use of the chain rule in Equation 44:

(44) $$\frac{\partial}{\partial \hat{x}} \left(N_i \frac{\partial \Psi}{\partial \hat{x}} \right) = N_i \frac{\partial^2 \Psi}{\partial \hat{x}^2} + \frac{\partial N_i}{\partial \hat{x}} \frac{\partial \Psi}{\partial \hat{x}}$$

Rearranging Equation 44 to realize the common term in Equation 43 yields the expansion shown in Equation 45:

(45) $$N_i \frac{\partial^2 \Psi}{\partial \hat{x}^2} = \frac{\partial}{\partial \hat{x}} \left(N_i \frac{\partial \Psi}{\partial \hat{x}} \right) - \frac{\partial N_i}{\partial \hat{x}} \frac{\partial \Psi}{\partial \hat{x}}$$

Substitute Equation 45 into Equation 43 to alleviate the problem with the second order partial differential term:

(46) $$\int_{\hat{x}} c_1 \left(\left(\frac{\partial}{\partial \hat{x}} \left(N_i \frac{\partial \Psi}{\partial \hat{x}} \right) - \frac{\partial N_i}{\partial \hat{x}} \frac{\partial \Psi}{\partial \hat{x}} \right) + N_i \left(c_2 \Psi + c_3 + c_4 \frac{\partial \Psi}{\partial t} \right) \right) d\hat{x} = 0$$

Expanding Equation 46 to realize the different integrations that must be performed as shown in Equation 47:

(47) $$\underbrace{\int_{\hat{x}} c_1 \left(\frac{\partial}{\partial \hat{x}} \left(N_i \frac{\partial \Psi}{\partial \hat{x}} \right) \right) d\hat{x}}_{FirstInt.} - \underbrace{\int_{\hat{x}} c_1 \left(\frac{\partial N_i}{\partial \hat{x}} \frac{\partial \Psi}{\partial \hat{x}} \right) d\hat{x}}_{SecondInt.} + \underbrace{\int_{\hat{x}} c_2 N_i \Psi d\hat{x}}_{ThridInt.} + \underbrace{\int_{\hat{x}} c_3 N_i \, d\hat{x}}_{FourthInt.} + \underbrace{\int_{\hat{x}} c_4 N_i \frac{\partial \Psi}{\partial t} d\hat{x}}_{FifthInt.} = 0$$

Evaluating the first integral ("Firstent." in Equation 47):

$$(48) \qquad \int_{\hat{x}_i=0}^{\hat{x}_j=L} c_1\left(\frac{\partial}{\partial\hat{x}}\left(N_i\,\frac{\partial\Psi}{\partial\hat{x}}\right)\right)d\hat{x} = \int_0^L c_1\left(N_i\,\frac{\partial\Psi}{\partial\hat{x}}\right) = R^1_{1,2}$$

Where: $N_1 = 1-\dfrac{\hat{x}}{L}$

$N_2 = \dfrac{\hat{x}}{L}$

$\Psi = \left(\dfrac{\Psi_j-\Psi_i}{L}\right)\hat{x}+\Psi_i$

Let the solution to Equation 48 be R_1^1 when N_1 is substituted in and let it be R_2^1 when N_2 is substituted.

$$(49) \qquad R_1^1 = c_1(1-\frac{L}{L})\frac{\partial\Psi}{\partial\hat{x}} - c_1(1-\frac{0}{L})\frac{\partial\Psi}{\partial\hat{x}} = -c_1\frac{\partial\Psi}{\partial\hat{x}}\bigg|_{\hat{x}=\hat{x}_i}$$

$$(50) \qquad R_2^1 = c_1(\frac{L}{L})\frac{\partial\Psi}{\partial\hat{x}} - c_1(\frac{0}{L})\frac{\partial\Psi}{\partial\hat{x}} = c_1\frac{\partial\Psi}{\partial\hat{x}}\bigg|_{\hat{x}=\hat{x}_j}$$

Evaluating the second integral ("SecondInt." In Equation 47):

$$(51) \qquad \int_{\hat{x}_i=0}^{\hat{x}_j=L} c_1\left(-\frac{\partial N_i}{\partial\hat{x}}\frac{\partial\Psi}{\partial\hat{x}}\right)d\hat{x} = R^2_{1,2}$$

Let the solution to Equation 51 be R_1^2 when N_1 is substituted in and let it be R_2^2 when N_2 is substituted.

$$(52) \qquad R_1^2 = -c_1\left(-\frac{1}{L}\right)\left(\frac{\Psi_j-\Psi_i}{L}\right)(L) - c_1\left(-\frac{1}{L}\right)\left(\frac{\Psi_j-\Psi_i}{L}\right)(0) = \frac{c_1}{L}\left(\Psi_j-\Psi_i\right)$$

(53) $$R_2^2 = -c_1\left(\frac{1}{L}\right)\left(\frac{\Psi_j - \Psi_i}{L}\right)(L) - c_1\left(\frac{1}{L}\right)\left(\frac{\Psi_j - \Psi_i}{L}\right)(0) = -\frac{c_1}{L}\left(\Psi_j - \Psi_i\right)$$

Evaluating the third integral ("ThirdInt." in Equation 47):

(54) $$\int_{\hat{x}_i=0}^{\hat{x}_j=L} c_2 N_i \Psi d\hat{x} = R_{1,2}^3$$

Let the solution to Equation 54 be R_1^3 when N_1 is substituted in and let it be R_2^3 when N_2 is substituted.

(55) $$R_1^3 = c_2 \int_0^L \underbrace{\left(1 - \frac{\hat{x}}{L}\right)}_{u} \underbrace{\left(\left(\frac{\Psi_j - \Psi_i}{L}\right)\hat{x} + \Psi_i\right)}_{dv} d\hat{x}$$

(56) $$R_2^3 = c_2 \int_0^L \underbrace{\left(\frac{\hat{x}}{L}\right)}_{u} \underbrace{\left(\left(\frac{\Psi_j - \Psi_i}{L}\right)\hat{x} + \Psi_i\right)}_{dv} d\hat{x}$$

Integration by parts will be performed on Equation 55 and Equation 56 to solve the integral. For Equation 55 let $u = \left(1 - \frac{\hat{x}}{L}\right)$, $du = -\frac{1}{L}$, $v = \left(\left(\frac{\Psi_j - \Psi_i}{2L}\right)\hat{x}^2 + \Psi_i\hat{x}\right)$, and $dv = \left(\left(\frac{\Psi_j - \Psi_i}{L}\right)\hat{x} + \Psi_i\right)$.

(57) $$\int u dv = uv - \int v du \rightarrow$$

$$R_1^3 = c_2\left[\left(1 - \frac{\hat{x}}{L}\right)\left(\left(\frac{\Psi_j - \Psi_i}{2L}\right)\hat{x}^2 + \Psi_i\hat{x}\right) - \int_0^L \left(\left(\left(\frac{\Psi_j - \Psi_i}{2L}\right)\hat{x}^2 + \Psi_i\hat{x}\right)\left(-\frac{1}{L}\right)\right)d\hat{x}\right] \rightarrow$$

$$R_1^3 = c_2\left[\left(1 - \frac{\hat{x}}{L}\right)\left(\left(\frac{\Psi_j - \Psi_i}{2L}\right)\hat{x}^2 + \Psi_i\hat{x}\right) - \left(-\frac{1}{L}\right)\left(\left(\frac{\Psi_j - \Psi_i}{6L}\right)\hat{x}^3 + \frac{\Psi_i}{2}\hat{x}^2\right)\right]_0^L \rightarrow$$

$$R_1^3 = c_2\left[\left(1-\frac{L}{L}\right)\left(\left(\frac{\Psi_j-\Psi_i}{2L}\right)L^2+\Psi_i L\right)-\left(-\frac{1}{L}\right)\left(\left(\frac{\Psi_j-\Psi_i}{6L}\right)L^3+\frac{\Psi_i}{2}L^2\right)\right]-c_2[0]\rightarrow$$

$$R_1^3 = c_2\left[\left(\frac{\Psi_j-\Psi_i}{6}\right)L+\frac{\Psi_i}{2}L\right]=\frac{c_2 L}{3}\Psi_i+\frac{c_2 L}{6}\Psi_j$$

(58) $\int udv = uv-\int vdu \rightarrow$

$$R_2^3 = c_2\left[\left(\frac{\hat{x}}{L}\right)\left(\left(\frac{\Psi_j-\Psi_i}{2L}\right)\hat{x}^2+\Psi_i\hat{x}\right)-\int_0^L\left(\left(\left(\frac{\Psi_j-\Psi_i}{2L}\right)\hat{x}^2+\Psi_i\hat{x}\right)\left(\frac{1}{L}\right)\right)d\hat{x}\right]\rightarrow$$

$$R_2^3 = c_2\left[\left(\frac{\hat{x}}{L}\right)\left(\left(\frac{\Psi_j-\Psi_i}{2L}\right)\hat{x}^2+\Psi_i\hat{x}\right)-\left(\frac{1}{L}\right)\left(\left(\frac{\Psi_j-\Psi_i}{6L}\right)\hat{x}^3+\frac{\Psi_i}{2}\hat{x}^2\right)\right]_0^L\rightarrow$$

$$R_2^3 = c_2\left[\left(\frac{L}{L}\right)\left(\left(\frac{\Psi_j-\Psi_i}{2L}\right)L^2+\Psi_i L\right)-\left(\frac{1}{L}\right)\left(\left(\frac{\Psi_j-\Psi_i}{6L}\right)L^3+\frac{\Psi_i}{2}L^2\right)\right]-c_2[0]\rightarrow$$

$$R_2^3 = c_2 L\left[\left(\frac{\Psi_j}{2}-\frac{\Psi_i}{2}+\Psi_i\right)-\left(\frac{\Psi_j}{6}-\frac{\Psi_i}{6}+\frac{\Psi_i}{2}\right)\right]=\frac{c_2 L}{6}\Psi_i+\frac{c_2 L}{3}\Psi_j$$

Evaluating the fourth integral ("FourthInt." in Equation 47):

(59) $$\int_{\hat{x}_i=0}^{\hat{x}_j=L} c_3 N_i d\hat{x} = R_{1,2}^4$$

Let the solution to Equation 59 be R_1^4 when N_1 is substituted in and let it be R_2^4 when N_2 is substituted.

(60) $$R_1^4 = \left[\left(\hat{x}-\left(\frac{\hat{x}^2}{2L}\right)\right)c_3\right]_0^L = \frac{c_3 L}{2}$$

(61) $$R_2^4 = \left[\left(\frac{\hat{x}^2}{2L}\right)c_3\right]_0^L = \frac{c_3 L}{2}$$

Evaluating the fifth integral ("FifthInt." in Equation 47):

$$\int_{\hat{x}_i=0}^{\hat{x}_j=L} c_4 N_i \frac{\partial \Psi}{\partial t} d\hat{x} = R_{1,2}^5 \tag{62}$$

Let the solution to Equation 62 be R_1^5 when N_1 is substituted in and let it be R_2^5 when N_2 is substituted. Note that the partial $\frac{\partial \Psi}{\partial t}$ is essentially a constant in this integration, since the integration is over $d\hat{x}$.

$$R_1^5 = \frac{\partial \Psi}{\partial t}\left[\left(\hat{x} - \left(\frac{\hat{x}^2}{2L}\right)\right)c_4\right]_0^L = \frac{c_4 L}{2}\frac{\partial \Psi}{\partial t} \tag{63}$$

$$R_2^5 = \frac{\partial \Psi}{\partial t}\left[\left(\frac{\hat{x}^2}{2L}\right)c_4\right]_0^L = \frac{c_4 L}{2}\frac{\partial \Psi}{\partial t} \tag{64}$$

Combine Equations 49, 50, 52, 53, 57, 58, 60, 61, 63, and 64 into matrix form:

$$\begin{Bmatrix} R_1 \\ R_2 \end{Bmatrix} = \begin{Bmatrix} -c_1 \left.\frac{\partial \Psi}{\partial \hat{x}}\right|_{\hat{x}=\hat{x}_i} \\ c_1 \left.\frac{\partial \Psi}{\partial \hat{x}}\right|_{\hat{x}=\hat{x}j} \end{Bmatrix} - \frac{c_1}{L}\begin{bmatrix} 1 & -1 \\ -1 & 1 \end{bmatrix}\begin{Bmatrix} \Psi_i \\ \Psi_j \end{Bmatrix} + \frac{c_2 L}{6}\begin{bmatrix} 2 & 1 \\ 1 & 2 \end{bmatrix}\begin{Bmatrix} \Psi_i \\ \Psi_j \end{Bmatrix} + \frac{c_3 L}{2}\begin{Bmatrix} 1 \\ 1 \end{Bmatrix} + \frac{c_4 L}{2}\frac{\partial \Psi}{\partial t}\begin{Bmatrix} 1 \\ 1 \end{Bmatrix} \tag{65}$$

Rearranging Equation 65:

$$\begin{Bmatrix} c_1 \left.\frac{\partial \Psi}{\partial \hat{x}}\right|_{\hat{x}=\hat{x}_i} \\ -c_1 \left.\frac{\partial \Psi}{\partial \hat{x}}\right|_{\hat{x}=\hat{x}j} \end{Bmatrix} + \underbrace{\frac{c_1}{L}\begin{bmatrix} 1 & -1 \\ -1 & 1 \end{bmatrix}}_{[K]_{c_1}}\begin{Bmatrix} \Psi_i \\ \Psi_j \end{Bmatrix} - \underbrace{\frac{c_2 L}{6}\begin{bmatrix} 2 & 1 \\ 1 & 2 \end{bmatrix}}_{[K]_{c_2}}\begin{Bmatrix} \Psi_i \\ \Psi_j \end{Bmatrix} = \underbrace{\frac{c_3 L}{2}\begin{bmatrix} 1 \\ 1 \end{bmatrix}}_{[F]} + \underbrace{\frac{c_4 L}{2}\frac{\partial \Psi}{\partial t}\begin{bmatrix} 1 \\ 1 \end{bmatrix}}_{[C]} \tag{66}$$

Combining like terms in Equation 66 and plugging in for c_1, c_2, c_3, c_4, and Ψ:

(67)
$$\begin{Bmatrix} k\left.\frac{\partial T}{\partial x}\right|_{x=x_i} \\ -k\left.\frac{\partial T}{\partial x}\right|_{x=xj} \end{Bmatrix} + \left\{[K]_{c_1} + [K]_{c_2}\right\}\begin{Bmatrix} T_i \\ T_j \end{Bmatrix} = [F] + [C]\begin{Bmatrix} \frac{\partial T_i}{\partial t} \\ \frac{\partial T_j}{\partial t} \end{Bmatrix}$$

Where:
$$[K]_{c_1} = \frac{k}{L}\begin{bmatrix} 1 & -1 \\ -1 & 1 \end{bmatrix}$$

$$[K]_{c_2} = \frac{hPL}{6A}\begin{bmatrix} 2 & 1 \\ 1 & 2 \end{bmatrix}$$

$$[F] = \left(\frac{hPL}{2A}T_\infty + \frac{L}{2}Q_{laser}\right)\begin{bmatrix} 1 \\ 1 \end{bmatrix}$$

$$[C] = \left(\frac{c_p \rho L}{2}\right)\begin{bmatrix} 1 \\ 1 \end{bmatrix}$$

For the finite elements at the ends of the wire the end effects are ignored due the long length of the wire compared to the cross-sectional area, as well as a small cross-sectional area due to the small diameter of the thin wire. Therefore the first term in Equation 67 is neglected and the general form of Equation 67 is realized as $[K]^e[T] = [F]^e + [C]^e[dT/dt]$. The equation for the elemental conduction matrix is shown below in Equation 68.

(68)
$$[K]^e = \frac{k}{L}\begin{bmatrix} 1 & -1 \\ -1 & 1 \end{bmatrix} + \frac{hPL}{6A}\begin{bmatrix} 2 & 1 \\ 1 & 2 \end{bmatrix}$$

The elemental force matrix is shown below as Equation 69.

(69)
$$[F]^e = \left(\frac{hPL}{2A}T_\infty + \frac{L}{2}Q_{laser}\right)\begin{bmatrix} 1 \\ 1 \end{bmatrix}$$

Elemental condition matrix is shown below in Equation 70.

(70) $$[C]^e = \left(\frac{c_p \rho L}{2}\right)\begin{bmatrix}1\\1\end{bmatrix}$$

Elemental temperature matrix is shown below in Equation 71.

(71) $$[T]^e = \begin{bmatrix}T_i\\T_j\end{bmatrix}$$

The elemental change in temperature with respect to time matrix is shown in Equation 72.

(72) $$\left[\frac{\partial T}{\partial t}\right] = \begin{bmatrix}\frac{\partial T_i}{\partial t}\\ \frac{\partial T_j}{\partial t}\end{bmatrix}$$

Equations 69 through 72 are the core elemental matrices used to construct the global matrices that will represent the heat transfer in the entire wire as a summation of its individual elements. The construction of the global matrix for the wire is actually quite simple. A five element example is give below in Figure 79.

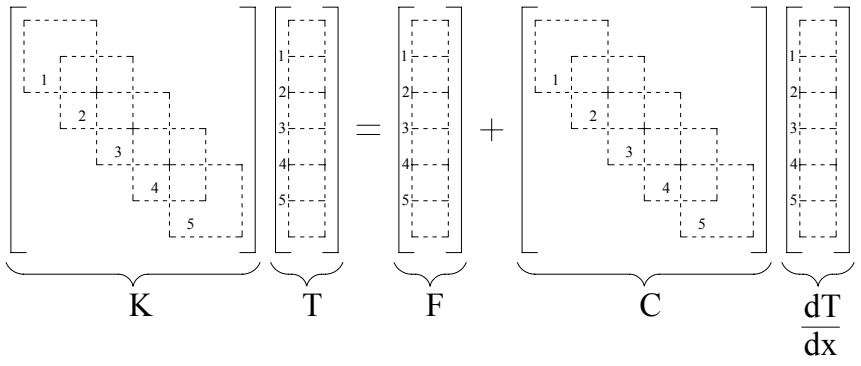

Figure 79. Assembly of the global matrix for a simple four element wire.

$$\begin{bmatrix} K_{1,1}^1 & K_{1,2}^1 & & & & \\ K_{2,1}^1 & K_{2,2}^1+K_{1,1}^2 & K_{1,2}^2 & & 0 & \\ & K_{2,1}^2 & K_{2,2}^2+K_{1,1}^3 & K_{1,2}^3 & & \\ & & K_{2,1}^3 & K_{2,2}^3+K_{1,1}^4 & K_{1,2}^4 & \\ & 0 & & K_{2,1}^4 & K_{2,2}^4+K_{1,1}^5 & K_{1,2}^5 \\ & & & & K_{2,1}^5 & K_{2,2}^5 \end{bmatrix} \begin{bmatrix} T_1 \\ T_2 \\ T_3 \\ T_4 \\ T_5 \\ T_6 \end{bmatrix} = \begin{bmatrix} F_1^1 \\ F_2^1+F_1^2 \\ F_2^2+F_1^3 \\ F_2^3+F_1^4 \\ F_2^4+F_1^5 \\ F_2^5 \end{bmatrix} + \begin{bmatrix} C_{1,1}^1 & & & & & \\ & C_{2,1}^1+C_{1,1}^2 & & & 0 & \\ & & C_{2,1}^2+C_{1,1}^3 & & & \\ & & & C_{2,1}^3+C_{1,1}^4 & & \\ & 0 & & & C_{2,1}^4+C_{1,1}^5 & \\ & & & & & C_{2,2}^5 \end{bmatrix} \begin{bmatrix} \frac{\partial T_1}{\partial t} \\ \frac{\partial T_2}{\partial t} \\ \frac{\partial T_3}{\partial t} \\ \frac{\partial T_4}{\partial t} \\ \frac{\partial T_5}{\partial t} \\ \frac{\partial T_6}{\partial t} \end{bmatrix}$$

Figure 80. Displays the overlapping of elemental variables in the global matrix.

To further explain how the global matrix is assembled, Figure 80 shows the values in each of the elemental matrices overlap in the global matrix. The subscripts in Figure 80 represent the row, column of each variable in the elemental matrix defined by the superscript.

Once the global matrices are formed, the temperature distribution must be determined. Matrix operations can be used to solve the global matrices for the heat transfer equation. The general form of the global matrices is $[K]^g[T] = [F]^g + [C]^g[dT/dt]$. Solve for the change in temperature with respect to time, as shown below.

(73) $$\frac{\partial T}{\partial t} = \frac{[K]^g}{[C]^g}[T] - \frac{[F]^g}{[C]^g}$$

Once this is accomplished, a numerical integrations technique can be used to solve for the temperature distribution of the wire over time. The only requirement is the initial state of the wire. This will generally be ambient temperature. All the mathematical calculations and finite element analysis are computed with Matlab. The numerical integration is also done using a predefined differential equation solver in Matlab.

11.6 Appendix: Derivation of Constants c_1 and c_2

The easiest constant to determine is c_2, and this is done by knowing that where the redline crosses the Gaussian curve in Figure 23 is at a height of $1/e^2 * c_1$ and at the distance of the laser beam radius, as referenced to zero. This would define the beam diameter as centered at zero. The derivation of c_2 is shown below:

(74) $$z(x) = c_1 e^{-c_2 x^2} \rightarrow \frac{1}{e^2} c_1 = c_1 e^{-c_2 x^2} \rightarrow e^{-2} = e^{-c_2 x^2} \rightarrow 2 = c_2 x^2 \rightarrow c_2 = \frac{2}{x^2}$$

Where: x = radius of the laser beam [mm]

Therefore: $$c_2 = \frac{8}{(dia_{laser})^2}$$

The next constant to determine is c_1. To do this it must be realized that the surface shown in Figure 22 is the product of the z(x) and z(y), as shown in Equation 75.

(75) $$S = z(xy) = c_1^{\,2} e^{-c_2\left(x^2+y^2\right)}$$

The surface in Equation 75 is used to determine the power applied to each finite element in the wire. By performing a double integration on S in Equation 75, as shown in Equation 76, the volume under the surface, S, is calculated, and this represents the amount of energy in that fragment of the beam. Therefore, the limits of integration can be defined such that the power in a particular portion of the beam covering the wire is determined.

(76) $$P = \iint S dx dy \rightarrow P = \iint c_1^{\,2} e^{-c_2\left(x^2+y^2\right)} dx dy$$

The double integral in Equation 76 can be split into two, single integration as shown in Equation 77, below.

(77) $$P = c_1^{\,2} \left(\int e^{-c_2 x^2} dx \right) \left(\int e^{-c_2 y^2} dy \right)$$

But first, c_1 is determined by simply solving Equation 77 when the limits of integration are set to the beam radius. Since the limits of integration will account for the whole beam and the volume under the beam represents laser power, the whole beam should contain all of the laser power. The derivation of c_1 is shown below:

(78) $$P = {c_1}^2 \left(\int_{-r_{laser}}^{r_{laser}} e^{-c_2 x^2} dx \right) \left(\int_{-r_{laser}}^{r_{laser}} e^{-c_2 y^2} dy \right)$$

Note that in Equation 78 the integrals are exactly the same, including the limits of integration. The integrals in Equation 78 can be combined as shown in Equation 79.

(79) $$P = {c_1}^2 \left(\int_{-r_{laser}}^{r_{laser}} e^{-c_2 x^2} dx \right)^2$$

It can be realized that $\int_0^b \int e^{-ax^2} dx = \frac{1}{2}\sqrt{\frac{\pi}{a}} erf(b\sqrt{a})$ when a > 0. (Zwillinger ed., 2003)

Therefore, the integral in Equation 79 can be split into the sum of the two integrals as in Equation 80.

(80) $$P = {c_1}^2 \left(\int_{-r_{laser}}^{0} e^{-c_2 x^2} dx + \int_{0}^{r_{laser}} e^{-c_2 x^2} dx \right)^2$$

(81) $$P = {c_1}^2 \left(\frac{1}{2}\sqrt{\frac{\pi}{c_2}} erf(r_{laser}\sqrt{c_2}) + \frac{1}{2}\sqrt{\frac{\pi}{c_2}} erf(r_{laser}\sqrt{c_2}) \right)^2$$

(82) $$c_1 = \sqrt{\frac{P}{\left(\sqrt{\frac{\pi}{c_2}} erf(r_{laser}\sqrt{c_2}) \right)^2}}$$

11.7 Appendix: Derivation of Thermocouple Effects

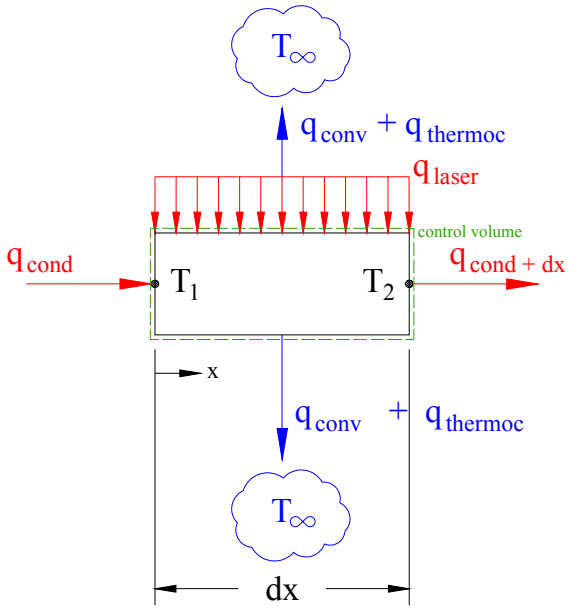

Figure 81. Single element used to calculate the heat distribution in the wire when a thermocouple is attached.

The following shows the same derivation that has been presented in Appendix 11.5, but now the heat transfer due to taking a thermocouple measurement has been added to the finite element, as seen in Figure 81. Note, parts of the derivation are abbreviated to reduce reputation, see Appendix 11.5 for the detailed derivation of these sections.

(83) $$E_{in} + E_g - E_{out} = E_{st}$$

Where: E_{in} = Energy into control volume [W]

E_g = Energy generated inside control volume [W]

E_{out} = Energy out of control volume [W]

E_{st} = Energy stored [W]

Substituting in for these values from Figure 81:

(84) $$\underbrace{q_{cond} + q_{laser}}_{E_{in}} \underbrace{- q_{cond+dx} - q_{conv} - q_{thermoc}}_{E_{out}} = E_{st}$$

Each of the components in Equation 84 can be expanded into:

(85) $$q_{cond} = -k\frac{\partial T}{\partial x}Adt$$

(86) $$q_{cond+dx} = q_{cond} + \frac{\partial q_{cond}}{\partial x}dx$$

(87) $$q_{laser} = Q_{laser}Adxdt$$

(88) $$q_{conv} = h(T(x,t) - T_{\infty})Pdxdt$$

(89) $$q_{thermoc} = k_t\frac{\partial T}{\partial r}Pdxdt$$

(90) $$E_{st} = c_p(\rho Adx)dT$$

Where: A = Cross-sectional area of the SMA wire [m^2]

c_p = Specific heat of wire [J/(kg*K)]

h = Convection coefficient [W/(m^2*K)]

k = Thermal conductivity of element [W/(m*K)]

k_t = Thermal conductivity of thermocouple cement [W/(m*K)]

Q_{laser} = Volumetric laser power [W/m^3]

T = Temperature of a particular point [K]

T_∞ = Ambient temperature [K]

r = thickness of thermocouple interface [m]

t = Time [s]

x = Position along wire [m]

ρ = Density of SMA wire [kg/m^3]

Combining Equations 84 through 90 the equation for heat transfer in the wire is realized in Equation 91.

(91)

$$E_{st} = -k\frac{\partial T}{\partial x}Adt + Q_{laser}Adxdt - \left(-k\frac{\partial T}{\partial x}Adt + \frac{\partial}{\partial x}\left(-k\frac{\partial T}{\partial x}Adt\right)dx\right) - \left(h\left(T(x,t)-T_{\infty}\right)Pdxdt\right) - \left(-k_t\frac{\partial T}{\partial r}Pdxdt\right)$$

Simplifying:

(92)

$$Q_{laser}Adxdt - \left(\frac{\partial}{\partial x}\left(-k\frac{\partial T}{\partial x}Adt\right)dx\right) - \left(h\left(T(x,t)-T_{\infty}\right)Pdxdt\right) + k_t\frac{\partial T}{\partial r}Pdxdt = c_p\rho AdxdT$$

Divide through by "Adxdt" to eliminate common terms

(93) $$Q_{laser} + \frac{\partial}{\partial x}\left(k\frac{\partial T}{\partial x}\right) - \frac{hP}{A}\left(T(x,t)-T_{\infty}\right) + \frac{k_tP}{A}\frac{\partial T}{\partial r} = c_p\rho\frac{dT}{dt}$$

The temperature distribution is assumed to be linear in the each finite element. When this approximate solution is substituted into the governing differential equation, Equation 93, an error will result. In order to try and drive this error to zero Galerkin's Method of Weighted Residuals (GMWR) is employed. Let the linear shape function be:

(94) $$N = \left[1 - \frac{\hat{x}}{L}, \frac{\hat{x}}{L}\right]$$

Where: $\hat{x}$ = Distance from left side of finite element [m]

L = Total length of finite element [m]

Rearranging Equation 93:

(95) $$Q_{laser} + \frac{\partial}{\partial x}\left(k\frac{\partial T}{\partial x}\right) - \frac{hP}{A}\left(T(x,t)-T_{\infty}\right) + \frac{k_tP}{A}\frac{\partial T}{\partial r} - c_p\rho\frac{dT}{dt} = 0$$

Let: $\Psi = T$, $c_1 = k$, $c_2 = -h*P/A$, $c_3 = h*P/A*T_\infty + Q_{laser}$, $c_4 = c_p\rho$, $c_5 = k_t*P/A$ so that the rest of the numerical analysis will be generalized and easier to conceptualize. Rewriting Equation 95 with substitutions:

$$c_1 \frac{\partial^2 \Psi}{\partial \hat{x}^2} + c_2 \Psi + c_3 + c_4 \frac{\partial \Psi}{\partial t} + c_5 \frac{\partial \Psi}{\partial r} = 0 \tag{96}$$

The general form used for GMWR is:

$$\iiint_V RN dV = 0 \tag{97}$$

Where: $R = c_1 \frac{\partial^2 \Psi}{\partial \hat{x}^2} + c_2 \Psi + c_3 + c_4 \frac{\partial \Psi}{\partial t} + c_5 \frac{\partial \Psi}{\partial r}$

$$N = \left[1 - \frac{\hat{x}}{L}, \frac{\hat{x}}{L}\right]$$

Substituting in for Equation 97:

$$\iiint_V N_i \left(c_1 \frac{\partial^2 \Psi}{\partial \hat{x}^2} + c_2 \Psi + c_3 + c_4 \frac{\partial \Psi}{\partial t} + c_5 \frac{\partial \Psi}{\partial r} \right) d\hat{x} d\hat{y} d\hat{z} = 0 \tag{98}$$

Since this is only a one-dimensional heat transfer problem in $d\hat{x}$, Equation 98 simplifies to:

$$\int_{\hat{x}} N_i \left(c_1 \frac{\partial^2 \Psi}{\partial \hat{x}^2} + c_2 \Psi + c_3 + c_4 \frac{\partial \Psi}{\partial t} + c_5 \frac{\partial \Psi}{\partial r} \right) d\hat{x} = 0 \tag{99}$$

Perform the integration of each term as that shown in Appendix 11.5. Below is the integration of the new sixth term, which incorporates the heat transfer due to the thermocouple. Evaluating the sixth integral:

(100) $$\int_{\hat{x}_i=0}^{\hat{x}_j=L} c_5 N_i \left(\frac{\partial \Psi}{\partial r}\right) d\hat{x} = R_{1,2}^5$$

Let the solution to Equation 100 be R_1^2 when N_1 is substituted in and let it be R_2^2 when N_2 is substituted.

(101) $$R_1^5 = c_5\left(\frac{\Psi_j - \Psi_i}{r}\right)\left(L - \frac{L}{2}\right) - c_5\left(\frac{\Psi_j - \Psi_i}{r}\right)(0) = c_5\left(\frac{\Psi_j - \Psi_i}{r}\right)\frac{L}{2}$$

(102) $$R_2^5 = c_5\left(\frac{\Psi_j - \Psi_i}{r}\right)\left(\frac{L}{2}\right) - c_5\left(\frac{\Psi_j - \Psi_i}{r}\right)(0) = c_5\left(\frac{\Psi_j - \Psi_i}{r}\right)\frac{L}{2}$$

Combine Equations 49, 50, 52, 53, 57, 58, 60, 61, 63, 64, 101, and 102 into matrix form:

(103)

$$\begin{Bmatrix} R_1 \\ R_2 \end{Bmatrix} = \begin{Bmatrix} -c_1 \left.\frac{\partial \Psi}{\partial \hat{x}}\right|_{\hat{x}=\hat{x}_i} \\ c_1 \left.\frac{\partial \Psi}{\partial \hat{x}}\right|_{\hat{x}=\hat{x}j} \end{Bmatrix} - \frac{c_1}{L}\begin{bmatrix} 1 & -1 \\ -1 & 1 \end{bmatrix}\begin{Bmatrix} \Psi_i \\ \Psi_j \end{Bmatrix} + \frac{c_2 L}{6}\begin{bmatrix} 2 & 1 \\ 1 & 2 \end{bmatrix}\begin{Bmatrix} \Psi_i \\ \Psi_j \end{Bmatrix} + \frac{c_3 L}{2}\begin{Bmatrix} 1 \\ 1 \end{Bmatrix} + \frac{c_4 L}{2}\frac{\partial \Psi}{\partial t}\begin{Bmatrix} 1 \\ 1 \end{Bmatrix} + \frac{c_5 L}{2r}\begin{bmatrix} -1 & 1 \\ -1 & 1 \end{bmatrix}\begin{Bmatrix} \Psi_i \\ \Psi_j \end{Bmatrix}$$

Rearranging Equation 103:

(104)

$$\begin{Bmatrix} c_1 \left.\frac{\partial \Psi}{\partial \hat{x}}\right|_{\hat{x}=\hat{x}_i} \\ -c_1 \left.\frac{\partial \Psi}{\partial \hat{x}}\right|_{\hat{x}=\hat{x}j} \end{Bmatrix} + \underbrace{\frac{c_1}{L}\begin{bmatrix} 1 & -1 \\ -1 & 1 \end{bmatrix}}_{[K]_{c_1}}\begin{Bmatrix} \Psi_i \\ \Psi_j \end{Bmatrix} - \underbrace{\frac{c_2 L}{6}\begin{bmatrix} 2 & 1 \\ 1 & 2 \end{bmatrix}}_{[K]_{c_2}}\begin{Bmatrix} \Psi_i \\ \Psi_j \end{Bmatrix} = \underbrace{\frac{c_3 L}{2}\begin{bmatrix} 1 \\ 1 \end{bmatrix}}_{[F]} + \underbrace{\frac{c_4 L}{2}\frac{\partial \Psi}{\partial t}\begin{bmatrix} 1 \\ 1 \end{bmatrix}}_{[C]} + \underbrace{\frac{c_5 L}{2r}\begin{bmatrix} -1 & 1 \\ -1 & 1 \end{bmatrix}\begin{Bmatrix} \Psi_i \\ \Psi_j \end{Bmatrix}}_{[K]_{c_5}}$$

Combining like terms in Equation 104 and plugging in for c_1, c_2, c_3, c_4, c_5 and Ψ:

(105)
$$\begin{Bmatrix} k\left.\frac{\partial T}{\partial x}\right|_{x=x_i} \\ -k\left.\frac{\partial T}{\partial x}\right|_{x=xj} \end{Bmatrix} + \left\{[K]_{c_1} + [K]_{c_2} + [K]_{c_5}\right\}\begin{Bmatrix} T_i \\ T_j \end{Bmatrix} = [F] + [C]\begin{Bmatrix} \frac{\partial T_i}{\partial t} \\ \frac{\partial T_j}{\partial t} \end{Bmatrix}$$

Where:
$$[K]_{c_1} = \frac{k}{L}\begin{bmatrix} 1 & -1 \\ -1 & 1 \end{bmatrix}$$

$$[K]_{c_2} = \frac{hPL}{6A}\begin{bmatrix} 2 & 1 \\ 1 & 2 \end{bmatrix}$$

$$[K]_{c_5} = \frac{k_t PL}{2rA}\begin{bmatrix} -1 & 1 \\ -1 & 1 \end{bmatrix}$$

$$[F] = \left(\frac{hPL}{2A}T_\infty + \frac{L}{2}Q_{laser}\right)\begin{bmatrix} 1 \\ 1 \end{bmatrix}$$

$$[C] = \left(\frac{c_p \rho L}{2}\right)\begin{bmatrix} 1 \\ 1 \end{bmatrix}$$

For the finite elements at the ends of the wire the end effects are ignored due the long length of the wire compared to the cross-sectional area, as well as a small cross-sectional area due to the small diameter of the thin wire. The rest of the derivation is carried out very similar to that shown in Appendix 11.5. The same global equation will result, but the variables in that global equation are defined by Equation 105.

11.8 Appendix: Matlab Code for Final Heat Transfer Model

```
%-------------------------------------------------------------------------%
% Finite Element Heat Transfer Model for Shape Memory Alloy Wire v.2.9.1  %
%                                                                         %
% Author: Ryan S. Dennis                                                  %
% Advisor: Dr. J. F. Tu                                                   %
% Created on: November 21, 2004; May 20, 2005                             %
% Last Modified: May 22, 2005 (16:17)                                     %
%-------------------------------------------------------------------------%

% Program: This program is designed to perform a finite element analysis of
% a SMA wire subject to a laser heat treatment to determine the temperature
% profile of that wire over time.

% Assumptions:
% 1) Heat transfer is 1-D along the length of the wire
% 2) Heat by laser beam is homogeneous through thickness of wire
% 3) Temperature distribution in each element is linear
% 4) Convection around the wire is only natural convection
% 5) Heat transfer tip effects are negligible

% Special features of this version:
% 1) Can plot the temperature distribution along the length of the wire in
%    time, and can be plotted in 2-D or 3-D.
% 2) Can plot the temperature change over time on single/multiple points
%    on the wire.
% 3) Plotting over distinct time intervals occurs in multiple colors.
% 4) The Convection coefficient is temperature dependent and is calculated
%    "on the fly."
% 5) A built in solver is now used to determine the temperature
%    distribution in the wire. Function files 'smafun_high_4' and
%    'smafun_low_4' was created.
% 6) Experimental temperature data is loaded from a text file, and the data
%    is plotted against the simulated temperature distribution. The format
%    of the file name is: 'Experiment 999.txt'
% 7) This model accounts for the Gaussian distribution of the laser beam
%    profile in applying the energy to each individual element. Function
%    file 'gaussbeam_2' was created.
% 8) Temperature bandwidth is used to control the laser switching,
%    corresponding timing vector and DMC vector generated. Function file
%    'threshold_2' was created.
% 9) A heating and cooling rate can be set for the treatment. Defined by
%    heat-up time, soak time, and cool-down time. Several varying cycles can
%    continuously exist in one heat treatment. Function file 'boundtemp_1'
%    was created.
% 11) This model incorporates the use of a pulsing laser beaming. Defined
%     by a pulse width and pulse period.
% 12) Can scan the laser beam repeatedly along some defined length of the
%     wire, with a fixed laser beam diameter.
% 13) Laser power and laser pulsing can be adjusted during middle of
%     treatment for each phase of the treatment. Also, no longer ON/OFF,
%     power is now switched between power levels, HIGH/LOW.
% 14) Helium is used as the ambient gas, and the convection coefficients
%     are changed accordingly.
% 15) Heat transfer due to thermocouples are now modeled at specificed
%     points on the wire.

% Functions list:
% boundtemp_1
% gaussbeam_2
% smafun_high_4
% smafun_low_4
% threshold_2
%-------------------------------------------------------------------------%

clear;
clc;
warning off MATLAB:divideByZero;
```

```
global abs a1 a2 b_dia disp_l disp_r dist_t dt k kt L L_e n P_element_h P_element_l pulse_p
pulse_w rt s scan_sp scan_st T_inf T_lower T_prev T_upper t_cyc w_dia w_rng
%-------------------------------------------------------------------------%

% Heat Treatment Constants
a1 = 0.340;                 % First Nusselt number constant [#]
a2 = 0.350;                 % Second Nusselt number constant [#]
s = 1;                      % Initialize laser to be ON at start of HT [bool]
T_inf = 300;                % Ambient temperature [K]
Tlim_l = 10;                % Lower limit for the temperature bandwidth [K]
Tlim_u = 10;                % Upper limit for the temperature bandwidth [K]
tog_c = 1;                  % Counts the toggles of the laser power [#]
tog_time = 0;               % Current time during numerical integration loop [s]
w_rng = 0.004;              % Length of wire to control temperature [m]

% Laser Beam Constants
abs_c = 1.83e5;             % Absorption constant as a f(w_dia)[%/m^2]
b_dia = 0.002;              % Diameter of laser beam at wire surface [m]

% Scanning Constants
disp_l = -0.000;            % Left-boundary of scanning, relative center (negative number)[m]
disp_r = 0.000;             % Right-boundary of scanning, relative center [m]
scan_sp = 0.000;            % Scanning speed of laser beam [m/s]
scan_st = 0.000;            % Start point of scanning, relative center (possible negative
number) [m]

% Simulation Constants
dt = 0.01;                  % Time step [s]
lag = 0.01;                 % Time lag for DDE solver [s]

% Thermocouple Constants
kt = 1.15376;               % Thermal conductivity of Omega CC High Temp. thermocouple cement
                              [W/m*K]
rt = 0.001;                 % Thickness of thermocouple interface [m]

% Wire Constants
k = 18;                     % Thermal conductivity [W/m*K]
L = 0.060;                  % Total length of wire [m]
w_dia = 0.00076;            % Diameter of SMA wire [m]

% Heat Treatment Vectors
ht_rate = [50];             % Heat-up rate vector for consecutive part of heat treatments
                              [K/s]
ht_time = [10];             % Time it will take to reach desired temperature with respective
                              heating rate [s]
sk_time = [10];             % Time to "soak" or hold the elements at a specific temperature
                              [s]
cl_rate = [0];              % Cool-down rate vector for consecutive part of heat treatments
                              (negative number) [K/s]
cl_time = [10];             % Time it will take to reach desired temperature with respective
                              cooling rate [s]

% Laser Power Vectors
P_laser_h = [40,40,0];      % HIGH Laser power cycle array ([ht,sk,cl,...] for each column in
                              HT vectors above) [W]
P_laser_l = [0,0,0];        % LOW Laser power cycle array ([ht,sk,cl,...] for each column in
                              HT vectors above) [W]

% Thermocouple Vectors
dist_t = [-0.000];          % Distance thermocouples are away from incident laser (neg.# =
                              left, pos.# = right) [m]

% Pulsing Vectors
pulse_p = [1.0,1.0,1.0];        % Pulse period of pulsing laser beam [s]
pulse_w = [1.0,1.0,1.0];        % Pulse width of pulsing laser beam [%]

% Dependent Variables
abs = abs_c*w_dia*b_dia;           % Percentage of laser beam absorbed [%]
L_e = b_dia/3;                     % Length of finite element [m]
n = round(L/L_e);                  % Number of finite elements [#]
sol = ones(n+1,1)*T_inf;           % Initialize DDE history, wire temp., to room temp. [K]
```

```
t_l = sum(ht_time+sk_time+cl_time); % Duration of heat treatment [s]
t = [0:dt:t_l];                     % Time vector for DDE evaluation [s]
%-------------------------------------------------------------------------%

% Global Time Cycle Vector
q = 1;                              % Initialize counter [#]
r = 1;                              % Initialize counter [#]
t_cyc_last = 0;                     % Initialize looping time holder [s]

% Creates a vector that refences the overall time value at which the heat
% treatment stages change
while q <= length(ht_rate)*3
    t_cyc(q) = ht_time(r) + t_cyc_last;     % Add in "rth" heating cycle time [s]
    t_cyc(q+1) = sk_time(r) + t_cyc(q);     % Add in "rth" soaking cycle time [s]
    t_cyc(q+2) = cl_time(r) + t_cyc(q+1);   % Add in "rth" cooling cycle time [s]
    t_cyc_last = t_cyc(q+2);                % Loop's time value holder [s]
    q = q + 3;                              % Increment counter [#]
    r = r + 1;                              % Increment counter [#]
end
%-------------------------------------------------------------------------%

% Boundary Temperature Profiles Function

% Ideal temperature vector for heat treatment [K]
[T_ideal] = boundtemp_1(cl_rate, cl_time, dt, ht_rate, ht_time, sk_time, T_inf);

T_lower = T_ideal - Tlim_l;      % Lower bound of threshold temperature [K]
T_upper = T_ideal + Tlim_u;      % Upper bound of threshold temperature [K]
%-------------------------------------------------------------------------%

% Gaussian Beam Profile Function

% Elemental laser power vectors for HIGH and LOW power [W]
[P_element_h] = gaussbeam_2(b_dia, L_e, n, P_laser_h, w_dia);
[P_element_l] = gaussbeam_2(b_dia, L_e, n, P_laser_l, w_dia);
%-------------------------------------------------------------------------%

% Numerical Integration and Evaluation
% The delay solver is used so that a previous temperature value is used to
% calculate the new h for each element in the wire.

% Set options for the DDE solver
opts = ddeset('MaxStep',0.05,'Events','threshold_2');

while tog_time(tog_c) < t_l
    if s==1
        % Creates a continuous solution on s_i to s_i+l with laser ON
        sol = dde23('smafun_high_4',lag,sol,[tog_time(tog_c), t_l],opts);
        s = 0;               % Toggle laser switch to off
    else
        % Creates a continuous solution on s_i to s_i+l with laser OFF
        sol = dde23('smafun_low_4',lag,sol,[tog_time(tog_c), t_l],opts);
        s = 1;               % Toggle laser switch to on
    end
    tog_c = tog_c+1;                        % Increment toggle counter
    tog_time(tog_c) = sol.x(length(sol.x));  % Captures the timestamp for each toggle of
                                               laser power
end

TempDist = deval(sol,t);             % Evaluate the temperature dist. on a set interval
tog_dmc = round(tog_time*1000);      % Converts tog_time vector from s to ms for DMC files

% Load Experimental Data
% TempData_1 = load('Experiment 999.txt');          % Must be in the current directory
%-------------------------------------------------------------------------%
```

11.9 Appendix: Simulink Model for D-Space

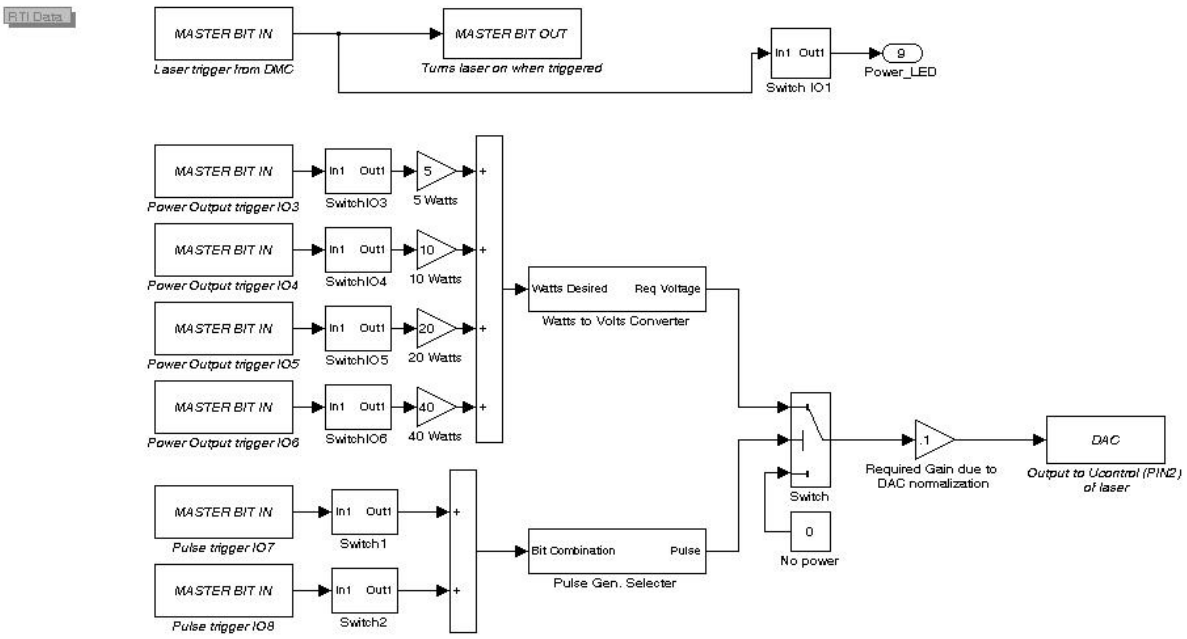

Figure 82. Top level of Simulink model used to control laser treatment program.

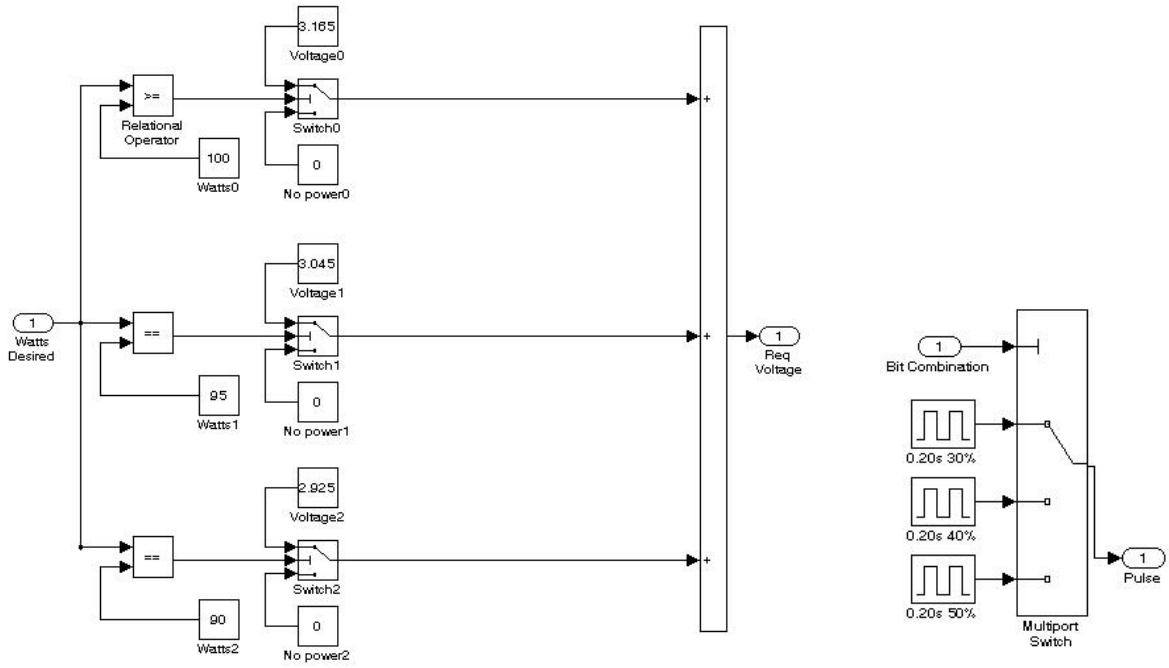

Figure 83. “Watts to Volts Converter” and “Pulse Gen. Selector” sub-block, respectively.